Summer 8-15-2013

Assessing Optic Neuritis in a Mouse Model of Multiple Sclerosis with Diffusion MR Imaging

Chia-Wen Chiang
Washington University in St. Louis

Recommended Citation

Chiang, Chia-Wen, "Assessing Optic Neuritis in a Mouse Model of Multiple Sclerosis with Diffusion MR Imaging" (2013). *Arts & Sciences Electronic Theses and Dissertations*. 1047.
https://openscholarship.wustl.edu/art_sci_etds/1047

WASHINGTON UNIVERSITY IN ST. LOUIS

Department of Chemistry

Dissertation Examination Committee:
Joseph J. H. Ackerman, Chair
Sheng-Kwei Song, Co-Chair
Anne H. Cross
Dewey Holten
Joshua Maurer
Liviu Mirica

Assessing Optic Neuritis in a Mouse Model of Multiple Sclerosis with Diffusion MR Imaging

by

Chia-Wen Chiang

A dissertation presented to the
Graduate School of Arts and Sciences
of Washington University in
partial fulfillment of the
requirements for the degree
of Doctor of Philosophy

August 2013

St. Louis, Missouri

Table of Contents

Chapter 1

Chapter 2

Chapter 3

Chapter 4

Chapter 5

Appendix

List of Figures

List of Tables

Acknowledgements

First, I would like to express my greatest gratitude to my advisor, Dr. Joseph J. H. Ackerman, and Dr. Sheng-Kwei Victor Song for their support, guidance, encouragement, and patience throughout my Ph.D. research. It is a great pleasure to learn and work with them. I sincerely appreciated all the help and experience they brought to me. I would also like to thank Dr. Joong Hee Kim for all his help, especially for his valuable discussion and comments, for sharing background knowledge, and for his input with immunohistochemistry quantification. I must also thank Dr. Yong Wang for his help and knowledge about the newly developed diffusion basis spectrum imaging (DBSI) approach and Monte-Carlo simulation, Dr. Peng Sun for his assistance with coding, Dr. Mingqiang Xie for guidance in immunohistochemistry staining, and Xiaojie Wang for sharing her knowledge and experience. I would like to specially thank Tsen-Hsuan Lin for all her help with experiments, support, and encouragement. This work could not have been completed without assistance of our collaborators: Dr. Anne H. Cross for all things, especially her clinical insight and valuable input for experiments, Bob Mikesell for help in numerous EAE immunizations, and Dr. Kim Trinkaus for her assistance with statistical analysis. I also wish to thank Dr. William M. Spees for guidance in presentation skills, languages and valuable input, Dr. Tsang-Wei Tu for his teaching and sharing of knowledge in experiments, Omar El-Ghazzawy for his guidance in languages, and John Engelbach for all the help he gave me during my projects.

I would to especially thank Dr. Dewey Holten, Dr. Liviu Mirica, and Dr. Joshua Maurer for serving on my dissertation committee, especially thanks to Dr. Holten and Dr. Mirica for valuable suggestions after every academic committee meeting.

I would also like to thank all the members in BMRL for all the help, discussion, encouragement and friendship.

In the end, I especially want to thank my lovely family for their patience, understanding, and encouragement. What I learned and experienced over these years were all appreciated. I dedicate this dissertation to them.

To my lovely family and friends

ABSTRACT OF THE DISSERTATION

Assessing Optic Neuritis in a Mouse Model of Multiple Sclerosis with Diffusion MR Imaging

by

Chia-Wen Chiang

Doctor of Philosophy in Chemistry

Washington University in St. Louis, 2013

Professor Joseph J. H. Ackerman, Chair

Professor Sheng-Kwei Song, Co-Chair

Optic neuritis (ON) is an early manifestation in patients of multiple sclerosis (MS), typically resulting in visual dysfunction. The inflammatory demyelination of the optic nerve in ON closely resembles pathologies of the rest of central nervous system (CNS) white matter in MS. Since accumulated axonal degeneration in MS was considered as the potential cause leading to permanent disability, correlating optic nerve pathology and visual function in ON could be a model system to investigate the relationship between functional outcome and neuropathology. It may also present a new way to reflect the disease progression in MS. Various MR techniques have been used to assess inflammation (inflammatory cell infiltration and vasogenic edema) of ON, but rarely demonstrated the ability to image cellularity changes non-invasively. Diffusion MRI measures the Brownian motion of water molecules in the microstructure of biological tissues. Diffusion tensor imaging (DTI) holds the promise to provide a specific biomarker of axonal injury and demyelination in CNS white matter by axial diffusivity (the diffusion parallel to white matter fibers) and radial diffusivity (the diffusion perpendicular to white matter fibers), respectively. However, DTI assumes a single diffusion tensor model and thus takes an average of varied diffusion components. In contrast, our recently developed diffusion basis spectrum imaging (DBSI) resolves the complex diffusion components and provides relatively accurate directional diffusivities and diffusion component fractions, relating to the detail and accurate pathological picture of the disease or injury. In the current work, in vivo 25-direction DBSI was applied to the optic nerve of mice with experimental autoimmune encephalomyelitis (EAE), an animal model of MS, with visual impairment at onset of ON. Our results demonstrate that inflammation correlated well with visual impairment in acute ON. DBSI successfully detected inflammatory cell infiltration and optic nerve white matter pathology in EAE that was consistent with histology, supporting the capability of DBSI to quantify increased cellularity, axonal injury and myelin damage in the optic nerve of EAE mice.

Chapter 1

Introduction

1.1 Multiple Sclerosis

Multiple Sclerosis [1] is an autoimmune disease of the central nervous system (CNS) primarily targeting myelinated axons of the CNS (Fig 1-1). This disorder is typically diagnosed in young adults and affects women more than men [2] . MS is named for the accumulation of scar tissue (sclerosis) around the multiple foci within the brain and spinal cord, inhibiting signals from CNS to the rest of the body which can cause MS patients to suffer a variety of neurological disorders in the clinic, involving motor and sensory disorder, disturbance of vision (e.g. blurred vision and blindness in one or both eyes), coordination, balance, and more [3, 4]. Although the etiology of MS is not known, the disease's neuropathology consists primarily of inflammatory demyelination at lesions in white matter CNS. The pathology is generally caused by invasion of inflammatory cells into the CNS and destruction of oligodendrocytes and patches of myelin sheaths and axons in variable degree [5-7] (Fig. 1-2).

Visual dysfunction is, frequently, the first clinical symptom in MS. Around 66% of patients with MS will have at least one episode of optic neuritis during the disease course (http://www.nationalmssociety.org/). There are two subtypes of optic neuritis associated with MS: retrobulbar neuritis (or inflammation of the optic nerve behind the eye) and papillitis (or inflammation of the optic disc) of which the former is the most commonly associated with MS [8].

Motor dysfunction also frequently develops during the MS disease time course. Based on disability, four clinically defined types of MS (Fig. 1-3) have been classified using standard neurological exams or extended disability status scoring [9]. Relapsing-remitting MS (RRMS), the most common type (~50% of the cases), is clinically characterized by recurrent attacks followed by either partial or total recovery from of neurological function, however these patients eventually develop a gradual neurological decline with repeated episodes of CNS inflammatory insult. Secondary progressive MS (SPMS) is the second most common type of MS (~30% of the cases) which may initially resemble RRMS before moving into a stage of progressive impairment. Primary progressive MS (PPMS) (~10% of the cases) begins as a gradual decline in function without remitting stages over the course of the disease. The fourth MS type, progressive relapsing MS (PRMS) (~5% of the cases) involves both progressive impairment and relapse from onset of the symptoms. The overall disease time course varies widely across these four classifications and even within each classification due to individual variability.

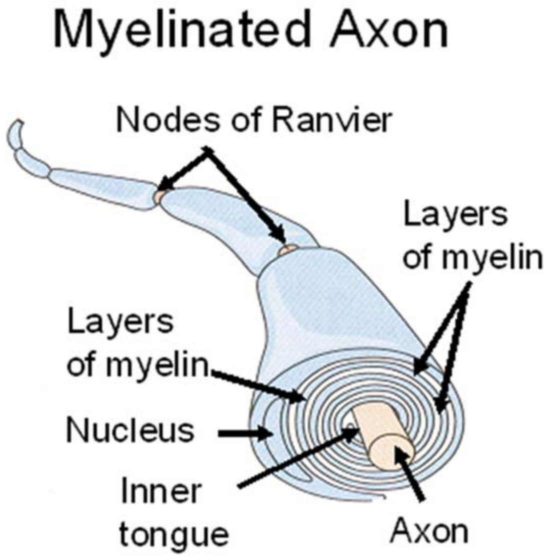

Kandel et. al, Principles of Neural Science 4th edition, Mc Graw Hill

Figure 1–1 The myelinated axon in white matter of central nerve system. The long cylindrical shape of axon is wrapped tightly by myelin sheath.

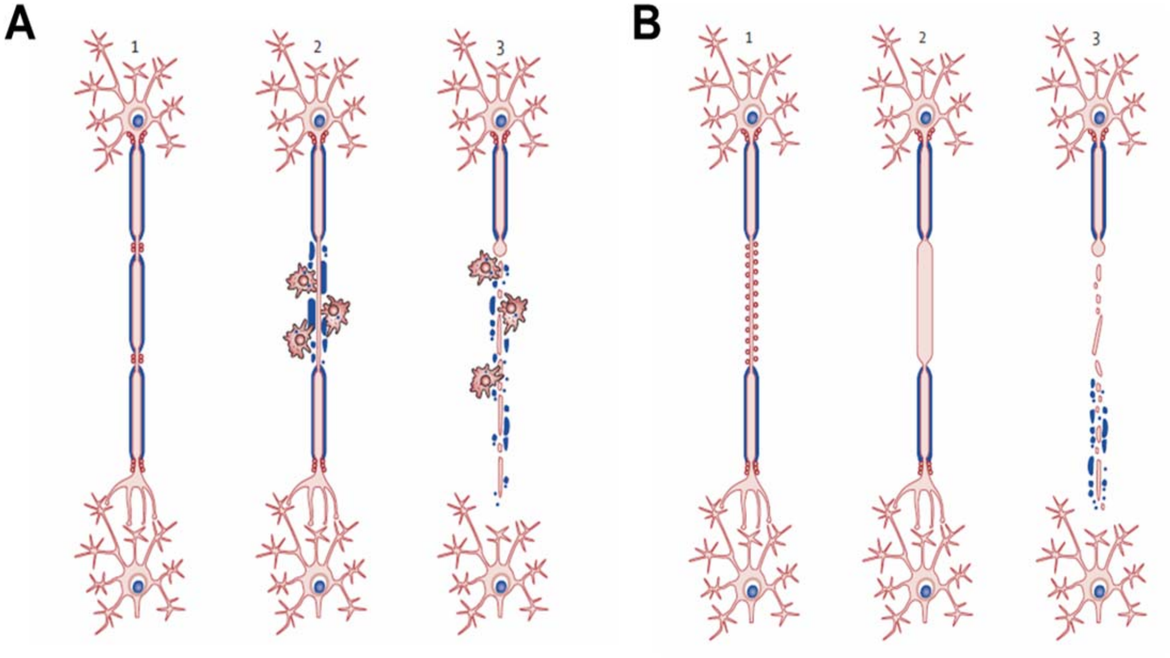

Trapp and Stys, Lancet Neurol 2009, 8(3): 280-91

Figure 1–2 (A) Summary diagram of axonal response during and after transection at acute stage, including (1) normal myelinated axons, (2) demyelination occurs due to immune-mediated process, and (3) the distal end of the transected axon rapidly degeneration. (B) degeneration of demyelinated axons process at chronic stage, including (1) most axons survive after demyelination and redistribute Na^+ channels, (2) chronically demyelinated axons exhibit slowly progressive swelling, (3) axons eventually degenerate.

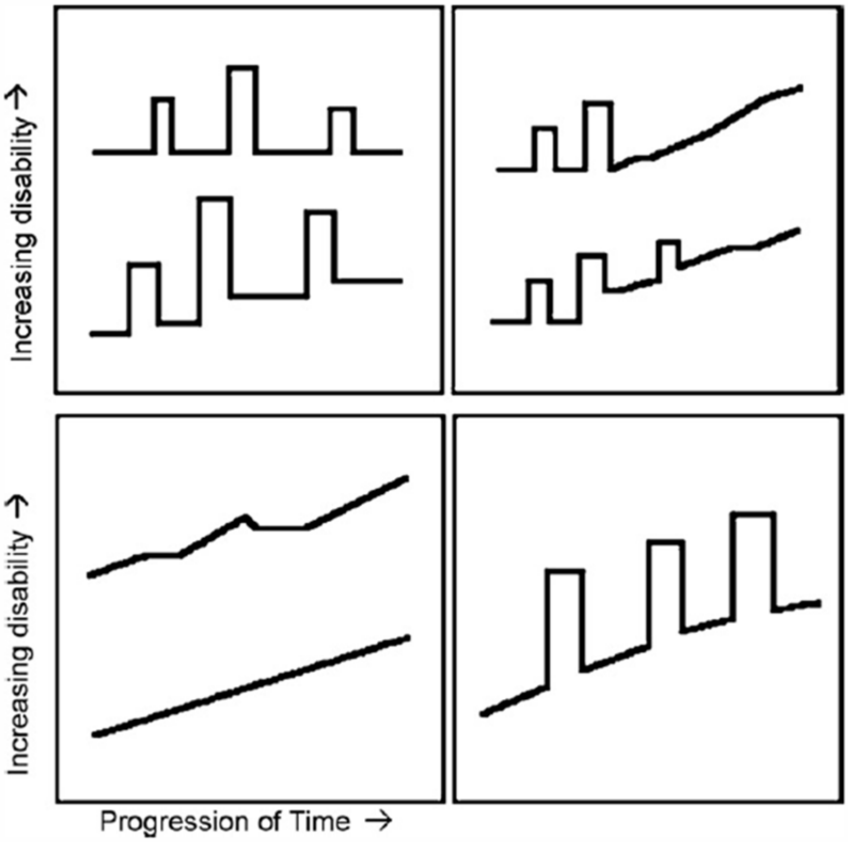

Zuvich et al. Semin Immunol 2009, 21(6): 328-333

Figure 1–3 Types of multiple sclerosis (left to right; top to bottom): relapsing-remitting, secondary progressive, primary progressive, and progressive relapsing.

1.2 Experimental Autoimmune Encephalomyelitis

Experimental Autoimmune Encephalomyelitis (EAE) is the most intensively used animal model system for studying MS pathologies [10]. EAE models mimic many of the clinical and neuropathological aspects of human MS, such as motor disability, visual dysfunction, as a result of CNS inflammatory demyelination. A major difference between MS and EAE is that the latter requires an external immunization step to develop. EAE is induced by injecting genetically susceptible animal strains with CNS myelin proteins such as myelin basic protein (MBP), myelin oligodendrocyte glycoprotein (MOG), and proteolipid protein (PLP). The innate immune system recognizes the introduced foreign matters as pathogens, and because native cells in the brain, spinal cord, and optic nerve express the same protein(s), the immune system attacks these proteins within the CNS. Thus, a MS-like disease can be induced in animals by stimulating innate T-cells to target myelin proteins. Similar to MS, EAE is also heterogeneous and influenced by the selected antigens, species and the genetic background.

Rodent EAE models can be induced on many different genetic strains with different myelin proteins such as PLP-EAE in SJL mice and MOG-EAE in C57BL/6 mice, and in rats. Each model may have different disease progression and proposed mechanism [11-15]. Among varied myelin proteins, MOG antigen tends to cause optic neuritis because of the high abundance of this protein inside the optic nerve [16]. The Inflammatory cell attack against the MOG autoantigen of the optic nerve is presumed to be the initiator in the sequence of events that ultimately lead to optic nerve damage. EAE models develop both encephalomyelitis and optic neuritis [16]. Furthermore, C57BL/6 mice immunized with MOG have been demonstrated to mimic many disease stages with pathological and clinical features of MS [12, 17]. MOG-induced EAE models are routinely used to study phenomena in the relapsing-remitting and chronic stages of the disease. Typically, mice in the acute stage (around 2 weeks post-immunization) exhibit an inflammatory response in optic nerve, spinal cord, and brain, which then leads to demyelination and axonal injury. EAE optic neuritis can produce a range of visual impairments, from mild to complete blindness in the affected animal [13]. Since disease events and relationships with functional outcomes have been extensively characterized in EAE, it is a good model for studying pathophysiology of MS and associated optic neuritis. Animal model have been very useful in developing and validating *in vivo* MRI techniques with histological assessment, which is not possible in human studies. In this study, MOG-EAE in C57BL/6 mice was used as an inflammatory demyelinating model of MS.

1.3 Optic nerve morphology and visual function

Optic nerve pathology may develop after just a single attack of optic neuritis [18]. Persistent or permanent vision loss has been shown to result from accumulated damage to the optic nerve and retina. Pathological consequences at the retina can include retinal nerve fiber layer (RNFL) thinning, retinal ganglion cell (RGC) loss, and decreased macular volume [19, 20]. In general, post-mortem histological examination of optic nerve and retina is used to determine the degree of injury and the pathological mechanism at different disease stages.

As noted in Section 1.2, the mechanism of neurodegeneration in EAE ON differs depending on the particular EAE model with inter-animal variability within each model. For example, MOG-induced EAE models described in the literature in C56BL/6 mice are reported to develop optic nerve inflammation prior to RGC loss [12, 13]. However, axonal irregularity or degeneration may also coincide with cell infiltration prior to demyelination [13]. In contrast, inflammatory-cell-infiltration-induced demyelination secondary to direct RGC loss has been revealed in a rat model of MOG-EAE [14]. Since histology studies of tissue morphology are accepted as a gold standard for validation, it is essential to develop a systematic and objective approach to accurately quantify histopathology in disease or injury. Our newly-developed, non-invasive MRI approach to studying optic nerve pathology is detailed and examined in Chapter 2.

Several techniques are used to examine changes in function of optic nerve or retina in mice with optic neuritis. Visual evoked potential (VEP) measures the gross electrical potential at the level of the visual cortex in response to visual stimulus, reflecting optic pathway conductivity [13, 21]. A delayed VEP latency is presumed to represent demyelination of axons in the optic nerve. Optokinetic tracking response (ORK) is an objective assessment of visual acuity (VA) based on evaluation of mouse head tracking movement similar to optikinetic nystagmus in humans, reflecting the function of visual pathway [22, 23] (Fig. 1-4). Electroretinography [24] recording reflects the activity of neuronal cells within the retina resulting from visual stimulation [25, 26]. In the present study, mouse visual function was evaluated in acute EAE optic neuritis using OKR as detailed in chapter 4.

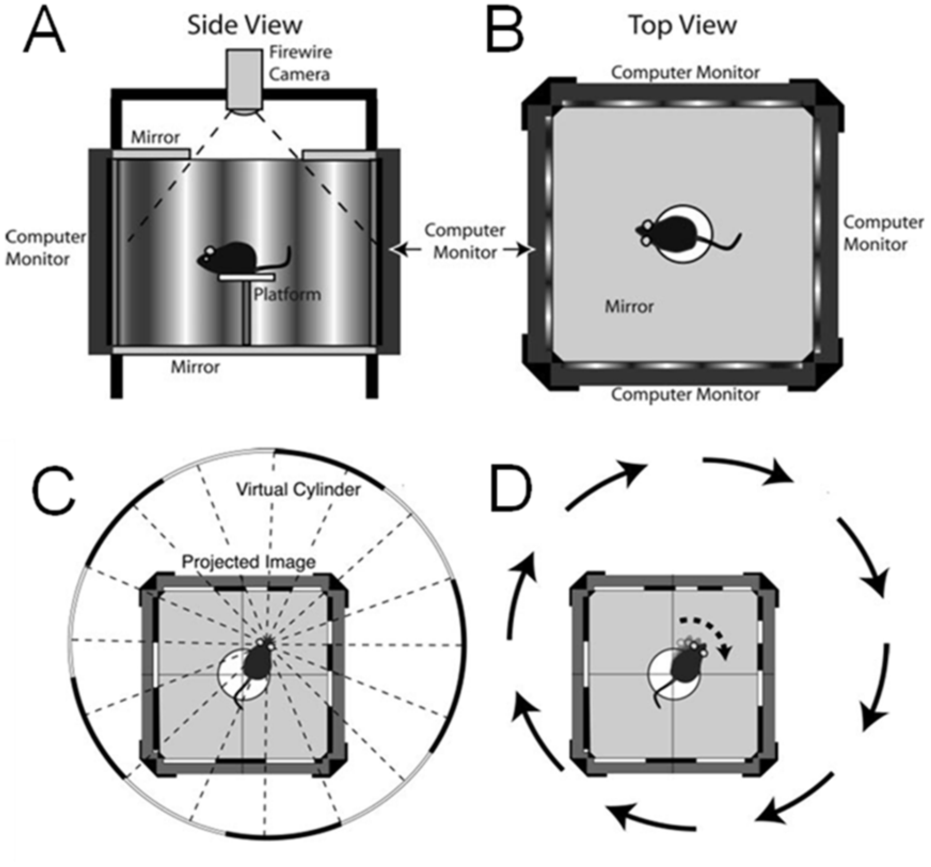

Prusky et al., IOVS 2004, 45(12): 4611-4616

Figure 1–4 Visual function was assessed by visual acuity (VA) using a Virtual Optometry System (OptoMotry, CerebralMechanics, Inc., Canada). OptoMotry apparatus in side view (A) and top view (B). In brief, a mouse was placed on the platform in a closed chamber with four computer monitors arranged in a square. Waiting until mouse stopped moving, a virtual cylinder of a grating with an adjustable spatial frequency (at 100% contrast, 12 degree/sec) was projected, centering in mouse head and moving in either clockwise or counter-clockwise direction (C). Mouse was observed through a camera and mouse visual threshold was determined by increasing the spatial frequency until mouse head cannot track the cylinder rotation, judging that mouse cannot see the grating. In addition, mouse head tracks the virtual rotation if seeing the grating (D). Visual function was reflected by VA, the highest spatial frequency mouse can see, in a unit of cycle/degree (c/d). Mice track in one direction with each eye, thus individual mouse eye vision could be assessed by applying specific rotating direction.

1.4 Imaging optic neuritis

Optical coherence tomography (OCT), a relatively new technique, based on patterns of infra-red light reflected from the back of the eye, detects structural changes in RNFL (reflecting optic nerve fiber), thickness of other retinal layers and macular volume, which serve as an imaging outcome [27, 28]. However, OCT is limited in its applicability for direct studies of optic nerve. Magnetic resonance imaging (MRI) techniques allow direct imaging of the optic nerve and have shown great potential to estimate the underlying pathology in optic neuritis. For example, increased gadolinium-contrast enhanced MRI determination of optic nerve volume in EAE reflects breakdown of blood nerve barrier, suggesting optic nerve inflammation [29, 30]. Cell infiltration, another aspect of inflammation, in MS has been shown to occur early by ultra-small particles of iron oxide (USPIO) enhanced MRI [31]. Optic nerve swelling (or increased optic nerve mean area) was detected in acute optic neuritis by short tau inversion recovery MR imaging, suggesting optic nerve inflammation [32]. Furthermore, diffusion tensor imaging (DTI) analysis has demonstrated that decreased axial diffusivity and increased radial diffusivity correlate well with axonal injury and demyelination of the optic nerve in chronic EAE, providing quantitatively non-invasive biomarkers of white matter injuries in CNS [15].

The assumption of Gaussian diffusion, inherent in the DTI model, limits its ability to provide an accurate and detailed picture of disease pathology in acute EAE optic neuritis. For instance, inflammation coincident with other pathological changes is responsible for a clear non-Gaussian diffusion component. Our recently-developed diffusion basis spectrum imaging (DBSI) enables us to resolve the contribution of this non-Gaussian signal component [33]. A detailed comparison of diffusion MRI using both DTI and DBSI model analyses are presented later in this study (see Chapter 3 and 4).

1.5 Diffusion MRI

In the following sections, the principles of diffusion MRI (dMRI) are discussed. dMRI relies on random diffusional motion of water molecule to reflect tissue contrast and is highly associated with anatomical microstructure. At the end of this section, several current working models are also introduced.

1.5.1 Diffusion in spin echo NMR and MRI

In ^{1}H MRI, we are usually concerned with the behavior of water protons. Protons placed in an applied homogeneous magnetic field, B_0, will precess about the direction of the applied field, at the Larmor frequency, according to equation [1-1] (Fig. 1-5 A). In tissue, the total vector sum of proton dipoles can be represented as a single vector, the so-called magnetization, that precesses about the direction of B_0 [34] (Fig. 1-5 B).

$$\omega = \gamma B_0 \qquad [1-1]$$

Diffusional motion in an inhomogeneous magnetic field induces phase incoherence in the macroscopic magnetization causing signal attenuation. The effect of diffusion on the MR signal was first addressed in 1950 by Hahn [35]. Carr and Purcell quantitatively analyzed the diffusion-induced spin-echo-signal attenuation in the presence of a constant gradient, which produces a linear spatial variation in Larmor frequency [36]. The resulting spin-echo amplitude is described by:

$$\mathrm{S(nTE)} = \exp\left[-\frac{\mathrm{D}\gamma^2\mathrm{G}_0^2\mathrm{TE}^3}{12\mathrm{n}^2}\right] \qquad [1-2]$$

where TE is echo time, D is diffusion coefficient, γ is gyromagnetic ratio, G_0 is steady gradient, and n is number of the echo in a multiple-spin-echo experiment.

However, the diffusion measurement using constant gradients is not optimal for MRI studies. The constant gradient would affect the slice-selection profile significantly and also would affect MR signal readout, causing significant reduction of signal-to-noise ratio. In 1965, Stejeskal and Tanner introduced MR diffusion measurements using a pair of pulsed-field diffusion-sensitizing gradients [37]. The spin echo sequence with a diffusion sensitizing gradient pair is shown in Fig. 1-6. Stejskal and Tanner initiated their work from the Bloch equations with a diffusion term, as initially proposed by Torrey [38].

In the presence of magnetic field, the macroscopic magnetization experiencing both T_1 and T_2 relaxation is quantitatively described using empirical vector equation introduced by Bloch [39, 40]:

$$\frac{d\overrightarrow{M}(\vec{r},t)}{dt} = \gamma\overrightarrow{M}(\vec{r},t) \times \overrightarrow{B}(\vec{r},t) - \left(\frac{M_x\vec{x} + M_y\vec{y}}{T_2}\right) + \left(\frac{\overrightarrow{M_0} - M_z\vec{z}}{T_1}\right) \qquad [1-3]$$

In this equation, γ is the gyromagnetic ratio, $\overrightarrow{M}(\vec{r},t) = (M_x\vec{x} + M_y\vec{y} + M_z\vec{z})$ is the net magnetization, $\overrightarrow{B}(\vec{r},t)$ is the externally-applied magnetic field (which may vary as a function of time and/or position), $\overrightarrow{M_0}$ is the equilibrium state magnetization, T_1 is spin-lattice relaxation time, and T_2 is spin-spin relaxation time. The differential equation [1-3] is further generalized by including Torrey's self-diffusion term [38], with the result:

$$\frac{d\overrightarrow{M}(\vec{r},t)}{dt} = \gamma\overrightarrow{M} \times \overrightarrow{B}(\vec{r},t) - \left(\frac{M_x\vec{x} + M_y\vec{y}}{T_2}\right) + \left(\frac{\overrightarrow{M_0} - M_z\vec{z}}{T_1}\right) + \vec{\nabla} \cdot \left(D\vec{\nabla}\overrightarrow{M}\right) \qquad [1-4]$$

Here D is diffusion coefficient. Torrey showed that if diffusion is isotropic, the equation [1-4] can be rewritten in an alternate, slightly simplified form as:

$$\frac{d\overrightarrow{M}(\vec{r},t)}{dt} = \gamma\overrightarrow{M} \times \overrightarrow{B} - \left(\frac{M_x\vec{x} + M_y\vec{y}}{T_2}\right) + \left(\frac{\overrightarrow{M_0} - M_z\vec{z}}{T_1}\right) + \left(D\nabla^2\overrightarrow{M}\right) \qquad [1-5]$$

Stejeskal and Tanner started their derivation from this assumption of isotropic diffusion. First Stejeskal and Tanner considered complex transverse magnetization as

$$m = M_x + iM_y \qquad [1-6]$$

then, the non-diffusion related term was eliminated by introducing equation [1-7]

$$m = \Psi \exp[-i\omega_0 t - t/T_2], \qquad [1-7]$$

yielding equation [1-8]

$$\frac{d\Psi}{dt} = -i\gamma\left(\vec{r}\cdot\vec{G}\right)\Psi + (D\nabla^2\Psi) \qquad [1-8]$$

In equation [1-8], $\vec{G}$ is the applied magnetic field gradient Stejskal and Tanner assumed that the values of Ψ immediately after 90° RF pulse is constant, which is S in equation [1-9] and there is no additional phase accumulation during application of the 180° RF pulse. Then in the absence of diffusion, the equation [1-8] can be rewritten.

$$\Psi = S\exp\left[-i\gamma\vec{r}\cdot(\vec{F} - 2H\,(t-\tau)\vec{f}\right] \qquad [1-9]$$

In equation [1-9], H is the Heaviside step function, τ is half-echo time in the spin-echo sequence (Fig. 1-6), and $\vec{F}$ and $\vec{f}$ are given as follows:

$$\vec{F} = \int_0^t \vec{G}(t')dt' \text{ and } \vec{f} = \vec{F}(\tau) \qquad [1-10]$$

To solve the equation [1-8] in the presence of diffusion Stejeskal and Tanner assumed that the solution to be the form of equation [1-9] and the S is to be function of time, S(t). Then S(t) at the echo time in spin-echo pulsed field gradient pair is expressed as equation [1-11]

$$\ln\left[\frac{S(TE)}{S(0)}\right] = -D\gamma^2\{\int_0^{TE}\vec{F}^2dt - 4\vec{f}^2\cdot\int_{\frac{TE}{2}}^{TE}\vec{F}\,dt + 4\vec{f}^2(TE)\} \qquad [1-11]$$

In spin-echo diffusion experiments, the extent of the sequence-specific signal- attenuation is described by its b value (in ms/μm^2). Using this compact notation, equation [1-11] is rewritten as

$$\ln\left[\frac{S(b)}{S(0)}\right] = -bD. \qquad [1-12]$$

It is readily seen that the b-value depends on the pulsed-field-gradient amplitude, duration, and the time between the two pulsed-field gradients. For a pair of square gradient lobes of the same amplitude, G (e.g., Fig. 1-6) the b value is given by

$$b = \gamma^2 G^2 \delta^2 \left(\Delta - \frac{\delta}{3}\right) \qquad [1-13]$$

Equations [1-12] and [1-13] are the key results of the famous work of Stejskal and Tanner [37]. These equations hold for conditions of non-bounded isotropic diffusion.

As shown in equation [1-10] and [1-11], the b-value is directly related to the amount of phase of the ensemble of magnetization, which is mostly integral part of equation [1-11]. This means that the applied diffusion sensitizing gradient shape affects consequent b-value. If the diffusion sensitizing gradient pair does not consist of square pulses, the b-value needs to be modified. For example, in the case of half-sine-shaped diffusion gradients (Fig. 1-7), the b value is given by

$$b = \frac{4}{\pi^2} \gamma^2 G^2 \delta^2 (\Delta - \frac{\delta}{4}) \qquad [1-14]$$

and for a trapezoidal-shaped gradient pair, the b value is given by

$$b = \gamma^2 G^2 [\delta^2 \left(\Delta - \frac{\delta}{3}\right) + \frac{\varepsilon^3}{30} - \frac{\delta \varepsilon^2}{6}] \qquad [1-15]$$

where ε is the ramp time [41]. Note that equation [1 – 15] becomes equation [1 – 13] if ε is negligible.

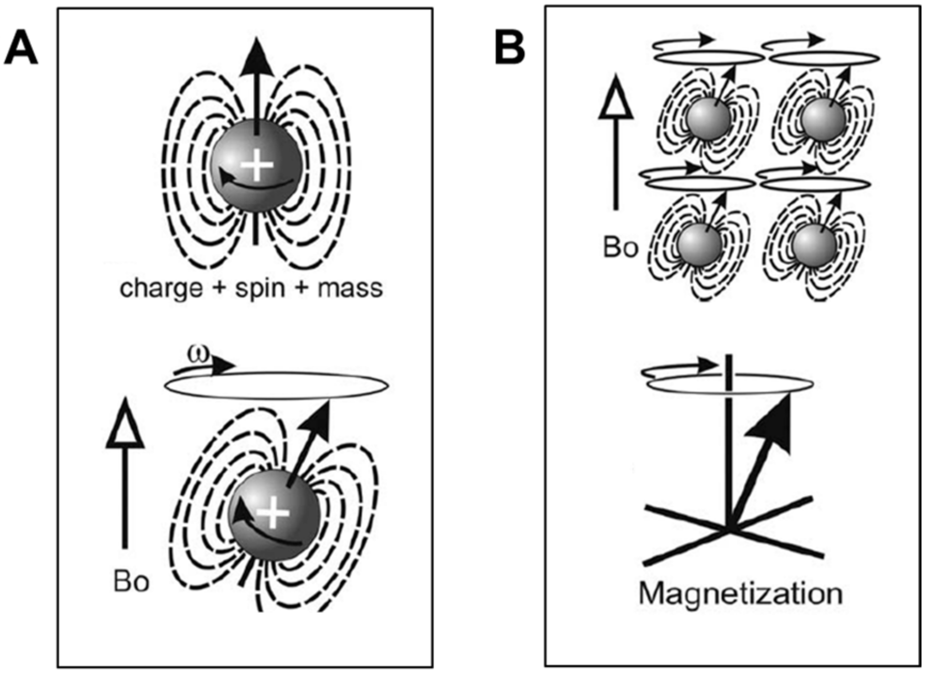

Plewes and Kucharczyk, JMRI 2012, 35: 1038-1054

Figure 1–5 Each water proton is considered as a spinning sphere with charge and mass and precesses about the direction of applied magnetic field B_0 (A). In tissue, tons of protons precess could represent as a single vector, so-called magnetization (B)

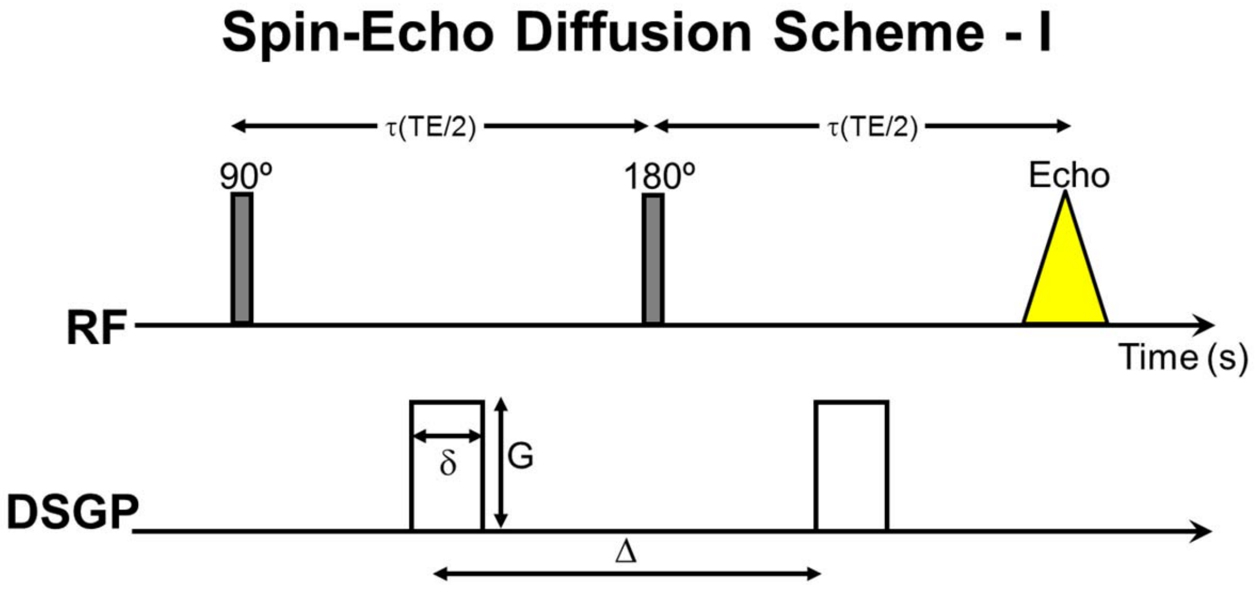

Figure 1–6 The Stejskal-Tanner Pulsed-Gradient Spin-Echo sequence with square-wave diffusion-sensitizing gradients. G - gradient strength, δ - duration of diffusion sensitizing gradient, Δ- time interval between diffusion-sensitizing gradient pulses, RF – radio frequency to excite nuclear spin, and DSGP – diffusion sensitizing gradient pair

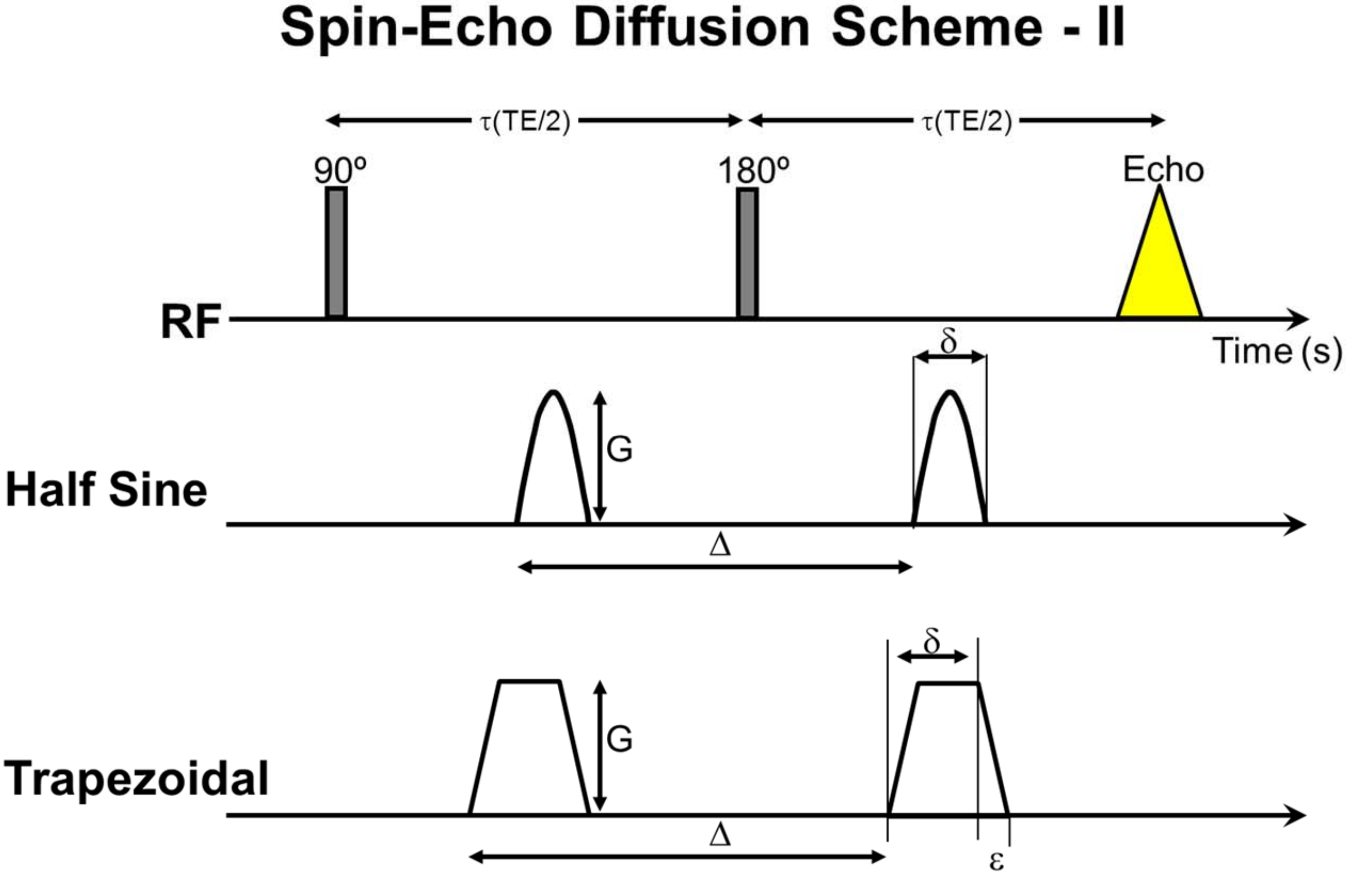

Figure 1–7 The Spin-Echo sequence with non-constant gradient amplitude. G -gradient strength, δ -duration of diffusion sensitizing gradient, Δ- time interval between diffusion sensitizing gradient pair, ε-ramp time

1.5.2 Apparent diffusion coefficient and anisotropy

Isotropic diffusion, exhibited in pure liquid, is sufficient to describe transport properties resulting from random thermally-induced collisions of molecules. However, Tanner found that isotropic self-diffusion could not fully describe particle motion in in more complex heterogeneous media like living tissue [42, 43]. Tanner introduced the concept of the apparent diffusion coefficient to explain the observed diffusivity in complex media. The apparent diffusion coefficient (ADC) is the diffusivity which would be calculated based upon the assumption of an isotropic Gaussian distribution of molecular displacements. Yet it didn't take long time to have reports on non-isotropic diffusion observation in biological tissue. The most distinct diffusion phenomenon in biological tissue compared to pure liquid is anisotropy. Cleveland et al, observed anisotropic diffusion in biological tissue in diffusion NMR [44]. Using Stejeskal and Tanner's diffusion measurement methodology, diffusion weighted imaging (DWI) studies reported that the observed ADC was affected by the orientation of the tissue with respect to the diffusion sensitizing gradients and is now well-appreciated [45, 46].

To evaluate the anisotropy of living tissue using diffusion magnetic resonance imaging, Basser, Le Bihan, and Mattiello introduced the tensor matrix idea into Stejeskal and Tanner's diffusion equation, resulting in a tensor $\widetilde{\mathrm{D}}$ instead of scalar D. The DTI analysis requires acquisition of a series of DWIs [41, 47, 48]. In diffusion tensor treatment, the diffusion equation [1-12] is now expressed as follows:

$$\frac{\mathrm{S(b)}}{\mathrm{S(0)}} = \exp\left(-\sum_{\mathrm{i=1}}^{\mathrm{n}}\sum_{\mathrm{j=1}}^{\mathrm{m}} \mathrm{b_{ij}}\,\mathrm{D_{ij}}\right) \qquad [1-16]$$

where in $\mathrm{b_{ij}}$ is i-j$^{\mathrm{th}}$ component in the b matrix and $\mathrm{D_{ij}}$ is i-j$^{\mathrm{th}}$ component of the apparent diffusion tensor. The diffusion tensor analysis produces additional parameters which are used to describe diffusion properties. From the diffusion-tensor matrix the eigenvalues (λ_1, λ_2, λ_3) and eigenvector (ε_1, ε_2, ε_3) can be calculated (Fig. 1-8). λ_1 and ε_1 represent the principal eigenvalue and eigenvector, respectively. The size of diffusion ellipsoid size is estimated by Trace of $\widetilde{\mathrm{D}}$.

$$\mathrm{Tr(D)} = \lambda_1 + \lambda_2 + \lambda_3 = 3 < D > \qquad [1-17]$$

The magnitude of deviation of diffusion from being purely isotropic is estimated by variance of the eigenvalues.

$$\mathrm{Var\ (D)} = \frac{(\lambda_1 - < D >)^2 + (\lambda_2 - < D >)^2 + (\lambda_3 - < D >)^2}{3} \qquad [1-18]$$

The anisotropy of the diffusion ellipsoid is quantified in terms of fractional anisotropy (FA) or relative anisotropy (RA) - quantities which are known to be rotationally invariant [49].

$$\mathrm{FA} = \frac{3}{\sqrt{2}} \frac{\left(\sqrt{\mathrm{Var(D)}}\right)}{\sqrt{\lambda_1^2 + \lambda_2^2 + \lambda_3^2}} \qquad [1-19]$$

$$\mathrm{RA} = \frac{\left(\sqrt{\mathrm{Var(D)}}\right)}{< D >} \qquad [1-20]$$

The anisotropy indices have been used to reflect microstructure of white matter [50, 51]. In addition, the principal eigenvalue (λ_1 or $\lambda_{\parallel}$, axial diffusivity) and the mean of the other two eigenvlaues ($(\lambda_2 + \lambda_3)/2$ or $\lambda_{\perp}$, radial diffusivity) have been used to detect abnormal white matter in various studies [51].

The application of diffusion tensor imaging has been extended to DTI fiber tractography. The basic idea of DTI tractography is provided by Basser [41], which is that the eigenvector-related principal eigenvalue is parallel to the major fiber direction in an image voxel. With certain thresholds on anisotropy and angle between two adjacent principal eigenvectors, DTI tractography has been used to provide reasonably accurate maps of the major white matter tracts [52-54]. The use of DTI has been mainly focusing on CNS.

Due to the complex structure of CNS tissue, the diffusion-sensitizing gradient directions and magnitude, or so called diffusion scheme requires optimization. Sampling diffusion properties with a scheme employing a large set of spatially-distributed diffusion encodings would provide for the most precise mapping of diffusion indices in CNS. However, the implementation of overly elaborate diffusion schemes is limited by practical limits of the required data acquisition time. In previous work, Derek Jones has extensively studied the optimized diffusion scheme [51]. In the current work we focus primarily on comparison of two diffusion schemes for ex vivo studies (99 and 25 directions) and implement the 25-direction scheme for *in vivo* studies (See chapter 3).

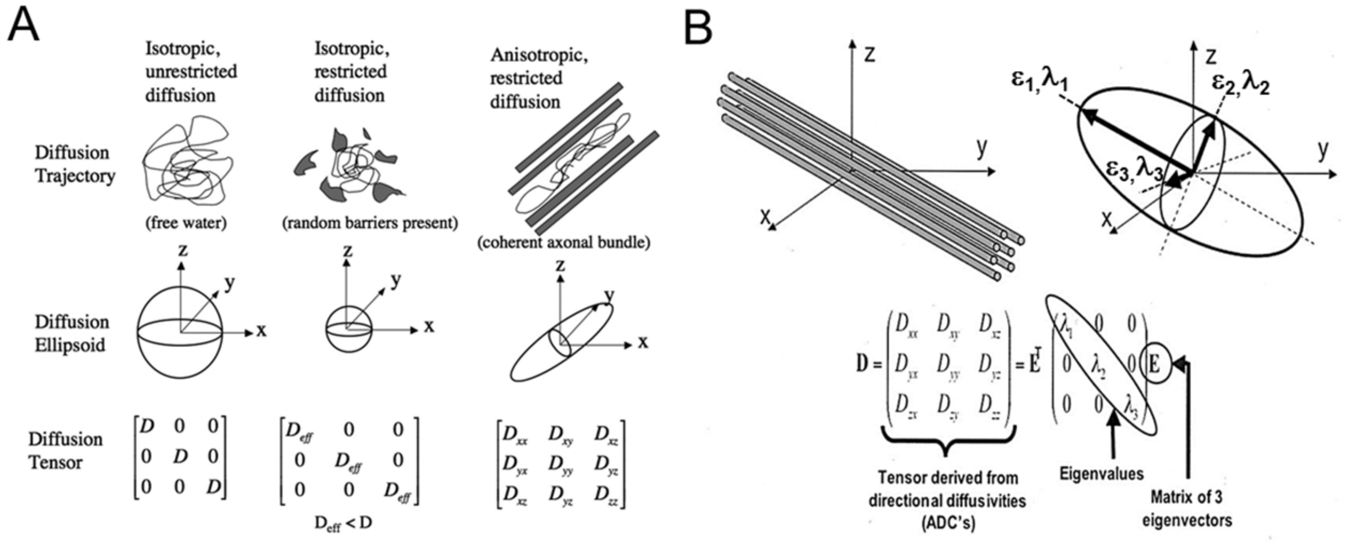

Mukherjee et al., AJNR 2008, 29: 632-641

Jellison et al., AJNR 2004, 25: 356-369

Figure 1–8 The diffusion ellipsoids and tensors for isotropic unrestricted diffusion, isotropic restricted diffusion and anisotropic diffusion are shown (A). Fiber tracts have an arbitrary orientation with respect to scanner geometry (x, y, z axes) and impose directional dependence (anisotropy) on diffusion measurements (B, top left). Anisotropic diffusion ellipsoid with orientation characterized by three eigenvectors (ε_1, ε_2, ε_3) and shape characterized by three eigenvalues (λ_1, λ_2, λ_3) (B, top right) which can be calculated by diagonalizing the diffusion tensor ($\vec{D}$) (B, bottom).

1.5.3 Effect of imaging gradients on b-value

It is inevitable that magnetic field gradients other than those required for diffusion-weighting, must be employed for MR imaging. The requisite imaging gradients encode for position in the three cardinal imaging directions: slice selection, phase encoding, and readout. The imaging gradients produce additional diffusion-weighting. Fig. 1-9 shows spin-echo diffusion experiment scheme with an additional gradient for spatial information, which is frequency-encoding for one-dimensional profile image. In Fig. 1-9 A, one sees readily that there are two different diffusion sensitizing gradient pairs, δ_d and δ_f. Thus, the additional imaging gradient imparts its own contribution to the total b value of the measurement:

$$b_f = \gamma^2 G_f^2 \delta_f^2 \left(\Delta_f - \frac{\delta_f}{3}\right) \qquad [1-21]$$

For a complete description of the diffusion-sensitization produced by the imaging sequence and most accurate diffusivity estimates, one needs to explicitly account for the contributions made by these imaging gradients. There are strategies that can be employed to minimize the contribution of phase-encoding gradients (e.g., Fig. 1 – 9 B, wherein the prephasing frequency encoding gradient is moved to right next to main frequency encoding gradient). In this case, the Δ_f is equal to δ_f and the effect of b_f on the diffusion calculation is minimized. Unfortunately, redesigning of diffusion sequence doesn't provide absolute solution for accurate diffusion measurement in the presence of imaging gradients. Thus one needs to consider interactions between all gradients [47]. In addition to imaging gradient for spatial encoding, MR diffusion imaging often requires large crusher gradients to minimize stimulated echoes caused by imperfect 180° RF pulses. Fig. 1-10 shows 2 dimensional spin-echo diffusion sequences with crusher gradient. As shown, there are three major interactions between gradients, which are 1) between diffusion sensitizing gradients, 2) between imaging gradients, and 3) between imaging and diffusion sensitizing gradient. Surely, the main diffusion sensitivity b-value is produced by the diffusion-sensitizing gradients pair. In general, the crusher gradient pair produces 2nd major b-value, about 0.1 ms/μm^2. In the work presented in this study, all three interactions between gradients were taken into account to calculate b-value.

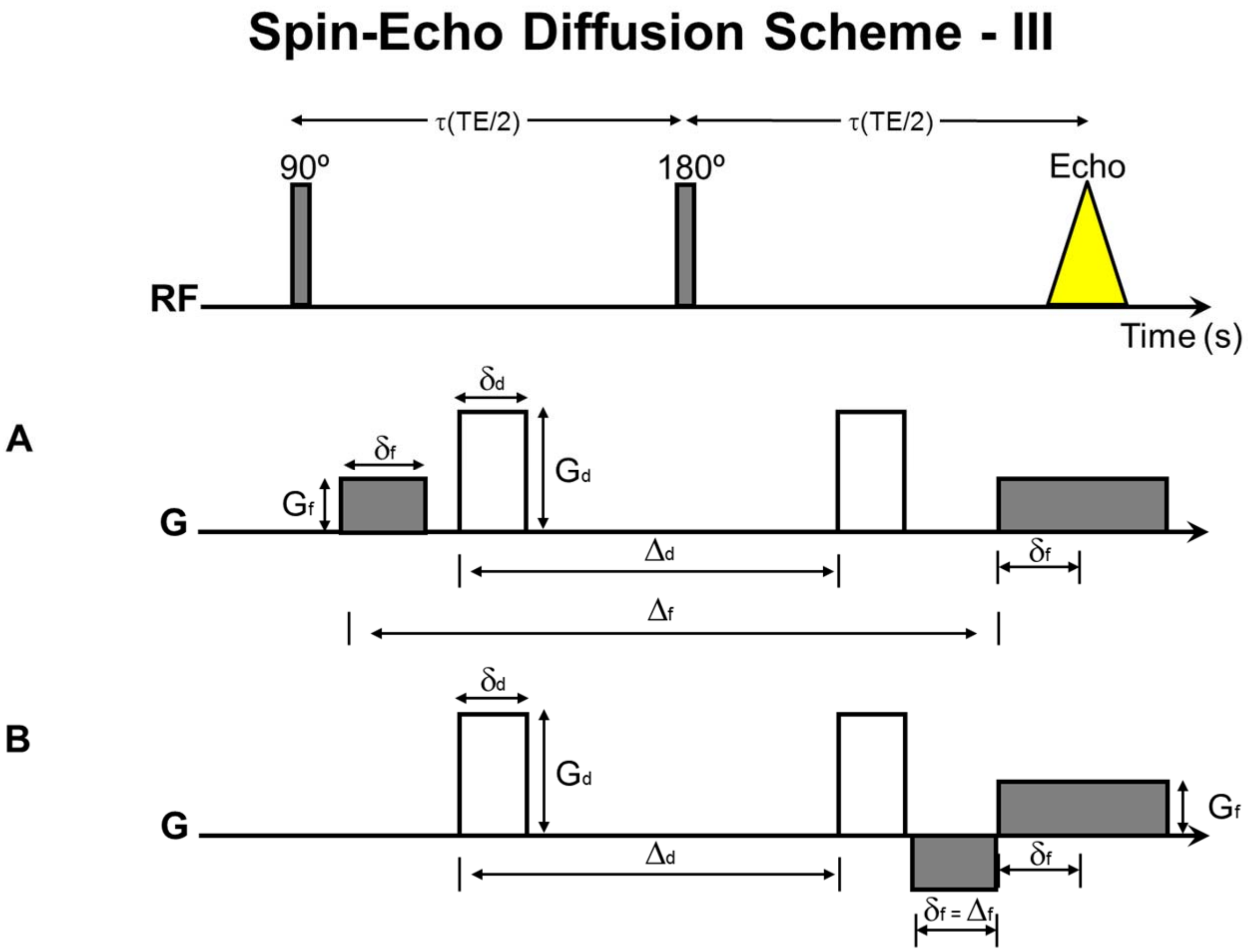

Figure 1–9 The effect of spatial encoding gradient on diffusion measurement.

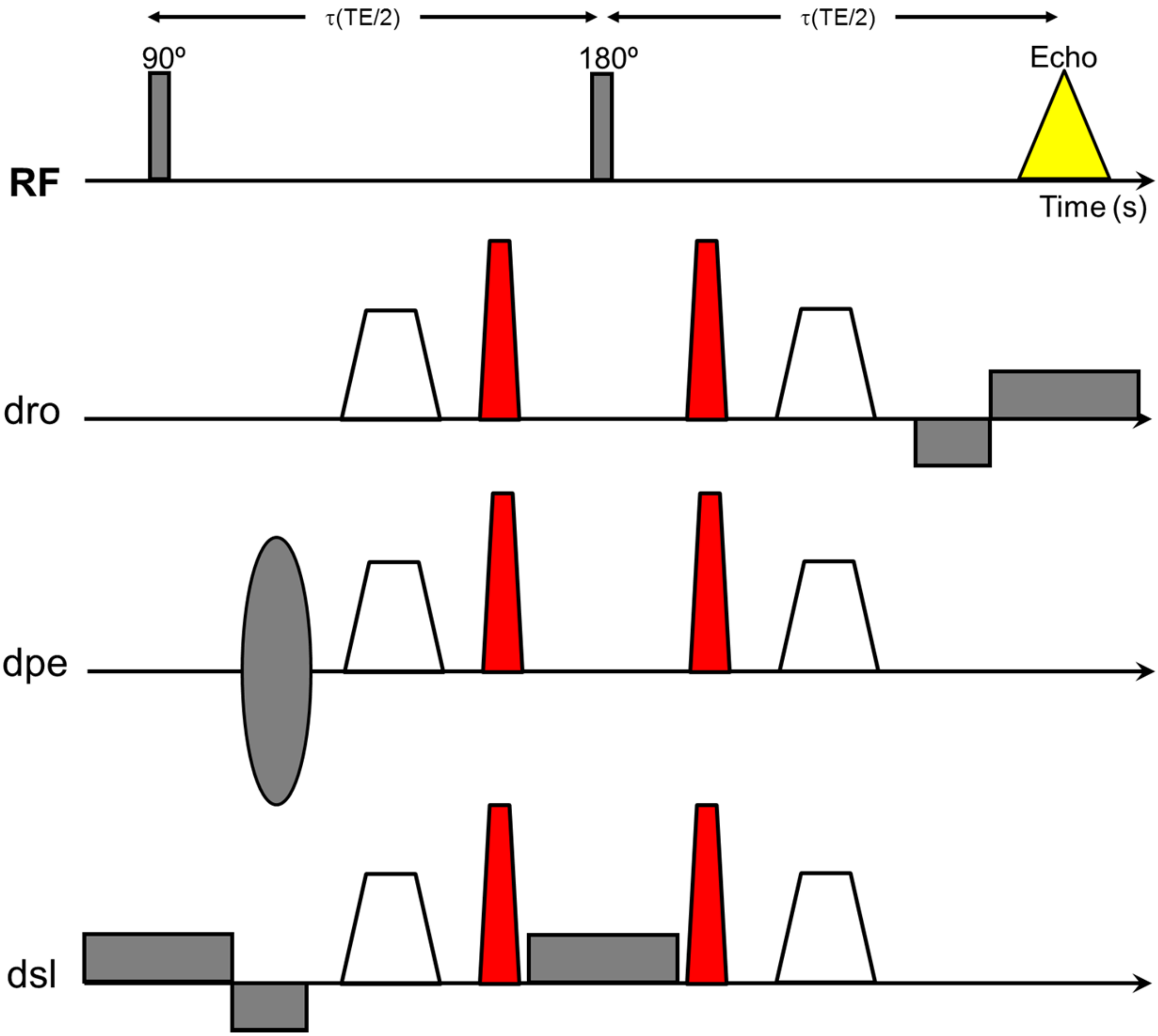

Figure 1–10 Two dimensional spin-echo diffusion sequence with crusher gradients. The white are diffusion sensitizing gradients. The gray are imaging gradients for spatial encoding. The red are crusher gradients.

1.5.4 Biophysical model analysis of non-Gaussian diffusion

In general diffusion MR study is based on Gaussian distribution of diffusion displacement. However we have seen that diffusion attenuated signal intensity varies with respect to the angle between diffusion sensitizing gradient direction and fiber orientation in section 1.5.2 Non-Gaussian diffusion behavior, as measured experimentally in brain tissue [55, 56] and optic nerve [57, 58] is most pronounced with strong diffusion sensitization. It has been observed that the relationship between b-value and diffusion signal deviates from monoexponential behavior if b the value exceeds ~1 ms/μm^2 [56, 57]. This non-Gaussian behavior was first interpreted in terms of contributions of fast and slow diffusing components using biexponential analysis. In earlier literature, the extracellular space was often suggested to correspond to the fast-diffusing component whereas the slower diffusion was ascribed to intracellular space [56, 59, 60].

$$\ln\left[\frac{S(b)}{S(0)}\right] = f_{fast}\exp(-bD_{fast}) + f_{slow}\exp(-bD_{slow}), \text{and } f_{fast} + f_{slow} = 1 \qquad [1-22]$$

in which f and D are the volume fraction and diffusion coefficient, respectively. Regardless of controversy over the physical interpretation of this deviation from monoexponential diffusion signal behavior [56], the multi-exponential analysis allows us to examine the microstructure of CNS in more detail than the Gaussian basis DWI or DTI.

Besides the presence of different diffusion compartments, it is also believed that microstructural barriers producing restricted or hindered diffusion may contribute to non-Gaussian signal behavior. Assaf and Cohen experimentally showed that the mean displacement of fast component linearly increased with diffusion time whereas the mean displacement of slow component reached a plateau regardless increase of diffusion time [61, 62]. Assaf et al. also showed that diffusion displacement of slow diffusion component slightly increased with reduction of physical barrier [63, 64], showing restricted diffusion in CNS. Evidently cell membrane and organelles are most important consideration factor in morphology-based biophysical modeling of the diffusion-weighted signal in white matter. In general, an assumption of restricted diffusion inside of impermeable axon and hindered diffusion in the extracelluar space is made for modeling water diffusion in white-matter structures [65-68]. Another important factor in modeling is the presence of glial cells which are believed to contribute an isotropic restricted diffusion component [57]. Interestingly, most biophysical modeling rarely models this factor [65, 66] or discards the importance of glial cells by assuming that water in glial cells are in fast exchange with the extracellular space [68]. Our recently-developed DBSI multi-compartment model computes the restricted isotropic diffusion signal component, providing a biomarker of cellularity [33].

1.5.5 Suggested working model

DWI and DTI have been widely used to investigate MS patients and rodent EAE models in an effort to account for contributions made by underlying pathology, including inflammation and white matter injury [1, 15, 17, 69-73]. Literature reports have demonstrated that decrease axial diffusivity ($\lambda_{\parallel}$) and increase radial diffusivity ($\lambda_{\perp}$) correlate well with axonal injury and demyelination, respectively (Fig. 1-11) [15, 17, 74]. However, as mentioned in above, the Gaussian diffusion assumption of DTI limits its ability to resolve non-Gaussian aspects of tissue water diffusion. Underestimation of white matter anisotropy in DTI can be caused by crossing fibers, CSF contamination, cell infiltration, edema, tissue loss, etc. [75, 76]. In a microscopically complex diffusion environment, the simplifying assumptions inherent in DTI may cause misleading results.

DBSI has been demonstrated to accurately detect and quantify crossing fibers, axonal injury, demyelination, and inflammation-associated cell infiltration and edema [33]. The key concept is that DBSI models white matter diffusion as a linear combination of multiple discrete anisotropic diffusion tensors describing myelinated axonal tracts and a spectrum of isotropic diffusion describing restricted (cells), non-restricted (extra-axonal space, edema space, and cerebrospinal fluid) diffusion components outside of axonal tracts (Fig. 1-12).

For assessment of acute EAE optic neuritis, the neuropathology may involve coexisting inflammation-related cell infiltration, edema, axonal injury, and demyelination in optic nerve. We will see that the DBSI model analysis, which includes terms that can account for this potentially complicated microenvironment, provides a superior description of water diffusion behavior in acute-stage EAE optic neuritis. In addition, DTI analysis of the same data was performed for valuable comparisons between interpretations yielded by the two types of analyses. (Detailed in Chapter 4)

One potential issue in DBSI is relatively lengthy scan time for in vivo animal study. Application of a time-efficient reduced diffusion scheme without compromising the data quality will be examined in Chapter 3.

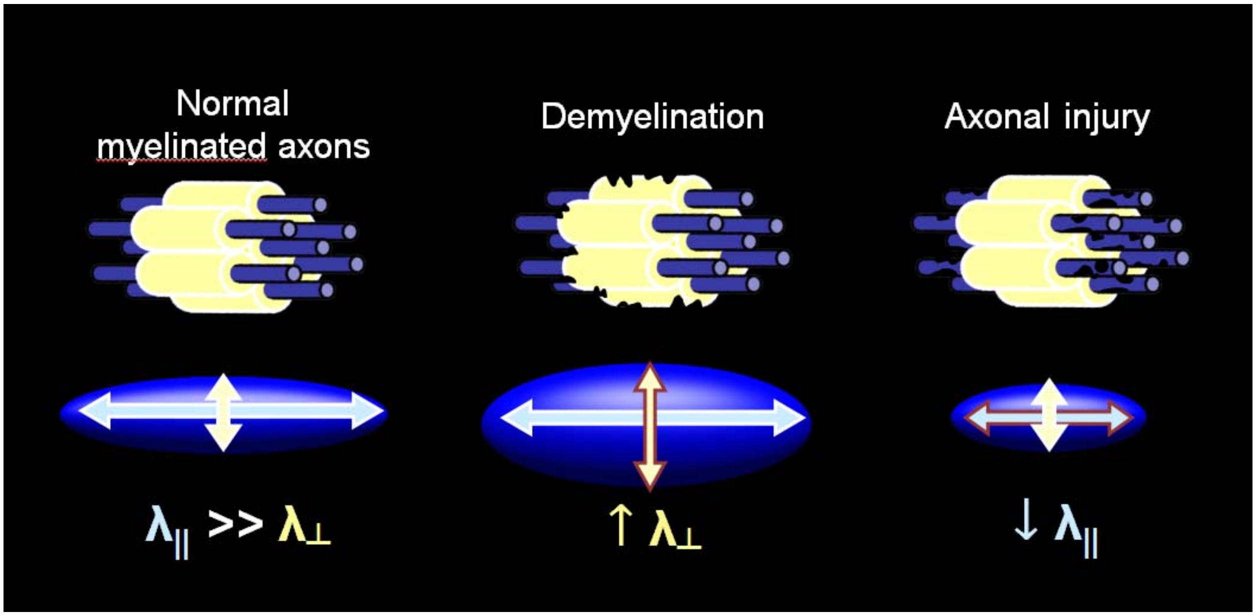

Courtesy from Dr. Matt Budde

Figure 1–11 Directional diffusivities in white matter injury. Normal myelinated axon has larger axial diffusivity ($\lambda_{\parallel}$, diffusivity along the fiber) than radial diffusivity ($\lambda_{\perp}$, diffusivity crossing the fiber). However, demyelination will cause an increased in radial diffusivity, whereas axonal injury results in a decrease in axial diffusivity. Directional diffusivities provide specificity to underlying pathology. Noted that anisotropy (FA) is decreased as well in both situations.

$$S_k = \sum_{i=1}^{N_{Aniso}} f_i e^{-|\overrightarrow{b_k}|\lambda_{\perp i}}\, e^{-|\overrightarrow{b_k}|(\lambda_{\parallel i}-\lambda_{\perp i})\cos^2\psi_{ik}} + \int_a^b f(D) e^{-|\overrightarrow{b_k}|D} dD \quad (k = 1, 2, 3, \dots)$$

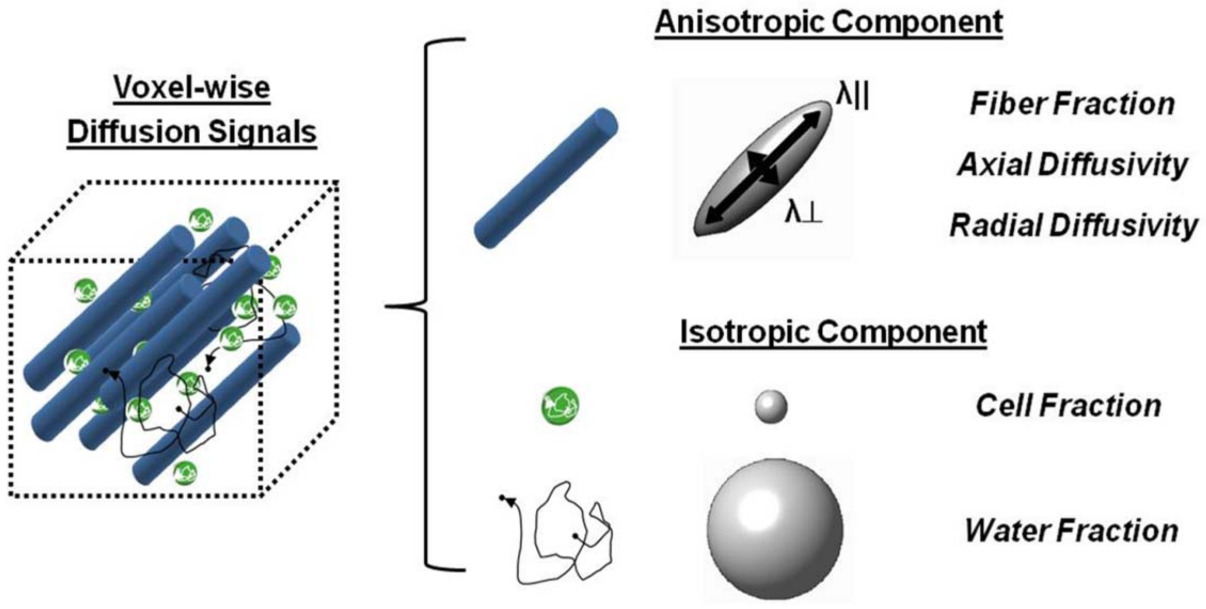

Courtesy from Dr. Tsang-Wei Tu

Figure 1–12 DBSI multi-compartment model computes anisotropic, restricted, and non-restricted isotropic diffusion components, reflecting myelinated axon, cellularity, and extra-axonal and extracellular space, respectively.

1.6 References

1. Ahrens, E.T., et al., *MR microscopy of transgenic mice that spontaneously acquire experimental allergic encephalomyelitis.* Magn Reson Med, 1998. **40**(1): p. 119-32.

2. Reipert, B., *Multiple sclerosis: a short review of the disease and its differences between men and women.* The Journal of Men's Health & Gender, 2004. **1**(4): p. 334-40.

3. Kornek, B. and H. Lassmann, *Neuropathology of multiple sclerosis-new concepts.* Brain Res Bull, 2003. **61**(3): p. 321-6.

4. Kornek, B., et al., *Multiple sclerosis and chronic autoimmune encephalomyelitis: a comparative quantitative study of axonal injury in active, inactive, and remyelinated lesions.* Am J Pathol, 2000. **157**(1): p. 267-76.

5. Whitney, L.W., et al., *Analysis of gene expression in mutiple sclerosis lesions using cDNA microarrays.* Ann Neurol, 1999. **46**(3): p. 425-8.

6. Noseworthy, J.H., et al., *Multiple sclerosis.* N Engl J Med, 2000. **343**(13): p. 938-52.

7. Trapp, B.D. and P.K. Stys, *Virtual hypoxia and chronic necrosis of demyelinated axons in multiple sclerosis.* Lancet Neurol, 2009. **8**(3): p. 280-91.

8. Osborne, B.J. and N.J. Volpe, *Optic neuritis and risk of MS: differential diagnosis and management.* Cleve Clin J Med, 2009. **76**(3): p. 181-90.

9. Zuvich, R.L., et al., *Genetics and pathogenesis of multiple sclerosis.* Semin Immunol, 2009. **21**(6): p. 328-33.

10. Baker, D. and D.J. Hankey, *Gene therapy in autoimmune, demyelinating disease of the central nervous system.* Gene Ther, 2003. **10**(10): p. 844-53.

11. Guan, Y., et al., *Retinal ganglion cell damage induced by spontaneous autoimmune optic neuritis in MOG-specific TCR transgenic mice.* J Neuroimmunol, 2006. **178**(1-2): p. 40-8.

12. Quinn, T.A., M. Dutt, and K.S. Shindler, *Optic neuritis and retinal ganglion cell loss in a chronic murine model of multiple sclerosis.* Front Neurol, 2011. **2**: p. 50.

13. Matsunaga, Y., et al., *Visual functional and histopathological correlation in experimental autoimmune optic neuritis.* Invest Ophthalmol Vis Sci, 2012. **53**(11): p. 6964-71.

14. Hobom, M., et al., *Mechanisms and time course of neuronal degeneration in experimental autoimmune encephalomyelitis.* Brain Pathol, 2004. **14**(2): p. 148-57.

15. Sun, S.W., et al., *Selective vulnerability of cerebral white matter in a murine model of multiple sclerosis detected using diffusion tensor imaging.* Neurobiol Dis, 2007. **28**(1): p. 30-8.

16. Kezuka, T., Y. Usui, and H. Goto, *Analysis of the pathogenesis of experimental autoimmune optic neuritis.* J Biomed Biotechnol, 2011. **2011**: p. 294046.

17. Budde, M.D., et al., *Axonal injury detected by in vivo diffusion tensor imaging correlates with neurological disability in a mouse model of multiple sclerosis.* NMR Biomed, 2008. **21**(6): p. 589-97.

18. Shams, P.N. and G.T. Plant, *Optic neuritis: a review.* Int MS J, 2009. **16**(3): p. 82-9.

19. Fisher, J.B., et al., *Relation of visual function to retinal nerve fiber layer thickness in multiple sclerosis.* Ophthalmology, 2006. **113**(2): p. 324-32.

20. Burkholder, B.M., et al., *Macular volume determined by optical coherence tomography as a measure of neuronal loss in multiple sclerosis.* Arch Neurol, 2009. **66**(11): p. 1366-72.

21. Brusa, A., S.J. Jones, and G.T. Plant, *Long-term remyelination after optic neuritis: A 2-year visual evoked potential and psychophysical serial study.* Brain, 2001. **124**(Pt 3): p. 468-79.

22. Prusky, G.T., et al., *Rapid quantification of adult and developing mouse spatial vision using a virtual optomotor system.* Invest Ophthalmol Vis Sci, 2004. **45**(12): p. 4611-6.

23. Douglas, R.M., et al., *Independent visual threshold measurements in the two eyes of freely moving rats and mice using a virtual-reality optokinetic system.* Vis Neurosci, 2005. **22**(5): p. 677-84.

24. Grossman, R.I., et al., *Multiple sclerosis: serial study of gadolinium-enhanced MR imaging.* Radiology, 1988. **169**(1): p. 117-22.

25. Meyer, R., et al., *Acute neuronal apoptosis in a rat model of multiple sclerosis.* J Neurosci, 2001. **21**(16): p. 6214-20.

26. Stefferl, A., et al., *Myelin oligodendrocyte glycoprotein induces experimental autoimmune encephalomyelitis in the "resistant" Brown Norway rat: disease susceptibility is determined by MHC and MHC-linked effects on the B cell response.* J Immunol, 1999. **163**(1): p. 40-9.

27. Enriquez-Algeciras, M., et al., *Evaluation of a transgenic mouse model of multiple sclerosis with noninvasive methods.* Invest Ophthalmol Vis Sci, 2011. **52**(5): p. 2405-11.

28. Syc, S.B., et al., *Optical coherence tomography segmentation reveals ganglion cell layer pathology after optic neuritis.* Brain, 2012. **135**(Pt 2): p. 521-33.

29. Owens, T., *The enigma of multiple sclerosis: inflammation and neurodegeneration cause heterogeneous dysfunction and damage.* Curr Opin Neurol, 2003. **16**(3): p. 259-65.

30. Qi, X., et al., *Suppression of mitochondrial oxidative stress provides long-term neuroprotection in experimental optic neuritis.* Invest Ophthalmol Vis Sci, 2007. **48**(2): p. 681-91.

31. Vellinga, M.M., et al., *Pluriformity of inflammation in multiple sclerosis shown by ultra-small iron oxide particle enhancement.* Brain, 2008. **131**(Pt 3): p. 800-7.

32. Hickman, S.J., et al., *A serial MRI study following optic nerve mean area in acute optic neuritis.* Brain, 2004. **127**(Pt 11): p. 2498-505.

33. Wang, Y., et al., *Quantification of increased cellularity during inflammatory demyelination.* Brain, 2011. **134**(Pt 12): p. 3590-601.

34. Plewes, D.B. and W. Kucharczyk, *Physics of MRI: a primer.* J Magn Reson Imaging, 2012. **35**(5): p. 1038-54.

35. Hahn, E.L., *Spin Echoes.* Physical Review, 1950. **80**: p. 580-594.

36. Carr, H.Y. and E.M. Purcell, *Effects of diffusion on free precession in nuclear magnetic resonance experiments.* Physical Review, 1954. **94**: p. 630-638.

37. Stejskal, E.T., JE., *Spin Echoes in the Presence of a Time-Dependent Field Gradient.* The Journal of Chemical Physics, 1965. **42(1)**: p. 288-292.

38. Torrey, H., *Bloch equations with diffusion terms.* Physical Review, 1956. **104**: p. 563-565.

39. Bloch, F., *Neuclear inductionn.* Physical Review, 1946. **70**: p. 460-474.

40. Abragam, A., *The Principles of Nuclear Magnetism.* Clarendon, Press, Oxford, 1961.

41. Basser, P.J., J. Mattiello, and D. LeBihan, *Estimation of the effective self-diffusion tensor from the NMR spin echo.* J Magn Reson B, 1994. **103**(3): p. 247-54.

42. Tanner, J.E., *Self diffusion of water in frog muscle.* Biophys J, 1979. **28**(1): p. 107-16.

43. Tanner, J.E., *Intracellular diffusion of water.* Arch Biochem Biophys, 1983. **224**(2): p. 416-28.

44. Cleveland, G.G., et al., *Nuclear magnetic resonance measurement of skeletal muscle: anisotrophy of the diffusion coefficient of the intracellular water.* Biophys J, 1976. **16**(9): p. 1043-53.

45. Moseley, M.E., et al., *Diffusion-weighted MR imaging of anisotropic water diffusion in cat central nervous system.* Radiology, 1990. **176**(2): p. 439-45.

46. Moseley, M.E., et al., *Anisotropy in diffusion-weighted MRI.* Magn Reson Med, 1991. **19**(2): p. 321-6.

47. Le Bihan, D., *Diffusion and perfusion magnetic resonance imaging: Applications to Funtional MRI*1995, New York: Raven Press.

48. Mattiello, J., P.J. Basser, and D. Le Bihan, *The b matrix in diffusion tensor echo-planar imaging.* Magn Reson Med, 1997. **37**(2): p. 292-300.

49. Basser, P.J., *Inferring microstructural features and the physiological state of tissues from diffusion-weighted images.* NMR Biomed, 1995. **8**(7-8): p. 333-44.

50. Pajevic, S. and C. Pierpaoli, *Color schemes to represent the orientation of anisotropic tissues from diffusion tensor data: application to white matter fiber tract mapping in the human brain.* Magn Reson Med, 1999. **42**(3): p. 526-40.

51. Jones, D.K., *Diffusion MRI.* Oxford University Press, 2011.

52. Jones, D.K., et al., *Non-invasive assessment of axonal fiber connectivity in the human brain via diffusion tensor MRI.* Magn Reson Med, 1999. **42**(1): p. 37-41.

53. Mori, S., et al., *Three-dimensional tracking of axonal projections in the brain by magnetic resonance imaging.* Ann Neurol, 1999. **45**(2): p. 265-9.

54. Basser, P.J., et al., *In vivo fiber tractography using DT-MRI data.* Magn Reson Med, 2000. **44**(4): p. 625-32.

55. Assaf, Y. and Y. Cohen, *In vivo and in vitro bi-exponential diffusion of N-acetyl aspartate (NAA) in rat brain: a potential structural probe?* NMR Biomed, 1998. **11**(2): p. 67-74.

56. Assaf, Y. and Y. Cohen, *Non-mono-exponential attenuation of water and N-acetyl aspartate signals due to diffusion in brain tissue.* J Magn Reson, 1998. **131**(1): p. 69-85.

57. Stanisz, G.J., et al., *An analytical model of restricted diffusion in bovine optic nerve.* Magn Reson Med, 1997. **37**(1): p. 103-11.

58. Stanisz, G.J. and R.M. Henkelman, *Diffusional anisotropy of T2 components in bovine optic nerve.* Magn Reson Med, 1998. **40**(3): p. 405-10.

59. Mulkern, R.V., et al., *Multi-component apparent diffusion coefficients in human brain.* NMR Biomed, 1999. **12**(1): p. 51-62.

60. Niendorf, T., et al., *Biexponential diffusion attenuation in various states of brain tissue: implications for diffusion-weighted imaging.* Magn Reson Med, 1996. **36**(6): p. 847-57.

61. Assaf, Y., A. Mayk, and Y. Cohen, *Displacement imaging of spinal cord using q-space diffusion-weighted MRI.* Magn Reson Med, 2000. **44**(5): p. 713-22.

62. Assaf, Y. and Y. Cohen, *Assignment of the water slow-diffusing component in the central nervous system using q-space diffusion MRS: implications for fiber tract imaging.* Magn Reson Med, 2000. **43**(2): p. 191-9.

63. Assaf, Y., et al., *Changes in axonal morphology in experimental autoimmune neuritis as studied by high b-value q-space (1)H and (2)H DQF diffusion magnetic resonance spectroscopy.* Magn Reson Med, 2002. **48**(1): p. 71-81.

64. Assaf, Y., et al., *High b-value q-space analyzed diffusion-weighted MRI: application to multiple sclerosis.* Magn Reson Med, 2002. **47**(1): p. 115-26.

65. Assaf, Y. and P.J. Basser, *Composite hindered and restricted model of diffusion (CHARMED) MR imaging of the human brain.* Neuroimage, 2005. **27**(1): p. 48-58.

66. Alexander, D.C., *A general framework for experiment design in diffusion MRI and its application in measuring direct tissue-microstructure features.* Magn Reson Med, 2008. **60**(2): p. 439-48.

67. Panagiotaki, E., et al., *Compartment models of the diffusion MR signal in brain white matter: a taxonomy and comparison.* Neuroimage, 2012. **59**(3): p. 2241-54.

68. Fieremans, E., J.H. Jensen, and J.A. Helpern, *White matter characterization with diffusional kurtosis imaging.* Neuroimage, 2011. **58**(1): p. 177-88.

69. DeBoy, C.A., et al., *High resolution diffusion tensor imaging of axonal damage in focal inflammatory and demyelinating lesions in rat spinal cord.* Brain, 2007. **130**(Pt 8): p. 2199-210.

70. Wu, Q., et al., *MR diffusion changes correlate with ultra-structurally defined axonal degeneration in murine optic nerve.* Neuroimage, 2007. **37**(4): p. 1138-47.

71. Inglese, M. and M. Bester, *Diffusion imaging in multiple sclerosis: research and clinical implications.* NMR Biomed, 2010. **23**(7): p. 865-72.

72. Ge, Y., *Multiple sclerosis: the role of MR imaging.* AJNR Am J Neuroradiol, 2006. **27**(6): p. 1165-76.

73. Budde, M.D., et al., *Axial diffusivity is the primary correlate of axonal injury in the experimental autoimmune encephalomyelitis spinal cord: a quantitative pixelwise analysis.* J Neurosci, 2009. **29**(9): p. 2805-13.

74. Song, S.K., et al., *Dysmyelination revealed through MRI as increased radial (but unchanged axial) diffusion of water.* Neuroimage, 2002. **17**(3): p. 1429-36.

75. Papadakis, N.G., et al., *Study of the effect of CSF suppression on white matter diffusion anisotropy mapping of healthy human brain.* Magn Reson Med, 2002. **48**(2): p. 394-8.

76. Alexander, D.C., et al., *Spatial transformations of diffusion tensor magnetic resonance images*. IEEE Trans Med Imaging, 2001. **20**(11): p. 1131-9.

Chapter 2

Quantitative analysis of immunohistochemical staining

2.1 Introduction

Diffusion magnetic resonance imaging has shown potential to reflect microstructure in the central nervous system (CNS) of living subjects in both preclinical and clinical applications [1-4]. In particular, white matter consisting of coherently-bundled long cylindrical axons wrapped tightly by myelin sheaths is characterized by a high anisotropy in diffusion maps, Fig. 2 – 1 [5, 6]. In addition, there have been many reports in the literature suggesting that diffusion-imaging-derived parameters may reflect pathophysiology of white matter in cases of neurodegenerative disease or injury [7, 8, 2, 9-13]. Recently, diffusion basis spectrum imaging (DBSI) was developed for identifying cellularity in white matter [14, 15]. Even though diffusion imaging may reflect morphology or pathophysiology of white matter non-invasively, the observed in vivo or even ex vivo MR findings require accurate and precise validation. Postmortem immunohistochemical (IHC) staining is a gold-standard methodology for identifying and quantifying neuropathology (http://www.nsh.org). IHC is often used to validate in vivo MRI findings on the CNS, especially white matter [16, 14, 17-21].

In this study, we utilized phosphorylated neurofilament (SMI-31, intact axon), myelin basic protein (MBP, myelin sheath), and 4’, 6-diamidino-2-phenlindole (DAPI, nuclei) IHC staining as a reflection of integrity of mouse optic nerve. Following staining for the relevant proteins of interest, IHC data should be analyzed quantitatively for validation of in vivo MR data. Enumeration of the positive signals in IHC staining is commonly used to provide quantitative measurements. However, most counting is done manually or with limited automation. Thus, accurate and, most importantly, objective quantitative method to examine histological findings is critical to validate MR findings. In this chapter, objective and reliable quantification methods for various IHC have been addressed.

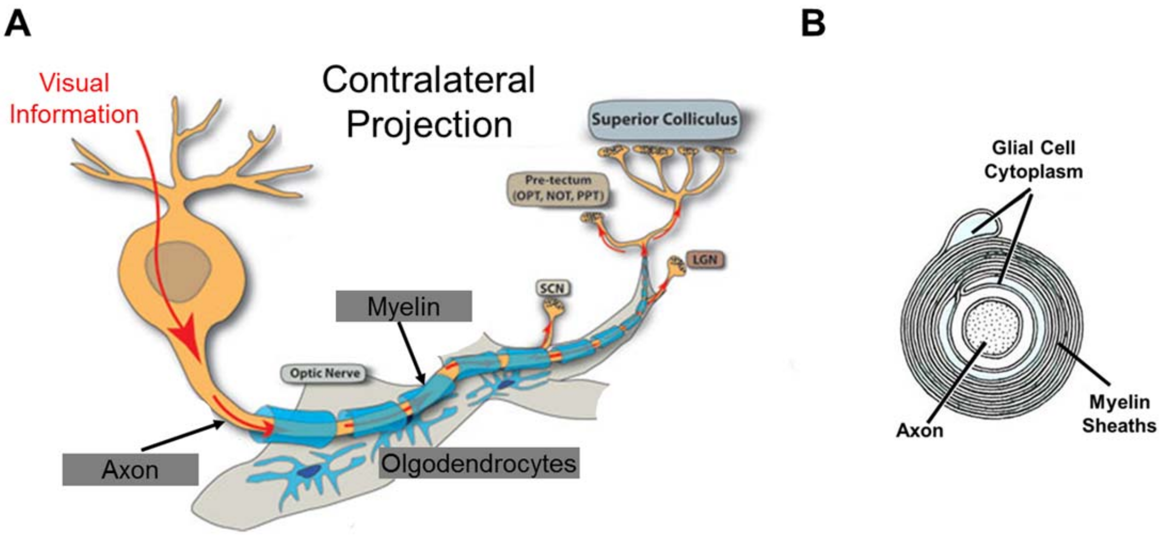

Figure 2–1 The visual system and structure of optic nerve. The visual information received in cell body is transported through myelinated axon (A). The anatomical structure optic nerve in axial plane is clearly seen (B). The donut-ring shaped myelin sheaths wraps around axon tightly.

Panel A: http://www.vanderbilthealth.com/eyeinstitute/23604
Panel B: Nicholls, John G, Martin, Robert A., Wallace, Bruce G., Fuchs, Paul A. *From Neuron to Brain*. 2nd ed. Sunderland, MA: Sinauer Associates, 2001. 327. Print.

2.2 Tissue preparation and IHC staining

IHC encompasses a range of staining methods to detect specific antigens, mostly proteins, by interaction between antibody and exploring the principle antibody (See Fig. 2 – 2 A) [22-25]. Fluorescent molecules (or fluorophores) are frequently used as labels in antibodies to reflect IHC staining effect. In brief, the electrons of fluorophore absorb energy from excitation light and re-emit light by a longer wavelength (Fig. 2 – 2 B) due to energy dissipation of surrounding molecule interaction.

At the end of in vivo MRI study (described further in Chapter 4) animals underwent cardiac perfusion fixation with 0.01M Phosphate buffered saline (PBS, Sigma-Aldrich, MO, USA) followed by 4 % paraformaldehyde (PFA, Sigma-Aldrich, MO, USA). The volumes of PBS and PFA were determined by body weight of animal in 1ml/g ratio to avoid over fixation, which may damage tissue. After perfusion/fixation, all tissue underwent over-night postmortem fixation in 4 % PFA. Then the harvested tissues were embedded in paraffin wax blocks and sectioned into 5-µm-thick slices using a microtome. IHC staining protocols were carried out according as described previously [26-29]. Briefly, sectioned slices were deparaffinized and rehydrated to facilitate binding of antibodies and then blocked by the solution mixed with 1% bovine serum albumin (BSA, Sigma-Aldrich, MO, US) and 5% normal goat-serum solution (Invitrogen, CA, USA) for 20 minutes at room temperature to prevent non-specific binding and to increase antibody permeability. Next, slices were incubated at 4˚C overnight in monoclonal anti-phosphorylated neurofilament antibody (SMI-31, 1:1000, Covance, NJ, USA) or rabbit myelin basic protein antibody (MBP, 1:1000, Sigma-Aldrich, MO, USA) to stain for intact axons or myelin sheaths, respectively. After rising, goat anti-mouse IgG and goat anti-rabbit conjugated Alexa 488 (1:800, Invitrogen, CA, USA) were applied to visualize immunoreactivity of phosphorylated neurofilament and myelin basic protein. Finally, slices were covered using Vectashield Mounting Medium with 4’,6-diamidino-2-phenylindole (DAPI) (Vector Laboratory, Inc., CA, USA). After each staining, digital images were taken with a fluorescence microscope (Nikon Eclipse 80i, USA), using identical light intensity and exposure time settings. Identical intensity scales were used for all digital images. The captured images were saved as 16-bit gray scale images for quantitative analysis. Quantification of IHC-positive staining was performed using ImageJ 1.46r (http://rsbweb.nih.gov/ij/) and related plugins. The digitally-captured images were loaded as gray scale with black background, zero value.

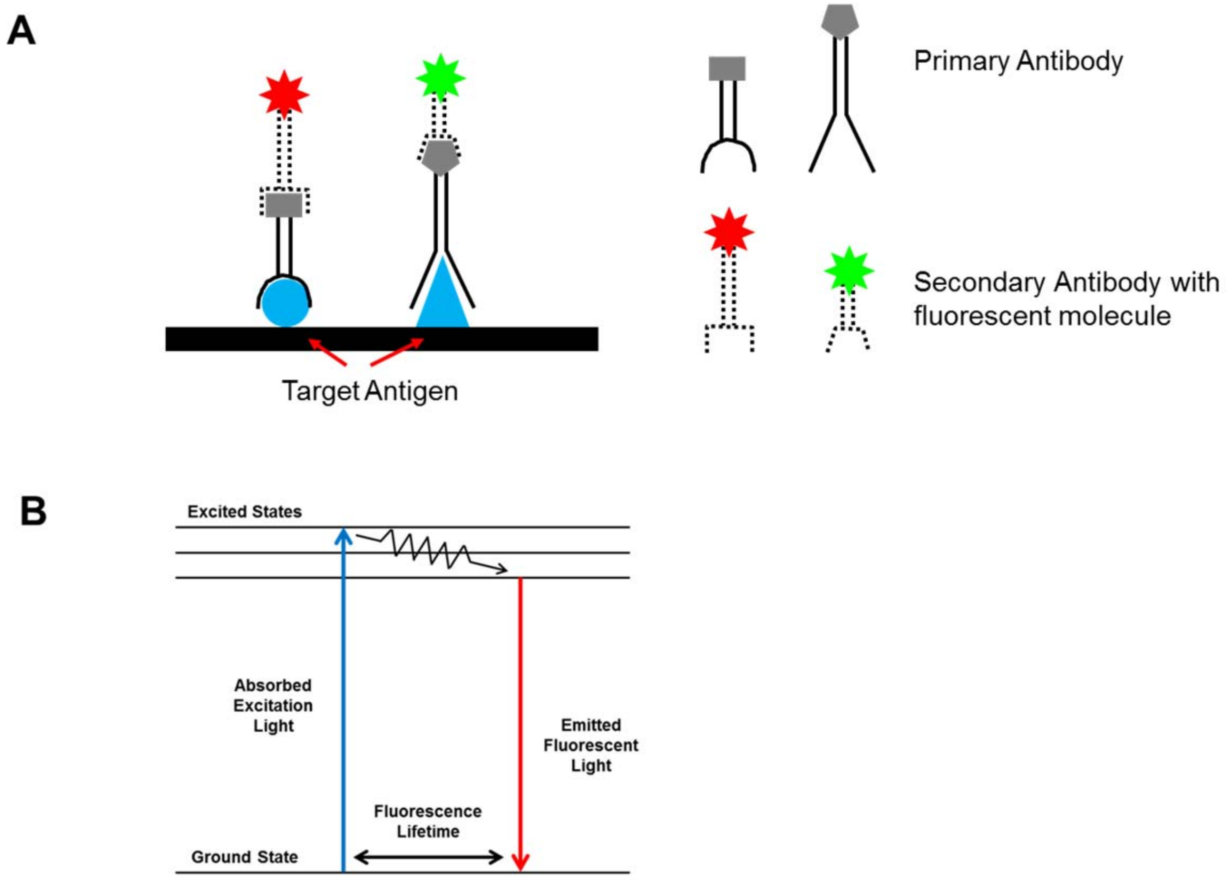

Figure 2–2 Immunohistochemical (IHC) stain. The mechanism of IHC stain is shown in a with a cartoon figure (A). The primary antibody interacts with target antigen protein whereas the secondary antibody binds to the primary antibody. Fluorescent molecules (the red or green color star symbols) are frequently incorporated into secondary antibodies as a label antigen-antibody interaction. Panel B shows the energy-level diagram for the fluorescent moiety. Excitation of the fluorophore-labeled tissue sample with a specific wavelength of light results in a spatially-variable fluorescence emission at a longer wavelength. The spatial distribution of fluorescence emission in the micrograph acquired at this longer wavelength is interpreted as reflecting the distribution of the target antigen in the tissue sample.

2.3 Quantification of nuclei using DAPI

4',6-diamidino-2-phenylindole (DAPI) was used to stain cell nuclei in optic nerves. A representative DAPI-stained mouse optic nerve is shown in Fig. 2 – 3. In general DAPI stain is highly prominent, so the signal-to-noise ratio (SNR) between DAPI positive objects vs. background is quite high (see Fig. 2 – 3) enabling direct threshold without further post-processing. To select only DAPI positive nuclei, an iterative procedure based on the Isodata threshold algorithm was used [30]. This algorithm defines the threshold as threshold = (average background + average objects)/2. First, 16-bit gray scale image was converted into 8-bit and then image was divided into object and background by taking an initial threshold the averages of the pixels above threshold and pixels at or below threshold are computed. After this, the averages of those two averaged values were computed. The threshold was again incremented and the process was repeated until the threshold was larger than the composite average reaching the condition, threshold = (average background + average objects)/2. The Isodata threshold was performed on 8-bit gray scale. Once thresholds were determined, positive objects were quantified using ImageJ particle analysis, http://rsbweb.nih.gov/ij/docs/menus/analyze.html, See Fig. 2 – 4. Using the addressed protocol, DAPI-positive nuclei were successfully enumerated showing severity of pathology of EAE mouse optic nerve, severe inflammation induced cell infiltration (Fig. 2 – 5).

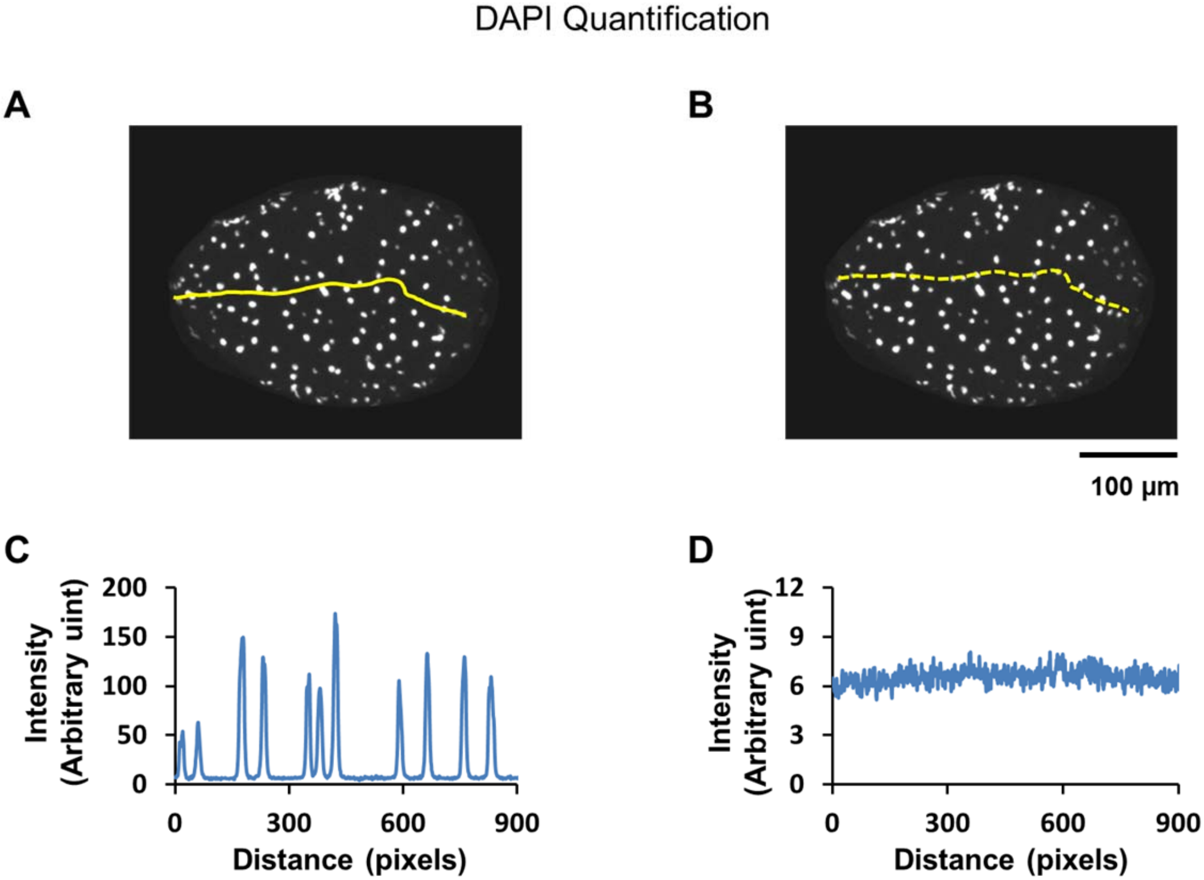

Figure 2–3 DAPI stain on mouse optic nerve and one dimensional intensity profile. Nuclei of cell bodies in mouse optic nerve are shown with DAPI stain at 20x magnification (A and B). The one dimensional intensity profile is shown for DAPI positive nuclei (C, solid line in A) and background (D, dashed line in B).

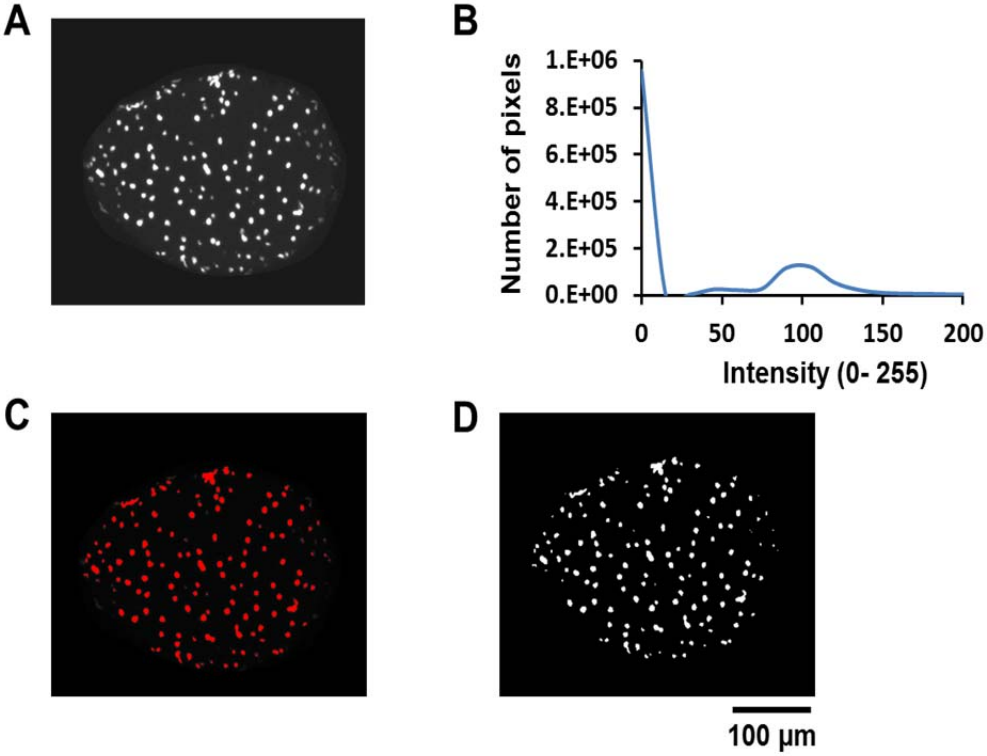

Figure 2–4 Quantification of DAPI uses iterative selection threshold. The intensity histogram of whole optic nerve having DAPI stain (A) is shown in B. DAPI positive nuclei intensity is distinct from background signal (B). Panel C shows object above threshold obtained from IsoData algorithm and panel D shows the final product of quantification.

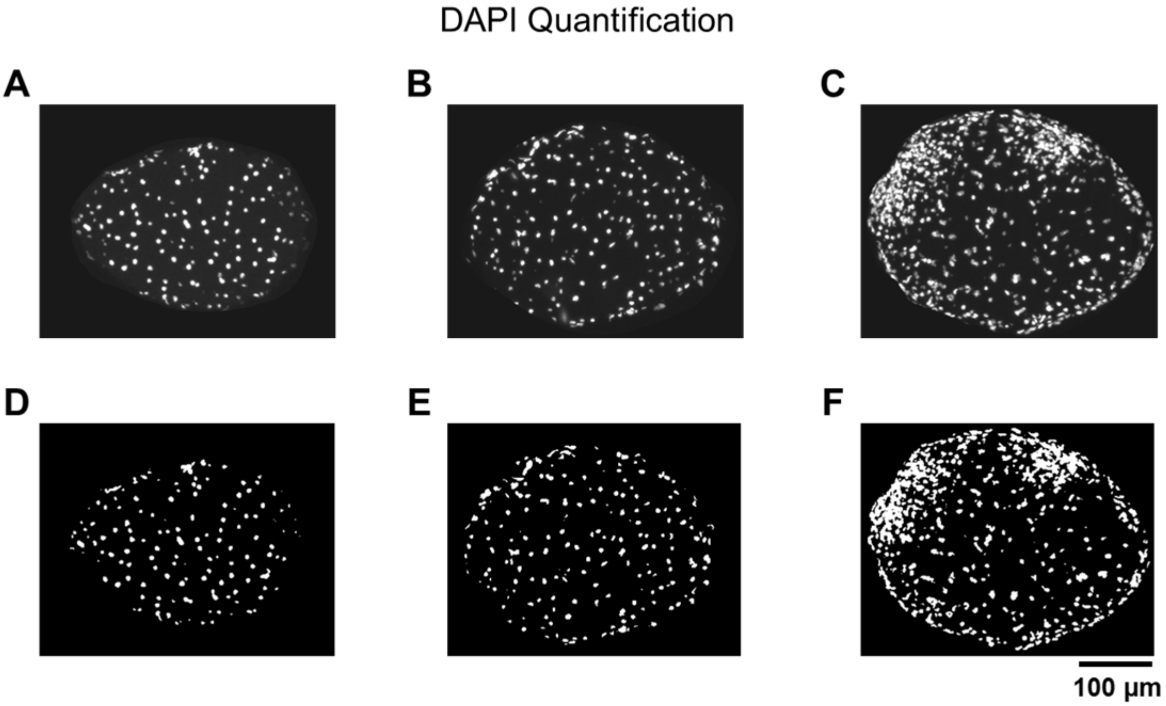

Figure 2–5 Representative DAPIs on mice optic nerves and quantified nuclei map. The raw DAPI images (20x) of mouse optic nerves having mild (B) and severe (C) inflammation including control (A) are shown. Panel D (control), E (mild), and F (severe) are quantified DAPI positive nuclei maps, and results show 120, 179, and 266 counts, respectively.

2.4 Quantification of SMI-32

In general healthy axons have phosphorylated neurofilaments supporting axonal transport [31]. Damaged axons were examined using non-phosphorylated neurofilament positive IHC, SMI-32. A representative SMI-32 EAE mouse optic nerve is shown in Fig. 2 – 6. Unlike DAPI, SMI-32 produced a strong background signal. This required application of a background signal removal process prior to threshold application. The background signal was removed using the ImageJ plugin, rolling ball algorithm, http://rsbweb.nih.gov/ij/plugins/rolling-ball.html [32, 33]. Background signal subtraction was performed on 16-bit gray scale images. Briefly, the signal-intensity profiles of whole 2D images were obtained in both horizontal and vertical directions, Fig. 2 – 6 C. The process of obtaining intensity profile is like rolling a ball along each direction and getting the intensity value. During this process, one should be aware of pixel size. If the intensity profile is obtained per each pixel, or with a very small ball size, the obtained intensity profile would be too noisy, preventing accurate background subtraction. To avoid this kind of problem, appropriate pixel size (or ball size) should be applied. In this study, the pixel size of the SMI-32-positive objective was determined manually from the digital microscope image. The appropriate pixel size would vary depending on magnification of the digital image. In our experience the appropriate pixel size has a radius equal to that of the positive object. Once the intensity profile was obtained, the background was subtracted easily. Figure 2 – 6 shows the intensity profile before and after background signal subtraction. The addressed protocol successfully removed background signal but preserved IHC (SMI-32) positive objects. After background subtraction, image was converted into 8-bit gray scale and then the SMI-32 positive objects were selected using IsoData threshold and enumerated by ImageJ particle analysis ,http://rsbweb.nih.gov/ij/docs/menus/analyze.html, See also section of 2.3. Figure 2 – 7 shows the quantified SMI-32 without and with background subtraction. The strong background signal without background subtraction caused huge amount of false positive SMI-32 counts. EAE mice optic nerves having different severities of axonal damage could be differentiated using this protocol of SMI-32 quantification, Fig. 2 – 8.

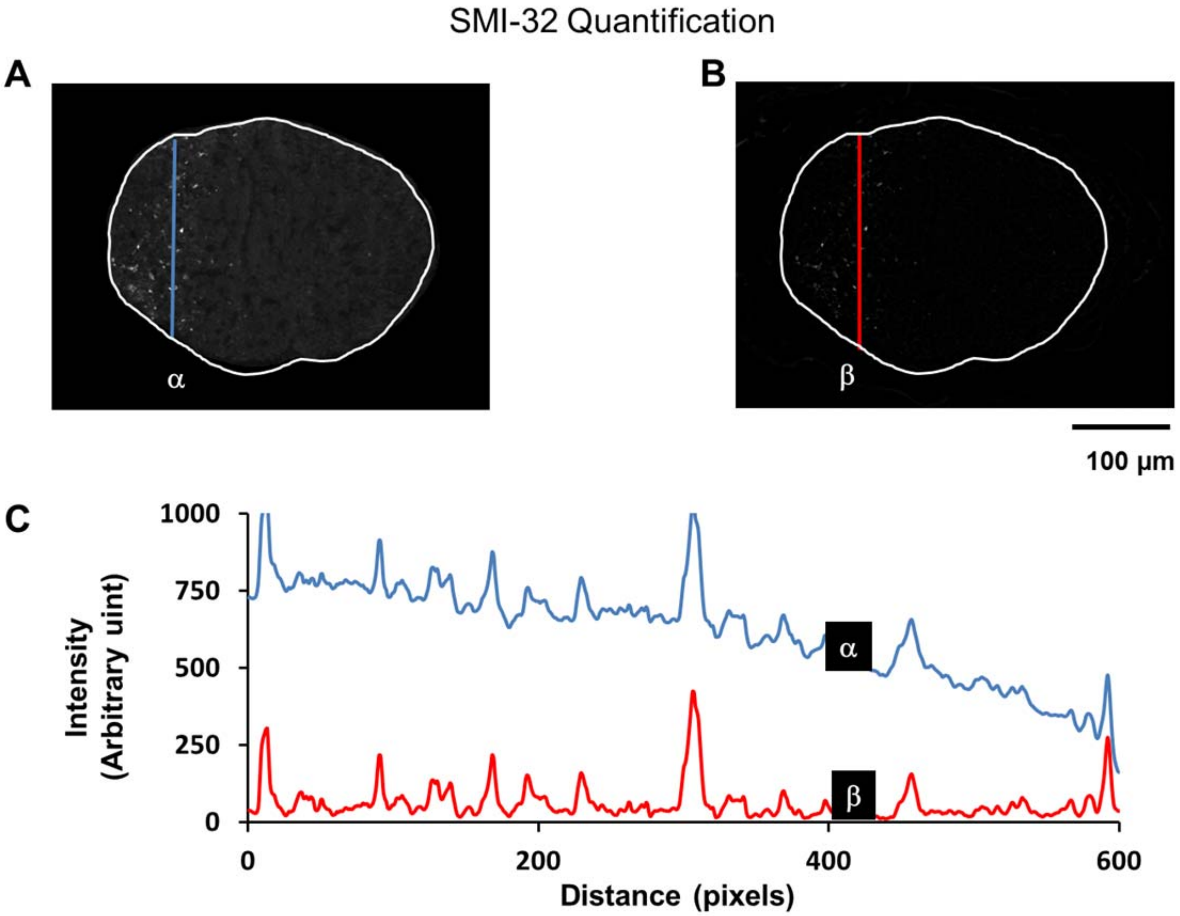

Figure 2–6 Non-phosphorylated neurofilament stain (SMI-32) on mouse optic nerve and one dimensional intensity profile. The SMI-32 stain on mouse optic nerve is shown in A (raw image) and B (image with background intensity subtraction), 20x magnification. The panel A and B are in same intensity scale. The panel C shows intensity profile without (α) and with (β) background signal subtraction using rolling ball method. The background signal intensity is reduced by a factor of 500 - 600.

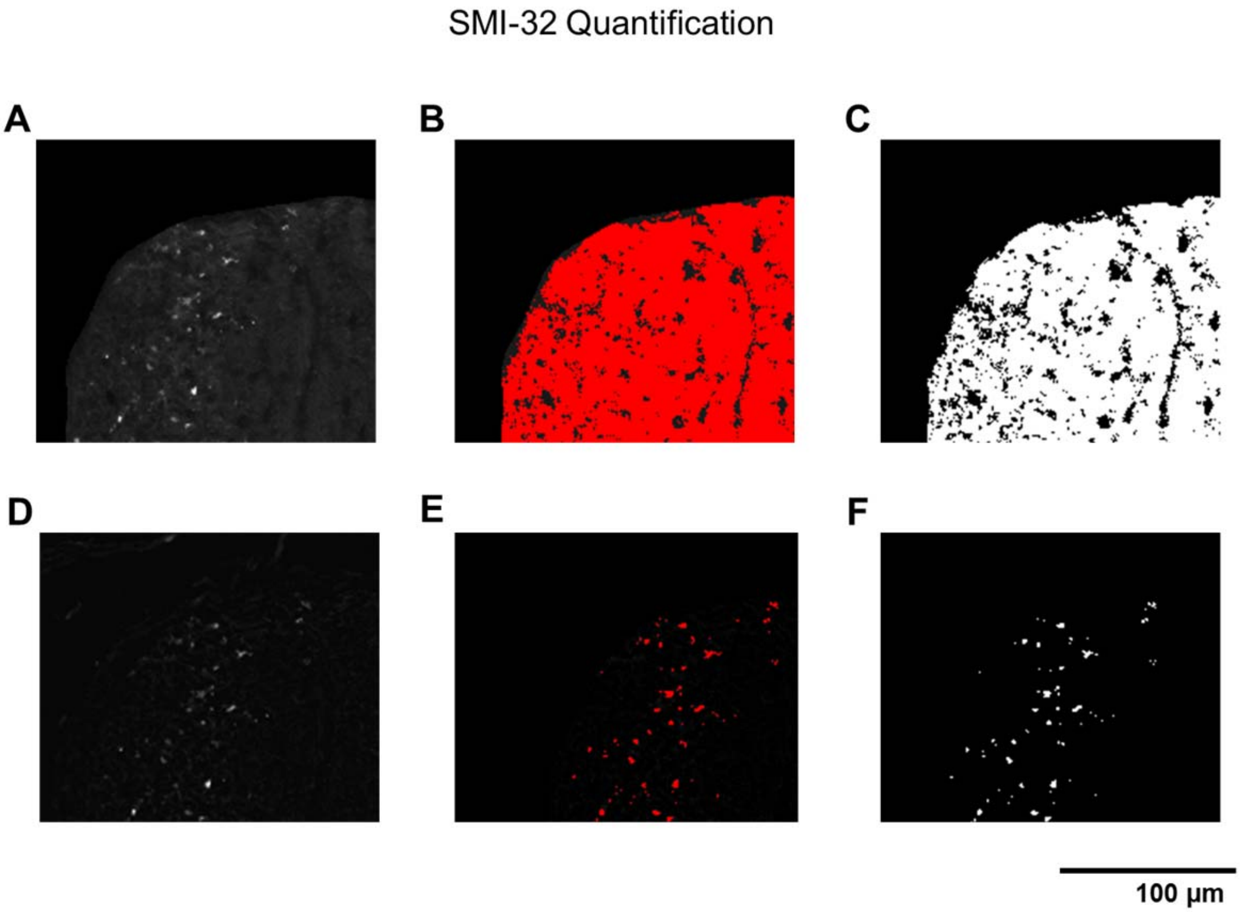

Figure 2–7 Quantification of SMI-32 positive axons using iterative selection threshold (IsoData) without (panel A - C) and with (panel D - F) background signal subtraction (rolling ball algorithm). The panel A - F are from the same raw image. Without background signal removal (A) whole optic nerve is selected as SMI-32 positive objects using iterative selection threshold (panel B and C). With background signal suppression (panel D) only SMI-32 true positive axons are selected as objects (panel E and F).

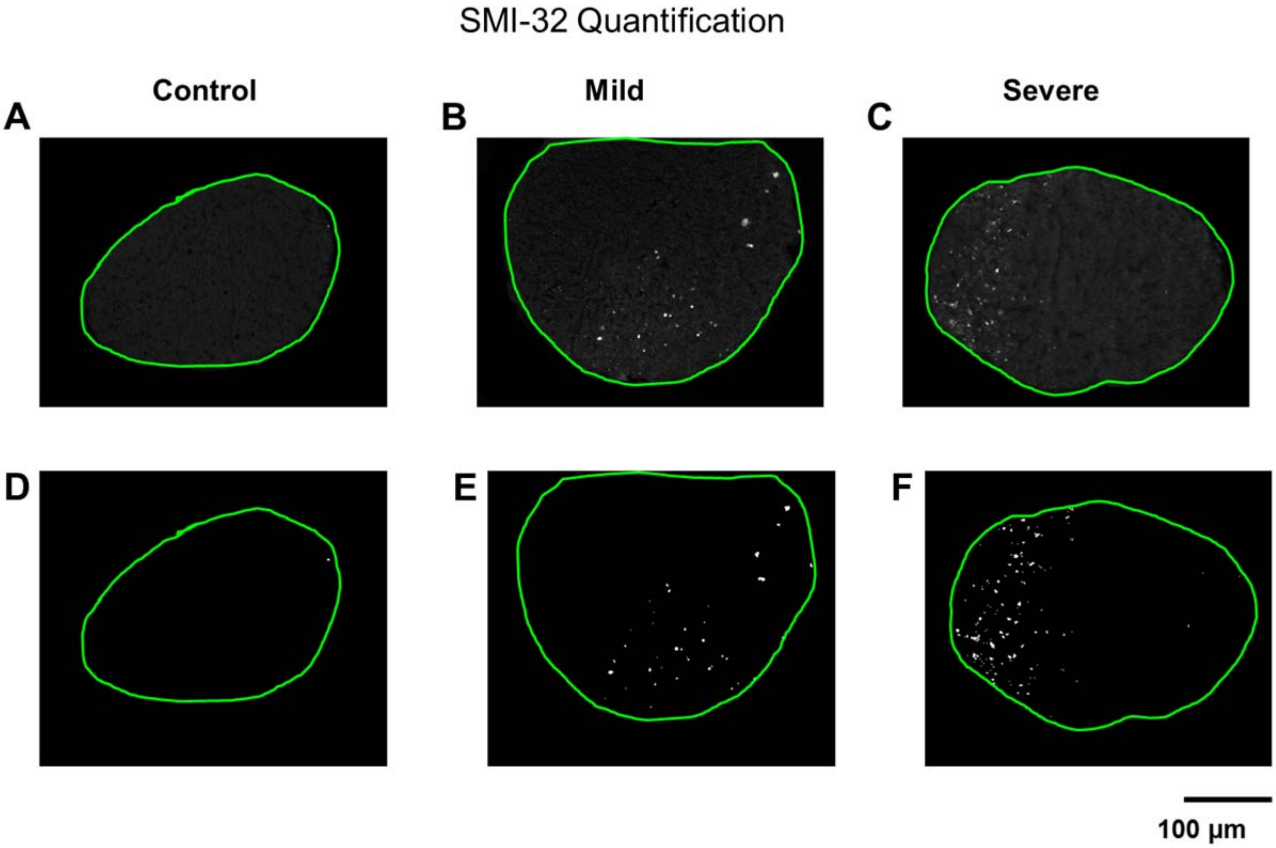

Figure 2–8 Panel A, B, and C are the representative 20x SMI-32 raw images of mice optic nerves with non-injured, mild injury, and severe injury, respectively. The green line in each panel is the border of optic nerves. After background signal suppression, the SMI-32 subtracted maps are shown in panel D, E, and F. The quantified numbers of mice optic nerves within the green lines with the three injury degree are 1, 96, and 226, respectively.

2.5 Quantification of MBP

Myelin integrity was examined using myelin basic protein (MBP) IHC. Myelin wraps around axons tightly. Consequently, the MBP positive stain has a small donut-ring shape in the plane orthogonal to the long axis of the optic nerve, Fig. 2 – 9, and requires higher magnification than DAPI or SMI-32. All histology maps including IHC maps would have significant amounts of background signal intensity especially in high magnification, which could be interpreted as false positives in intensity-based quantification analyses. Thus similar to SMI-32 stained images, background signal was subtracted using the protocol described in Section 2.4. However, the background signal subtraction on MBP stained micrographs still exhibit a noisy background, Fig. 2 – 9 E and F. In addition, the digitally captured histology maps would produce targets having blurred edges even though high magnification would be used. The blurred edge would prevent accurate target counting. Thus, the edge should be enhanced for accurate quantitative analysis. Herein, we employed a bilateral filter, or so called conditional mean filter, which is based on a Gaussian distribution, to preserve edges with noise reduced smoothing [34-36]. After background signal subtraction on 16-bit gray scale, images were converted into 8-bit gray scale. For noise reduction, a low-spatial-frequency = pass filter was employed with a pass-band determined by the spatial radius of the object under investigation. Again, the appropriate spatial radius would vary depending on magnification and target object dimensions. To enhance edges, signal-intensity-range-based-filtering was applied. In this study, mean intensity of the whole captured digital IHC image with background signal subtraction was used. Note that bilateral filtering must be performed on 8-bit gray scale image after background signal subtraction on 16-bit gray scale image. The effect of bilateral filtering for suppression of background noise on MBP stain is well shown in Fig. 2 – 9 H and I. Once the bilateral filtering was done, the IsoData threshold was performed on MBP stain, Fig. 2 – 10. However, unlike DAPI and SMI-32, the IsoData threshold missed many MBP positive regions, Fig. 2 – 10 D and F. So, an alternative threshold method was needed. To determine an appropriate threshold for MBP positive objects, the intensity histogram of the MBP stained image with background signal subtraction, image conversion, and bilateral filtering was examined Fig. 2 – 11 B. The histogram then was analyzed using a mono-exponential decay and exponential time constant, or exponential time constant of intensity, was obtained and employed as threshold to determine MBP positive object. This approach detected MBP positive regions accurately, which the IsoData threshold missed, Fig. 2 – 11 C and D. Using this optimized protocol, the EAE mice optic nerve having inflammation induced myelin damage could be quantitatively analyzed, Fig. 2 – 12.

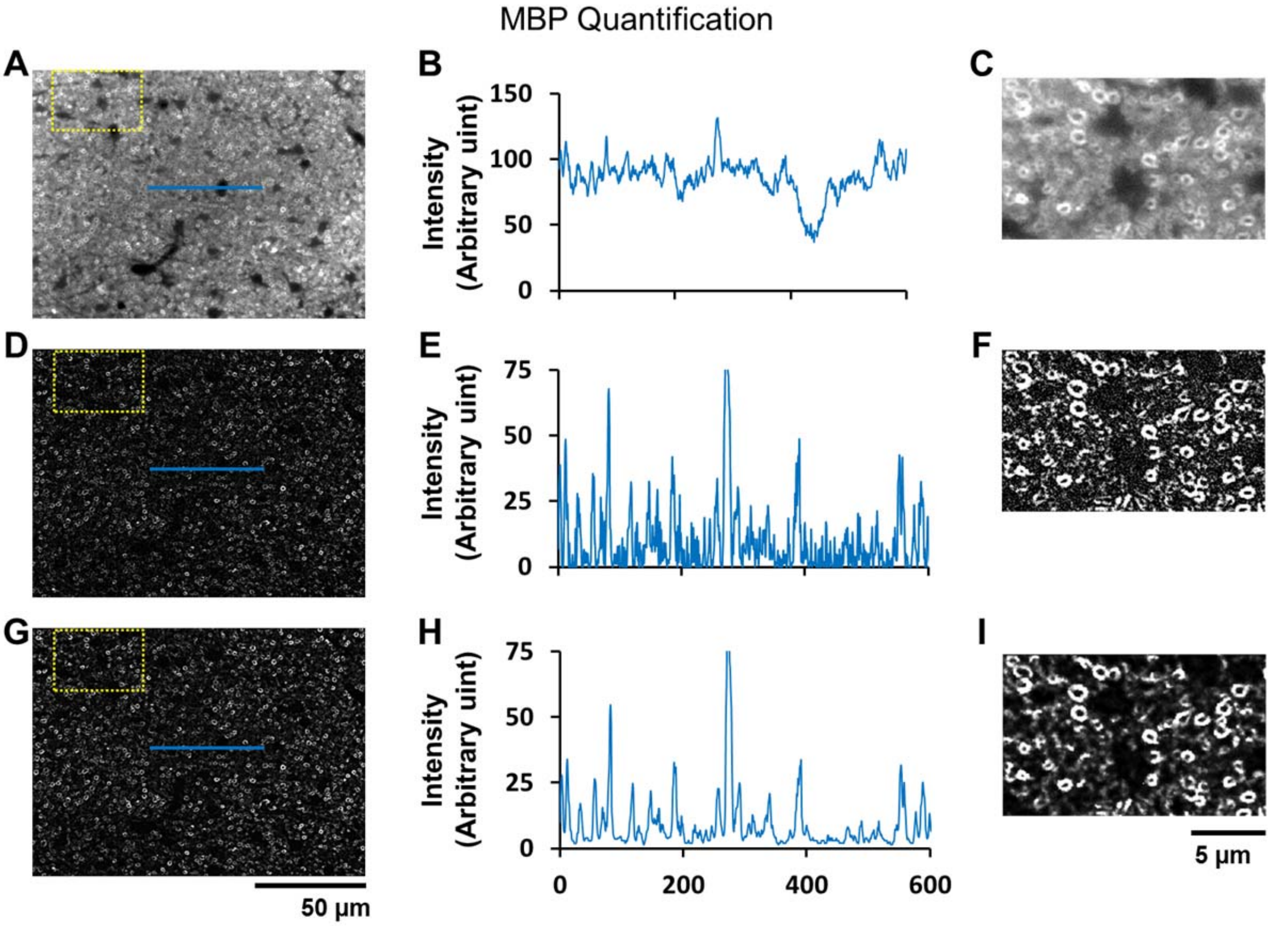

Figure 2–9 Myelin basic protein (MBP) stained mouse optic nerve. The MBP stain on optic nerve is shown at 60x magnification (panel A, D, and G). The panel C, F, and I are insets of panel A, D, and G, respectively. The panel A and C are raw images. The panel D and F are image with background subtraction (rolling ball algorithm). The panel G and I are images with background subtraction and noise reduction by means of the rolling ball algorithm and bilateral filter, respectively. The panel B, E, and H are one dimensional intensity profile of the region indicated as straight line in panel A, D, and G, respectively. The positions of the one-dimensional profiles are the same for all images. The raw MBP stain image shows non trivial background signal (panel A – C). The background signal is suppressed effectively using the same method as in Fig. 2-6 (panel D – F), yet leaves noise. The noise is reduced significantly via bilateral filtering (panel G – I).

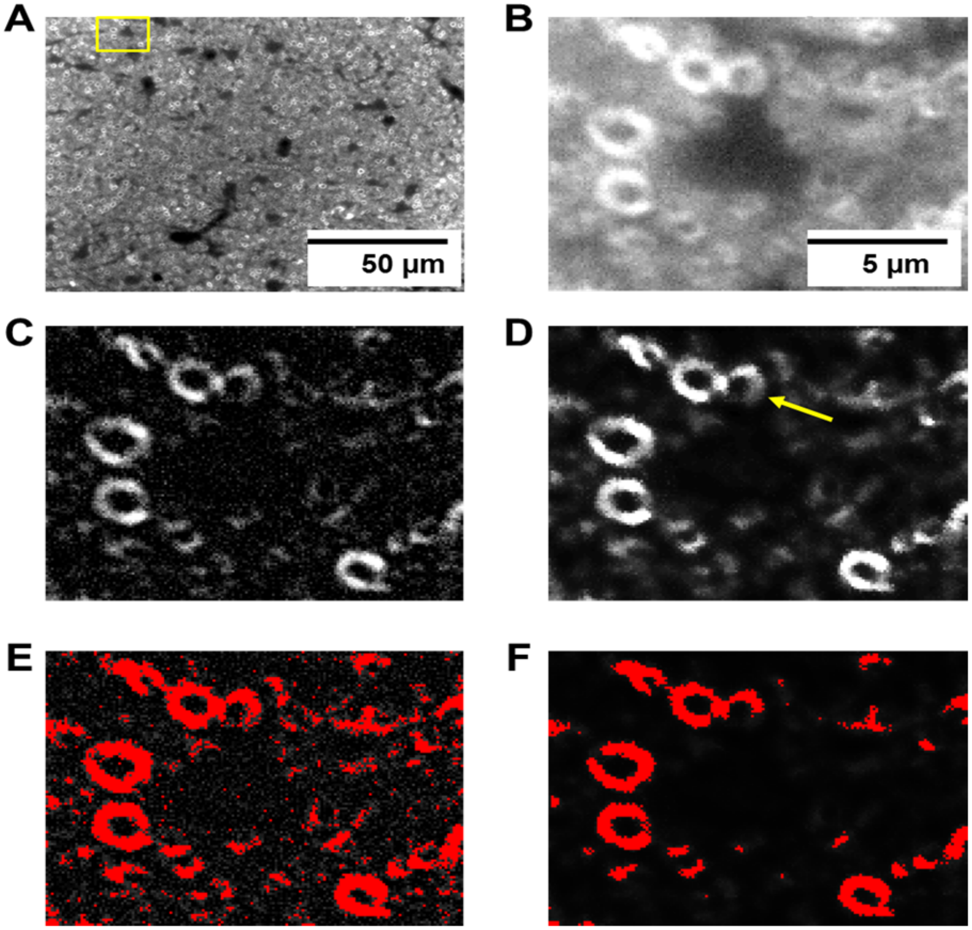

Figure 2–10 Quantification of MBP using an iterative-selection threshold. The panel B – F are insets of the panel A. The panel A and B are raw MBP-stained images. Panel C and E are images with background subtraction (rolling ball algorithm). Panel D and F show the effects of both background subtraction (rolling ball algorithm) and noise reduction using bilateral filtering. The MBP positive objects are determined using iterative selection threshold (IsoData) methods, similar to those used for DAPI and SMI-32 quantification (panel E and F). With background subtraction only, the noise is determined by MBP-positive objects, panel E. The noise-induced overestimation of MBP positive objects is not seen after bilateral filtering, panel F. However there are multiple MBP-positive objects missed with iterative selection threshold, indicated by arrow in D.

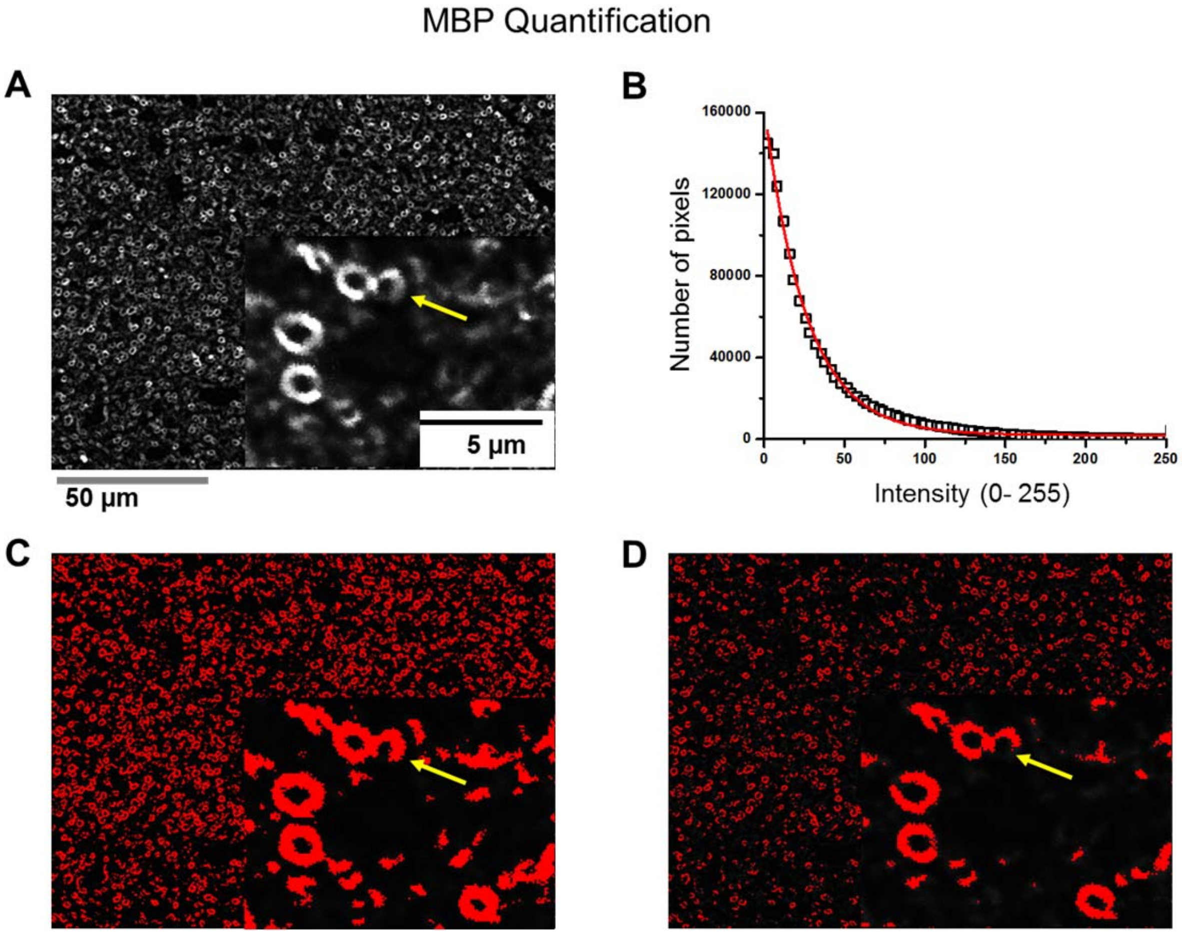

Figure 2–11 Determination of MBP positive objects using intensity-histogram thresholding. Panel A shows MBP staining with background subtraction and noise reduction. The intensity histogram (Panel B) of the resulting image in panel A shows a clear mono-exponential decay. The mono-exponential analysis of the intensity histogram produces an exponential time constant of intensity which is used as threshold (C). Panel C shows MBP-positive objects determined using exponential time constant of intensity as a threshold value, whereas panel D indicates MBP-positive objects based on an iterative-selection threshold (IsoData). The yellow arrow in Panel C indicates the location of a MBP-positive object detected using the mono-exponential analysis that is missed when the iterative-selection threshold is used.

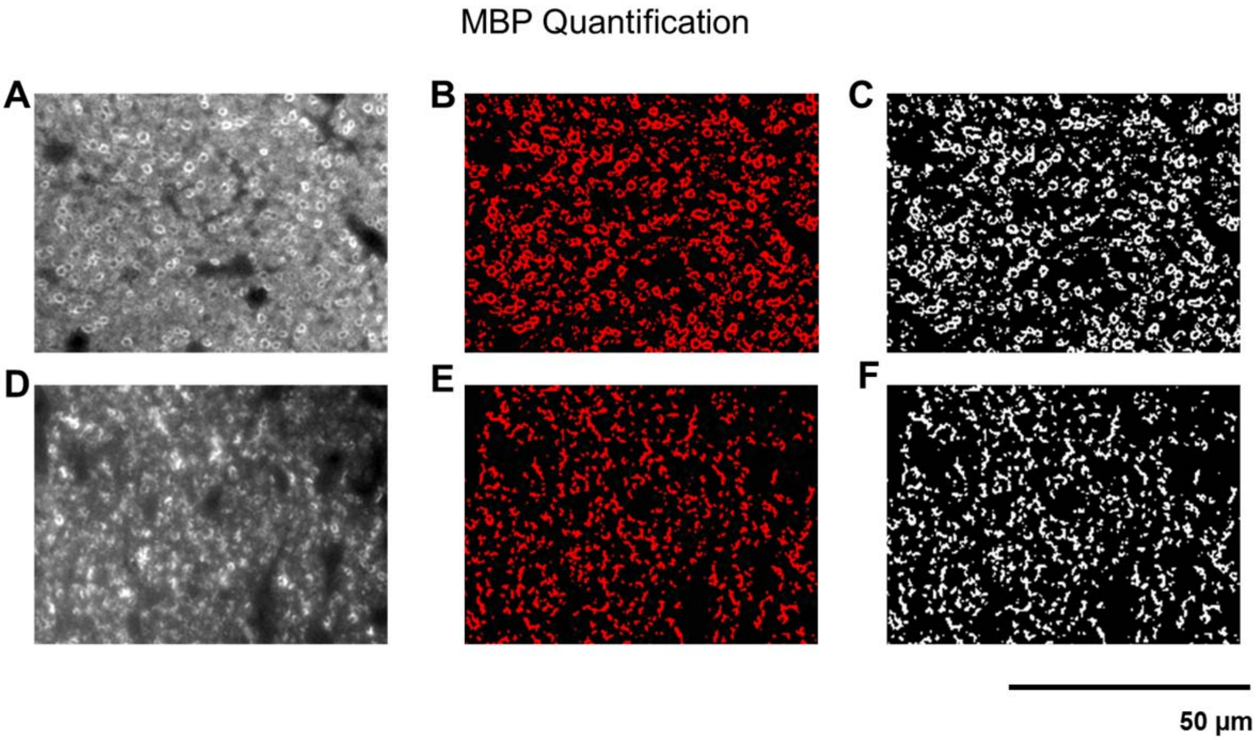

Figure 2–12 Representative 60x MBP stain of mice optic nerves and quantified maps. MBP-positive myelin is shown for control (A – C) and injury (D – F) mouse optic nerves. The panel A and D are raw images viewed at 60x. Panel B and E show the same images after applying the threshold. Panel C and F are final binary maps of MBP-positive objects. The 60x magnification has total 0.017 mm^2 field of view. In the control image, myelin area was determined to account for 0.0095 mm^2 (C, 56% of total image area), whereas it is reduced to 0.0075 mm^2 (F, 44% of total image area) in the control specimen.

2.6 Quantification of SMI-31

The total number of healthy axons determines the functional status of white-matter pathways. In this study, the numbers of healthy axons was measured using the phosphorylated neurofilament positive IHC stain, SMI-31. The axially sectioned axon would have small dot shape and be separated from neighboring axons due to the presence of myelin sheath. However, since IHC is based on fluorescence, two or more IHC positive targets can appear merged as one big bundle, which may falsely reduce quantified counts. Thus, accurate and objective segmentation should be done prior to quantification analysis for SMI-31. As one may see, SMI-31 quantification requires all image-processing protocols addressed above and more. First, the digitally captured SMI-31 gray scale 16-bit image underwent background signal subtraction, image conversion from 16 to 8-bit gray scale, and bilateral filtering. And, yet the IsoData threshold still couldn't detect all SMI-31 positive axons, Fig. 2 –13. The exponential time constant of intensity produced by intensity histogram analysis using exponential decay also failed to accurately detect SMI-31 positive axons. This was mainly due to the vague border between neighboring axons. To enhance the border between neighboring axons, a watershed method was employed. The watershed segmentation is based on local maximum [37-40]. Briefly, two local maximum intensity pixels would be selected and then the pixel having lowest intensity between two local maximum pixels would be selected as border. This process was repeated until all border points were connected. The Fig. 2 – 14 shows the connected border points successfully separating neighboring axons. However, this might produce false positive axons (e.g., indicated with arrow in Fig. 2 – 14 b). False positive axons can be removed using exponential analysis of the intensity histogram. Once image went through watershed segmentation, the segmenting line was assigned zero intensity. Then the whole image intensity was analyzed using exponential analysis producing an exponential time constant of intensity. The obtained exponential time constant of intensity value was employed to determine thresholding for SMI-31 positive axons, Fig. 2 -15. This approach showed potential to enumerate axons accurately and also remove false positive void areas, Fig. 2 –15 C and D. With these image-processing steps, SMI-31 counts in specimens from mice having severe axonal loss could be quantitatively analyzed, Fig. 2 – 16.

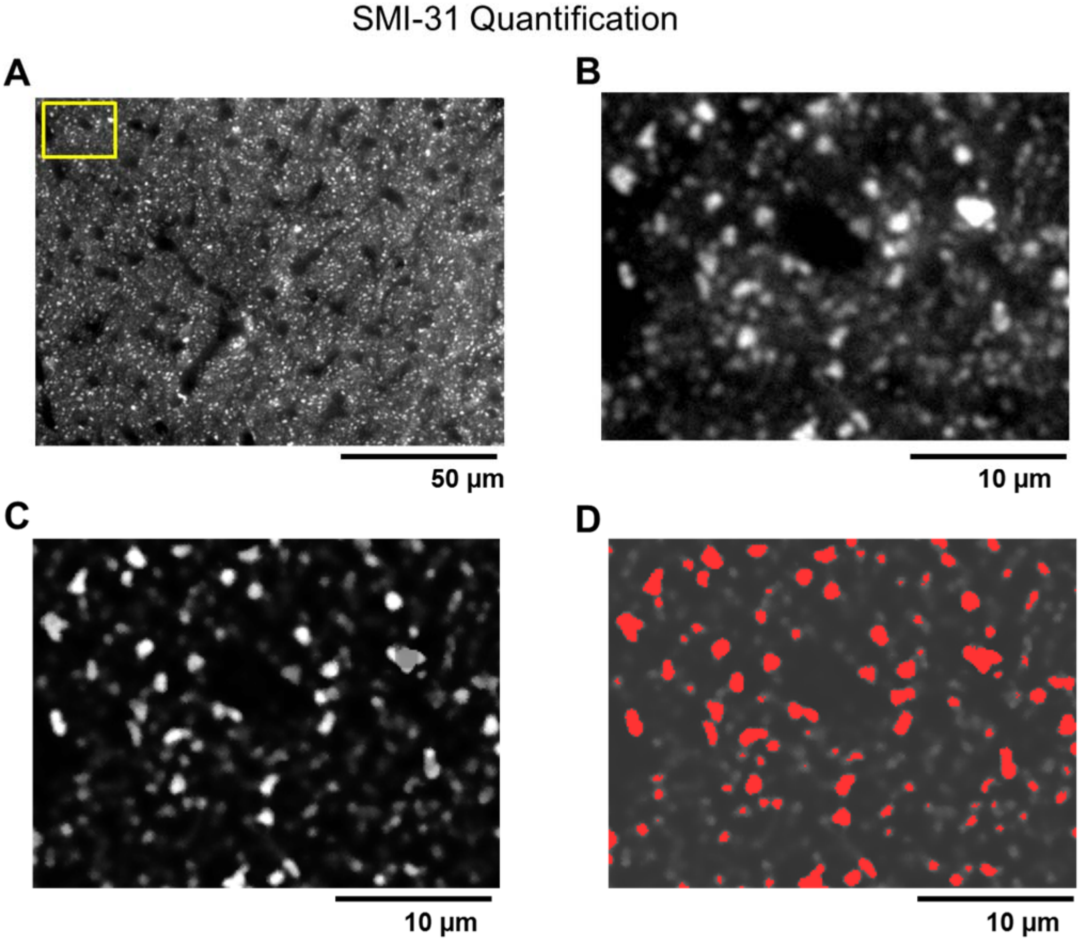

Figure 2–13 Phosphorylated neurofilament (SMI-31) staining of mouse optic nerve and one dimensional intensity profile. SMI-31 stain on mouse optic nerve is shown in 60x magnification (A). Panel B – D are of an inset from A. Panel A and B are raw images. Panel C has background subtraction (see Fig. 2 – 6) and noise reduction (see Fig. 2 – 9). Panel D is the result of iterative selection threshold (IsoData). The brightness of d is increased to show axons that are both selected and non-selected axons with this threshold. There are many SMI-31 positive objects missed with the iterative-selection threshold (IsoData) (D).

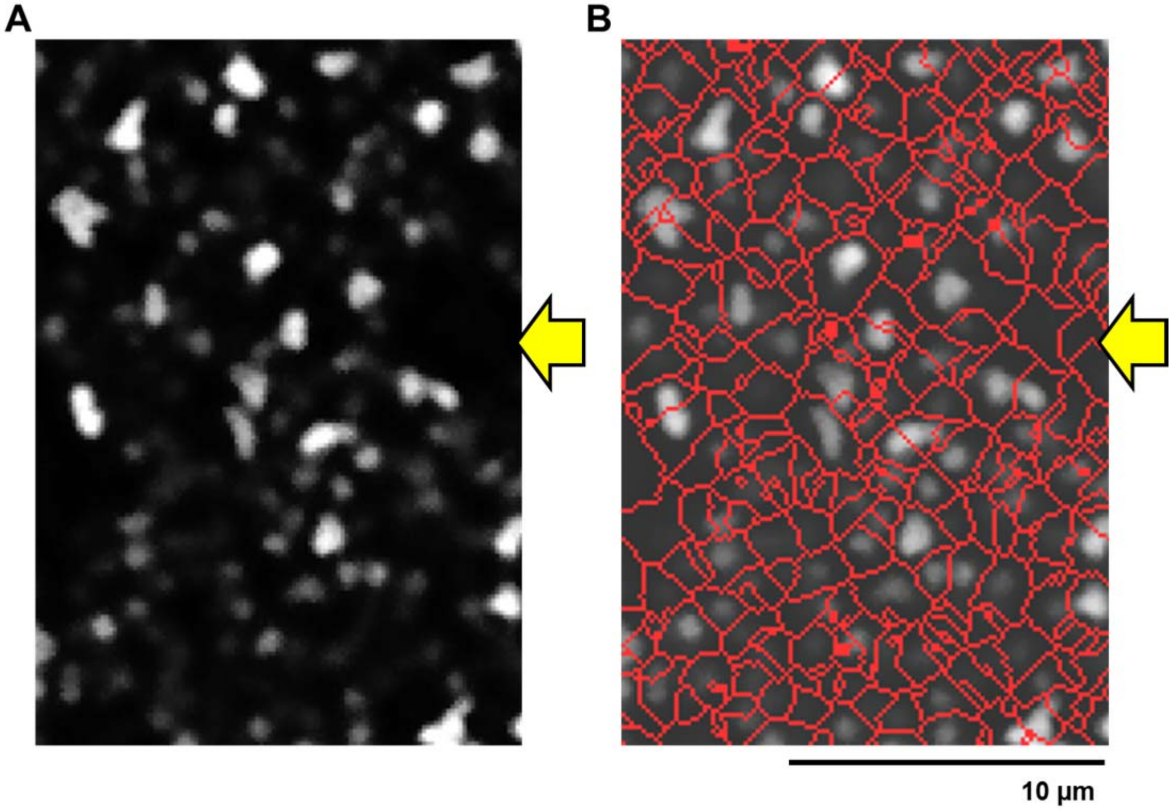

Figure 2–14 Watershed segmentation. A SMI-31-stained micrograph with background subtraction and noise reduction is shown in Panel A. Panel B has watershed segmentation lines separating adjacent SMI-31 positive objects. The brightness of panel B is enhanced to show both SMI-31 positive objects and the segmentation lines. The watershed segments adjacent SMI-31 positive axons precisely yet there are segmentation lines in void area indicated by the arrow.

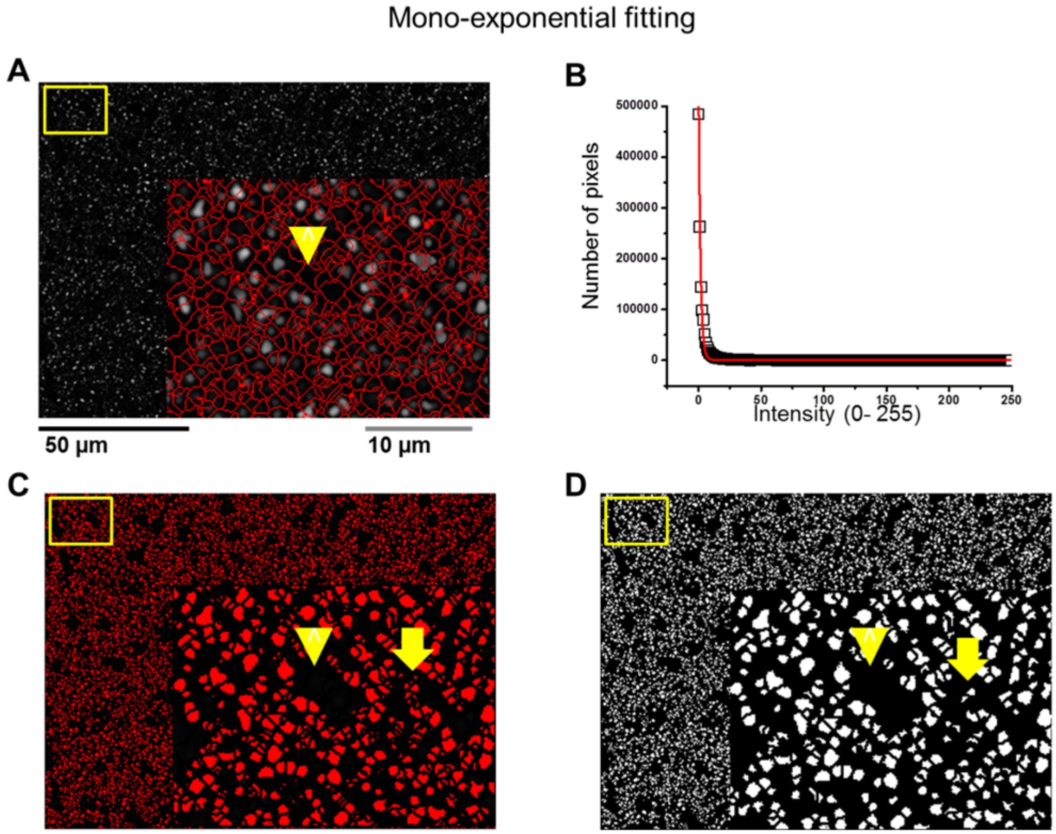

Figure 2–15 Determination of threshold from a watershed map for quantification of SMI-31 positive axons. Panel A shows an SMI-31-positive image with background subtraction, noise reduction, and watershed segmentation. The red segmentation lines are assigned zero intensity. The intensity histogram of watershed segmentation map is shown in panel B. A mono-exponential intensity decay is observed. Thus, exponential time constant of intensity is obtained from mono-exponential analysis. The observed exponential time constant of intensity is used as a threshold to determine SMI-31 positive objects (panel C). This threshold method detects SMI-31 positive objects precisely removing false positive void region indicated by the yellow arrow. However, exponential time constant of intensity threshold produces very small objects as SMI-31 positive objects. These small false positive objects are removed by selecting reasonable particle sizes in particle analysis (panel D).

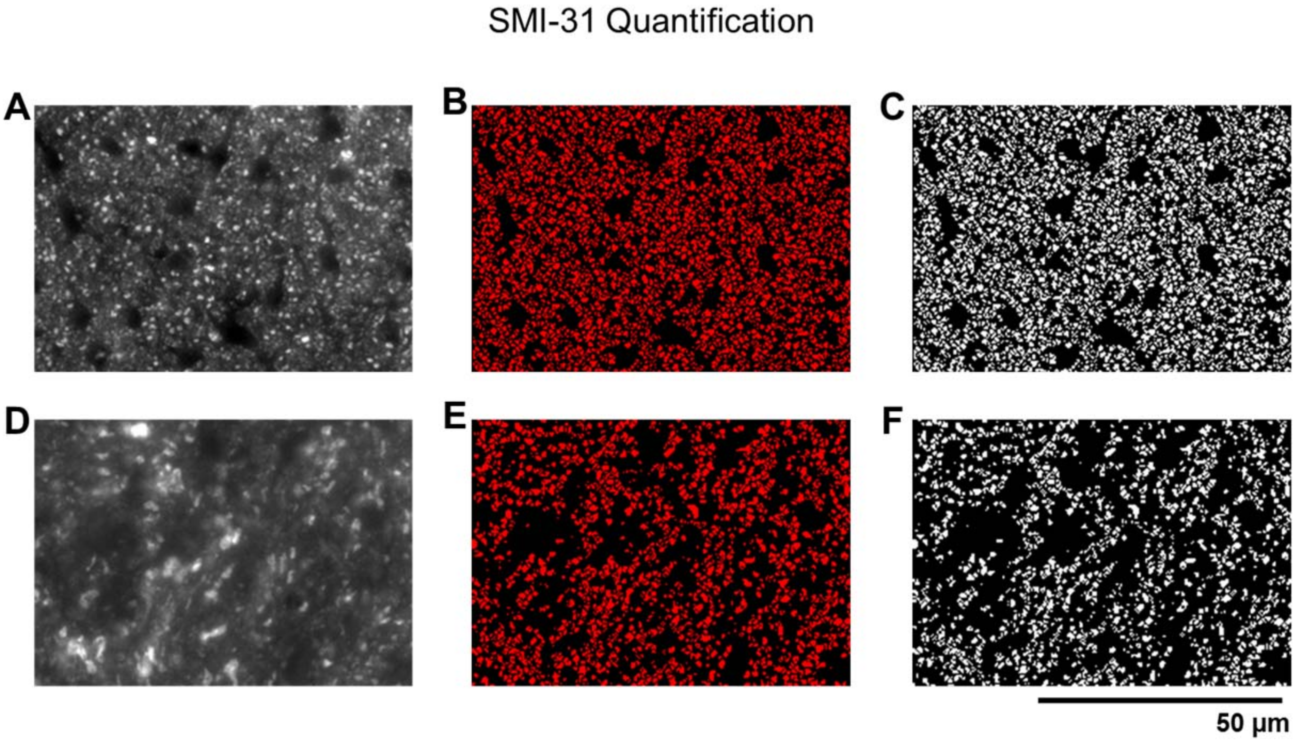

Figure 2–16 Representative SMI-31 staining of mice optic nerves and quantified maps. Phosphorylated neurofilament positive stain (SMI-31) of mouse optic nerves are shown for control (panel A – C) and EAE specimens (panel D – F). Panel A and D are raw SMI-31 stain images. Panel B and E are maps with threshold (see Fig. 2 – 15). Panel C and F are final binary maps for SMI-31 positive axons wherein control counts were $6.1 \times 10^5/\text{mm}^2$ and injury has $5.1 \times 10^5/\text{mm}^2$.

2.7 Conclusion

In conclusion, an objective quantification of IHC staining can be achieved using the aforementioned protocols. These protocols are highly reproducible and showed excellent sensitivity to the specified IHC labeled cells. Therefore, the establishment of IHC quantification protocols employed in our study provide for detailed and precise histologic validation of the in vivo diffusion MR findings.

2.8 Reference

1. Moseley, M., *Diffusion tensor imaging and aging - a review.* NMR Biomed, 2002. **15**(7-8): p. 553-60.

2. Neil, J., et al., *Diffusion tensor imaging of normal and injured developing human brain - a technical review.* NMR Biomed, 2002. **15**(7-8): p. 543-52.

3. Basser, P.J. and D.K. Jones, *Diffusion-tensor MRI: theory, experimental design and data analysis - a technical review.* NMR Biomed, 2002. **15**(7-8): p. 456-67.

4. Le Bihan, D., *Molecular diffusion, tissue microdynamics and microstructure.* NMR Biomed, 1995. **8**(7-8): p. 375-86.

5. Tournier, J.D., S. Mori, and A. Leemans, *Diffusion tensor imaging and beyond.* Magn Reson Med, 2011. **65**(6): p. 1532-56.

6. Armitage, P.A. and M.E. Bastin, *Selecting an appropriate anisotropy index for displaying diffusion tensor imaging data with improved contrast and sensitivity.* Magn Reson Med, 2000. **44**(1): p. 117-21.

7. Horsfield, M.A. and D.K. Jones, *Applications of diffusion-weighted and diffusion tensor MRI to white matter diseases - a review.* NMR Biomed, 2002. **15**(7-8): p. 570-7.

8. Sotak, C.H., *The role of diffusion tensor imaging in the evaluation of ischemic brain injury - a review.* NMR Biomed, 2002. **15**(7-8): p. 561-9.

9. Prosperini, L., et al., *Multiple Sclerosis: White and Gray Matter Damage Associated with Balance Deficit Detected at Static Posturography.* Radiology, 2013.

10. Rueda Lopes, F.C., et al., *The role of demyelination in neuromyelitis optica damage: diffusion-tensor MR imaging study.* Radiology, 2012. **263**(1): p. 235-42.

11. Agosta, F., et al., *Primary progressive multiple sclerosis: tactile-associated functional MR activity in the cervical spinal cord.* Radiology, 2009. **253**(1): p. 209-15.

12. Garaci, F.G., et al., *Optic nerve and optic radiation neurodegeneration in patients with glaucoma: in vivo analysis with 3-T diffusion-tensor MR imaging.* Radiology, 2009. **252**(2): p. 496-501.

13. Yu, C.S., et al., *Relapsing neuromyelitis optica and relapsing-remitting multiple sclerosis: differentiation at diffusion-tensor MR imaging of corpus callosum.* Radiology, 2007. **244**(1): p. 249-56.

14. Wang, Y., et al., *Quantification of increased cellularity during inflammatory demyelination.* Brain, 2011. **134**(Pt 12): p. 3590-601.

15. Tu, T.W., et al., *Diffusion Basis Spectrum Imageing detects evolving axonal injury, demyelination, and inflammation in the course of EAE.* Proc. Intl. Soc. Mag. Reson. Med. 20, 3598, 2011.

16. DeBoy, C.A., et al., *High resolution diffusion tensor imaging of axonal damage in focal inflammatory and demyelinating lesions in rat spinal cord.* Brain, 2007. **130**(Pt 8): p. 2199-210.

17. Kozlowski, P., et al., *Characterizing white matter damage in rat spinal cord with quantitative MRI and histology.* J Neurotrauma, 2008. **25**(6): p. 653-76.

18. Song, S.K., et al., *Dysmyelination revealed through MRI as increased radial (but unchanged axial) diffusion of water.* Neuroimage, 2002. **17**(3): p. 1429-1436.

19. Song, S.K., et al., *Diffusion tensor imaging detects and differentiates axon and myelin degeneration in mouse optic nerve after retinal ischemia.* NeuroImage, 2003. **20**(3): p. 1714-22.

20. Mac Donald, C.L., et al., *Diffusion tensor imaging reliably detects experimental traumatic axonal injury and indicates approximate time of injury.* J Neurosci, 2007. **27**(44): p. 11869-76.

21. Mac Donald, C.L., et al., *Detection of traumatic axonal injury with diffusion tensor imaging in a mouse model of traumatic brain injury.* Exp Neurol, 2007. **205**(1): p. 116-31.

22. Idikio, H.A., *Immunohistochemistry in diagnostic surgical pathology: contributions of protein life-cycle, use of evidence-based methods and data normalization on interpretation of immunohistochemical stains.* International Journal of Clinical and Experimental Pathology, 2010. **3**(2): p. 169-176.

23. Ramos-Vara, J.A., *Technical aspects of immunohistochemistry.* Veterinary Pathology, 2005. **42**(4): p. 405-426.

24. Kubista, M., B. Akerman, and B. Norden, *Characterization of Interaction between DNA and 4',6-Diamidino-2-Phenylindole by Optical Spectroscopy.* Biochemistry, 1987. **26**(14): p. 4545-4553.

25. Zink, D., N. Sadoni, and E. Stelzer, *Visualizing chromatin and chromosomes in living cells.* Methods, 2003. **29**(1): p. 42-50.

26. Budde, M.D., et al., *Axonal injury detected by in vivo diffusion tensor imaging correlates with neurological disability in a mouse model of multiple sclerosis.* NMR Biomed, 2008. **21**(6): p. 589-97.

27. Budde, M.D., et al., *Toward accurate diagnosis of white matter pathology using diffusion tensor imaging.* Magn Reson Med, 2007. **57**(4): p. 688-95.

28. Budde, M.D., et al., *Axial diffusivity is the primary correlate of axonal injury in the experimental autoimmune encephalomyelitis spinal cord: a quantitative pixelwise analysis.* J Neurosci, 2009. **29**(9): p. 2805-13.

29. Kim, J.H., et al., *Detecting axon damage in spinal cord from a mouse model of multiple sclerosis.* Neurobiol Dis, 2006. **21**(3): p. 626-32.

30. Ridler, T.W. and S. Calvard, *Picture thresholding using an iterative selection method.* IEEE Transactions on Image Processing Systems, Man and Cybernetics, 1978. **8**: p. 630-632.

31. Miller, C.C., et al., *Axonal transport of neurofilaments in normal and disease states.* Cell Mol Life Sci, 2002. **59**(2): p. 323-30.

32. Sternberg, S.R., *Biomedical Image-Processing.* Computer, 1983. **16**(1): p. 22-34.

33. Woo, J., et al., *Geometric feature-based multimodal image registration of contrast-enhanced cardiac CT with gated myocardial perfusion SPECT.* Med Phys, 2009. **36**(12): p. 5467-79.

34. Chin, R.T. and C.L. Yeh, *Quantitative-Evaluation of Some Edge-Preserving Noise-Smoothing Techniques.* Computer Vision Graphics and Image Processing, 1983. **23**(1): p. 67-91.

35. Himayat, N. and S.A. Kassam, *Approximate Performance Analysis of Edge-Preserving Filters.* Ieee Transactions on Signal Processing, 1993. **41**(9): p. 2764-2777.

36. Denis, L., et al., *Joint filtering of SAR amplitude and interferometric phase with graph-cuts.* Traitement Du Signal, 2009. **26**(2): p. 127-144.

37. Haris, K., et al., *Hybrid image segmentation using watersheds and fast region merging.* Ieee Transactions on Image Processing, 1998. **7**(12): p. 1684-1699.

38. Li, F., F. Seillier-Moiseiwitsch, and V.R. Korostysheyskiy, *Region-based statistical analysis of 2D PAGE images.* Computational Statistics & Data Analysis, 2011. **55**(11): p. 3059-3072.

39. Luo, X.Y., J. Zhang, and Q.H. Dai, *A regional image fusion based on similarity characteristics.* Signal Processing, 2012. **92**(5): p. 1268-1280.

40. Omer, O.A. and T. Tanaka, *Region-based weighted-norm with adaptive regularization for resolution enhancement.* Digital Signal Processing, 2011. **21**(4): p. 508-516.

Chapter 3

Quantifying white matter tract diffusion parameters in the presence of increased extra-fiber cellularity and vasogenic edema

This chapter represents a manuscript initially submitted on June 26th, 2013 to NeuroImage and currently under review. (Chia-Wen Chiang, Yong Wang, Peng Sun, Tsen-Hsuan Lin, Kathryn Trinkaus, Anne H. Cross, and Sheng-Kwei Song)

Abstract

The effect of extra-fiber structural and pathological components confounding diffusion tensor imaging (DTI) computation was quantitatively investigated using data generated by both Monte-Carlo simulations and realistic tissue phantoms. Increased extent of vasogenic edema, by addition of various amount of gel to fixed normal trigeminal nerves or by increasing non-restricted isotropic diffusion tensor component in Monte-Carlo simulations, significantly decreased fractional anisotropy (FA), increased radial diffusivity, while less significantly increased axial diffusivity derived by DTI. Increased cellularity, mimicked by graded increase of restricted isotropic diffusion tensor component in Monte-Carlo simulations, significantly decreased FA and axial diffusivity with limited impact of radial diffusivity derived by DTI. The recently developed novel diffusion basis spectrum imaging (DBSI) was also applied to detect and quantify the increased cellularity and vsaogenic edema. Results showed that increased cellularity or vasogenic edema did not change the DBSI derived fiber FA, axial or radial diffusivity. The extent of extra-fiber cellularity and edema estimated by DBSI correlated with experimentally added gel and true values of Monte-Carlo simulations. We also examined the

feasibility of applying 25-direction diffusion encoding scheme for DBSI analysis on coherent white matter tracts. Results suggested that the 25-direction diffusion scheme provided accurate DBSI estimation of both fiber diffusion parameters and extra-fiber cellularity/edema extent. An *in vivo* 25-direction DBSI analysis was performed on experimental autoimmune encephalomyelitis (EAE, an animal model of human multiple sclerosis) optic nerve as an example to demonstrate the validity of derived DBSI parameters with post-imaging immunohistochemistry verification.

3.1 Introduction

Diffusion tensor imaging (DTI) successfully detects axon and myelin injury through decreased axial diffusivity ($\lambda_{\|}$, parallel to white matter tract) and increased radial diffusivity ($\lambda_{\perp}$, perpendicular to white matter tract) in animal models of central nervous system (CNS) diseases and injuries [1-4]. Although decreased fractional anisotropic (FA) has been demonstrated to reflect myelin damage in multiple sclerosis (MS) [5], it is not a marker specific to myelin damage since other pathological components may also contribute to diffusion anisotropy change [6, 7]. For example, inflammation associated vasogenic edema has been recognized to increase apparent diffusion coefficient underestimating the diffusion anisotropy of fiber tracts [8, 9]. Increased cellularity has been demonstrated to decrease apparent diffusion coefficient [10]. However, its impact on diffusion anisotropy remains unclear. An *in vivo* experiment of white matter inflammation in rats has suggested the association of DTI derived apparent diffusion coefficients (ADC) with the evolution of pathology [11]. It is without a doubt that various pathological components impact DTI derived metrics.

DTI assumes that diffusion of water molecules in the CNS white matter follows mono-exponential diffusion signal decay (typically at b-value < 1000 s/mm^2) as a single anisotropic tensor. Thus, diffusion anisotropy of white matter tracts in the presence of multiple structural and pathological compartments poses significant challenges in DTI analysis of white matter tracts since non-Gaussian models or multiple diffusion tensors are needed to correctly reflect the tissue and pathological complexity. Various diffusion techniques have been proposed to overcome the limitation of DTI by non-Gaussian modeling of both parametric (model-based) or non-parametric (model-free) approaches. For instance, diffusion spectrum imaging (DSI) resolves crossing or branching fibers by direct evaluation of diffusion displacement probability density function which is the inverse Fourier transform of the diffusion weighted signals, but typically requires a large number of measurements [12]; diffusion kurtosis imaging (DKI) quantifies the non-Gaussian diffusion by estimating apparent diffusion kurtosis of diffusion displacement probability distribution [13]; generalized diffusion tensor imaging (gDTI) models the white matter tract via higher order tensors [14]; composite hindered and restricted model of diffusion - (CHARMED) evaluates an extra-cellular compartment (assigned to hindered diffusion resulting from extra-axonal diffusion weighted signal) and intra-cellular compartments (assigned to restricted diffusion in a cylinder with zero radius representing individual intra-axonal space) employing a comprehensive diffusion weighting scheme [15]. Recently, Scherrer et al. proposed multiple fascicle models (MFM) to model an isotropic compartment (assigned to free water diffusion) and multiple anisotropic compartments (assigned to single fascicle) using a cube and sphere (CUSP) acquisition scheme [16]. Zhang et al. proposed neurite orientation dispersion and density imaging (NODDI) to model tissue components. Using high-angular-resolution diffusion imaging (HARDI) acquisition scheme, NODDI assesses intra-cellular (assigned to space within neurites), extra-cellular (assigned to space around the neurites but occupied by glial cells), and CSF compartments for deriving neurite density and orientation dispersion [17]. Although these approaches resolve possible fiber orientations and free water diffusion contaminations confounding DTI in the CNS, the restricted water diffusion outside fiber tracts affecting DTI measurements has not been dealt with.

The recently-developed diffusion basis spectrum imaging (DBSI) approach models white matter diffusion as the linear combination of multiple discrete anisotropic diffusion tensors describing axonal tracts and a spectrum of isotropic diffusion tensors describing restricted (reflecting cells), non-restricted (reflecting extra-axonal and extracellular space) diffusion components outside of axonal tracts [18]. Employing a 99-direction diffusion-encoding scheme, DBSI has shown promise to accurately detect and quantify crossing fibers, axonal injury, demyelination, and inflammation-associated cell infiltration and edema in both *ex vivo* phantom and *in vivo* mouse brain. Although the effect of increased cell infiltration and edema on DTI-derived indices has been demonstrated preliminarily using cuprizone treated mouse model and mouse trigeminal nerve phantoms (Wang, 2011), a more comprehensive study was needed to investigate the effect of increased cellularity and vasogenic edema associated with inflammation. In this study, diffusion weighted signals derived from Monte-Carlo simulations and experimentally acquired from realistic tissue phantoms of fixed mouse trigeminal nerve and 2% agar gel were employed to demonstrate how various inflammatory components change DTI indices. The accuracy of DBSI to resolve the complication of inflammation was also examined.

Although the original 99-direction diffusion encoding scheme is readily implemented in clinical scanners, it poses significant challenges in the animal scanners to obtain DBSI data from mouse CNS. To image the coherent white matter tracts without fiber crossing, such as optic nerve and spinal cord, a simplified DBSI with $N_{Aniso} = 1$ would be sufficient and require less diffusion encoding directions. A reduced scanning time can be achieved by significantly reducing the number of diffusion weighted images. Thus, we adopted a 25-direction diffusion encoding scheme [19] on both Monte-Carlo simulations and realistic tissue phantoms. Comparisons between 25- and 99-direction DBSI results on both simulated and experimental data were conducted to examine the accuracy of DBSI analysis using the 25-direction diffusion encoding scheme. To further demonstrate the feasibility of the 25-direction scheme for DBSI analysis, *in vivo* diffusion MRI was performed on an EAE-affected mouse at the onset of optic neuritis. The *in vivo* diffusion MRI data were analyzed using DBSI and verified by post-imaging immunohistochemistry.

3.2 Materials and Methods

3.2.1 Diffusion-encoding schemes

Both 99- [18] and 25-direction [19] diffusion-encoding schemes were employed for DBSI analysis in this study. The 99 diffusion-encoding directions were selected as prescribed in diffusion spectrum imaging (DSI) where the position vectors are the entire grid points (q_x, q_y, q_z) over the 3-D q-space under the relationship that $(q_x^2+q_y^2+q_z^2) \leq r^2$, where r = 3 for DBSI [20, 12, 18]. The icosahedral 25-direction sampling scheme was as prescribed by Batchelor et al. with the addition of one extra non-diffusion (b = 0) weighted image. See Appendix A and B for a detail of 99- and 25-direction diffusion-encoding schemes, respectively.

3.2.2 Fixed trigeminal nerve phantom

Trigeminal nerves from adult female normal C57BL/6 mice (The Jackson Laboratory, Bar Harbor, ME) were dissected after fixation and kept in 0.01 M phosphate buffered saline (PBS) solution. Twenty trigeminal nerves were employed to generate phantoms of a single trigeminal nerve only (n = 7) and a single nerve juxtaposed with different amount of 2% aqueous agar gel to mimic vasogenic edema (n = 13). All phantoms were prepared on a slide and covered with plastic wrap immediately before measurements to avoid dehydration. Diffusion-weighted data were collected utilizing a diffusion-weighted spin-echo spectroscopy sequence with 99- and 25-direction schemes at a single setting with the following acquisition parameters: TR 2 sec, TE

32 ms, Δ 16 ms, δ 8 ms, 1 average, and maximum b-value 3200 s/mm^2 for *ex vivo*. Total acquisition time was 4 min 15 sec.

3.2.3 Monte-Carlo simulation

Monte-Carlo simulations were performed to evaluate the effect of vasogenic edema and cellularity on DTI and DBSI indices in the aforementioned realistic tissue phantoms. The simulation was performed by allowing water molecules (2.5×10^5, randomly distributed) to undergo random walk within a 90-μm diameter sphere (light blue, Fig. 3 - 1 A) at 20 °C. Thus, diffusivity for free water was set to be 2.02 μm^2/ms. The time-step for simulated random walk was 0.2 ms. The computer simulation model of the trigeminal nerve phantom were composed with (1) a coherent axon fiber bundle modeled by uniformly oriented, and tightly packed cylindrical tubes (green cylinders in Fig. 3 – 1 A) with diameter of 2 μm; (2) cellular components modeled as isotropic spheres (blue in Fig. 3 – 1 A) with a diameter of 6 μm randomly placed surrounding the axonal fiber bundle; (3) extra-axonal and extracellular space occupied by water molecules distributed outside of axonal bundle and cellular components (Fig. 3 - 1 A). The size of axonal cylinder and cells was adapted according to literature reports [21, 22]. The imaging voxel ($50 \times 50 \times 50$ μm^3, pink cube in Fig 1A) was placed in the center of the sphere defined for random walk (light blue outer sphere in Fig. 3 - 1 A). At the boundary of axon and cell components, the water spin reflected elastically [14]. During the simulation, water spins were allowed to walk in or out of the imaging voxel without constrains to reflect the real physical condition [14]. The boundaries of the axon and cell components were assumed to be impermeable. The random walk trajectory of each water spin was recorded and saved during the simulation.

Based on previous mouse trigeminal nerve phantom study [18], baseline trigeminal nerve model (model # 1, Fig. 3 - 1 B), the simulation of nerve only phantom, consisted of 12% cells (133 spheres), 68% axonal fibers (529 cylinders), and 20% extra-axonal/extracellular space. The tissue phantom of single nerve plus gel was simulated by increasing the size of imaging voxel of baseline nerve model, thereby increasing the extra-axonal/extracellular space (model # 2-11, Fig. 3 - 1 B), to mimic vasogenic edema. For model # 2-11, the cellularity ranged from 7% to 15%, the axonal fiber fraction ranged from 15% to 57%, and the extra-axonal/extracellular space ranged from 27% to 78% (Fig. 3 – 1 B). Although it is very challenging to control the amount of cellularity in the experimental trigeminal nerve phantom, varied cellularity was readily simulated by simply increasing the number of spheres (cells) inside the imaging voxel. Models with different amount of cellularity content (model # 12-21) were generated by increasing number of spheres into the imaging voxel. For simulations of varied cellularity (model # 12-21), the cellularity ranged from 14% to 80%, the axon fiber fraction ranged from 12% to 63%, and the extra-axonal/extracellular space ranged from 8% to 22%.

A simple spin echo sequence with diffusion gradients was implemented to simulate the diffusion weighted MRI signals from the imaging voxel. The simulated phase of each water spin at the echo time (TE) was calculated based on the random walk trajectory [14]. The overall measured diffusion MRI signal was simulated as the summation of signals contributed from all water spins, ending within the voxel of imaging at the time of TE. The effect of T1 and T2 decay for all spin trajectories were neglected [14]. Both 99- and 25-direction schemes were employed to acquire the diffusion weighted signals. Other key MRI acquisitions parameters included TE 32 ms, Δ 16 ms, δ 8 ms, maximum b-value 3200 s/mm^2 were kept the same intentionally with the fixed trigeminal nerve phantom experiment above. Rician noise was added to simulated diffusion MRI signals to mimic the typical achievable signal-to-noise ratio (SNR) = 40 in our hands.

3.2.4 In vivo diffusion MRI of acute optic neuritis

A female 8-week-old C57BL/6 mouse (The Jackson Laboratory, Bar Harbor, ME, USA) was immunized using 50 µg myelin oligodendrocyte glycoprotein peptide ($MOG_{35\text{-}55}$) emulsified in incomplete Freund's adjuvant with 50 µg Mycobacterium tuberculosis. One age-matched sham female mouse received only incomplete Freund's adjuvant in the absence of $MOG_{35\text{-}55}$ and Mycobacterium tuberculosis. For EAE-immunized mouse, the adjuvant pertussis toxin (300 ng; PTX, List Laboratories, Campbell, CA) was injected intravenously on the day of immunization and two days later. Transverse view of mouse optic nerve was imaged when visual impairment was first detected at the onset of acute EAE optic neuritis [23].

In vivo diffusion MRI experiments were performed on a 4.7-T Agilent DirectDrive™ small-animal MRI system (Agilent Technologies, Santa Clara, CA) equipped with Magnex/Agilent HD imaging gradient coil (Magnex/Agilent, Oxford, UK) with pulse gradient strength up to 58 G/cm and a gradient rise time ≤ 295 µs. After anesthetizing using 1% isoflurane/oxygen, mice were placed in a custom-made head holder. The rate of respiration and rectal temperature, at 37 °C, was monitored and controlled by a small animal physiological monitoring and control unit (SAII Inc., NY). An actively-decoupled volume (transmit) /surface (receive) coil pair was used for MR excitation and signal reception. All image slices were acquired based on previously reported procedures [24]. A final-targeted slice showing a transverse view of mouse brain with two optic nerves, as nearly as orthogonal to image slice as possible, resulted (Fig. 3 – 2 A). A multi-echo spin-echo diffusion-weighted sequence [25] and a

25-direction diffusion-encoding scheme combined with one b = 0 were employed and MR acquisition parameters were TR 1.5 sec, TE 37 ms, Δ 18 ms, δ 6 ms, max. b-value 2200 s/mm^2, slice thickness 0.8 mm, in-plane resolution 117 μm × 117 μm (before zero-filled). The total acquisition was approximately 2 hour, 20 minutes.

3.2.5 Immunohistochemistry

Mice were perfusion fixed with 0.01 M phosphate-buffered saline (PBS) followed by 4% paraformaldehyde in 0.01 M PBS immediately after imaging. Brains were excised and fixed for 24 h, and then transferred to 0.01 M PBS for storage at 4 °C until histological analysis. Fixed optic nerves were embedded in 2% agar blocks [26] before being embedded in paraffin. Five-μm thick transverse slices were sectioned, deparaffinized, rehydrated, and blocked using a 1:1 mixture of 10% normal goat serum and 2% bovine serum albumin in PBS for 20 min at room temperature to prevent nonspecific binding of goat secondary antibody. Sections were incubated in monoclonal anti-phosphorylated neurofilament primary antibody (SMI-31; 1:1000, Covance, US) to stain non-injured axons, or in rabbit anti-myelin basic protein (MBP) primary antibody (1:1000, Sigma Inc., MO) to stain myelin sheath at 4 °C overnight. After several rinses, secondary goat anti-mouse IgG and goat anti-rabbit IgG conjugated Alexa 488 (1:800, Invitrogen) were applied respectively to visualize immunoreactivity of materials at room temperature for 1 h. After washing, slides were covered using Vectashield Mounting Medium with 4′,6-diamidino-2-phenylindole (DAPI) (Vector Laboratory, Inc., Burlingame, CA). Histological images were acquired at 20x and 60x (water objective) magnifications on Nikon Eclipse 80i fluorescence microscope using MetaMorph software (Universal Imaging Corporation, Sunnyvale, CA).

3.2.6 Data analysis

Experimental and simulated data using 99- and 25-direction diffusion encoding schemes were examined by DBSI multi-tensor model analysis package developed in-house with Matlab® (MathWorks) [18] and conventional DTI single-tensor model analysis. Briefly, Eq. [1] was first solved by fitting total number k diffusion signals using a linear combination of diffusion basis sets consisting of cylindrically symmetric diffusion tensors with the freedom to vary $\lambda_{\parallel}$ and $\lambda_{\perp}$ to estimate the number of anisotropic diffusion tensor components (N_{Aniso}) and the associated principal directions. After N_{Aniso} was computed, isotropic components were further analyzed using nonnegative least-squares (NNLS) technique. For coherent white matter tract in this study, $N_{Aniso} = 1$.The global nonlinear optimization was conducted employing direct pattern search to solve Eq. [1]. S_k is the k^{th} measured diffusion weighted signals ($k = 1, 2, \ldots, 99$ (or 25) in this study). f_i and $f(D)$ are signal intensity fractions of i^{th} anisotropic diffusion components and a spectrum of isotropic diffusion components from a to b (typically from 0 to 5) diffusivity, respectively.

$$S_k = \sum_{i=1}^{N_{Aniso}} f_i e^{-|\overrightarrow{b_k}|\lambda_{\perp i}}\, e^{-|\overrightarrow{b_k}|(\lambda_{\parallel i}-\lambda_{\perp i})\cos^2\psi_{ik}} + \int_a^b f(D)e^{-|\overrightarrow{b_k}|D}dD \quad (k = 1,2,3,\ldots) \qquad [1]$$

3.2.7 Statistical analysis

All data were expressed as mean ± standard deviation. The comparison between DTI and DBSI derived diffusion parameters was performed on data obtained from trigeminal nerve phantoms and from Monte-Carlo simulations using linear repeated measures regression models. Two one-sided t-tests (TOST) at a 0.05 significance level were performed to test equivalence of 99- and 25-direction DBSI derived $\lambda_{\parallel}$, $\lambda_{\perp}$, and FA, as well as the diffusion fractions of different components. The tests were repeated for data from models with a changing proportion of extra-axonal/extracellular space and for those with a changing proportion of cells. One test compared the mean difference to an upper equivalence boundary and the other to a lower equivalence boundary, defined as ± 2 × standard deviations. All statistical analyses were performed using SAS V9.3 (SAS Inc., Cary, NC).

3.3 Results

3.3.1 Effect of vasogenic edema on DTI derived parameters

In trigeminal nerve only phantoms, DTI derived $\lambda_{\|} = 0.77 \pm 0.05$ $\mu m^2/ms$, $\lambda_{\perp} = 0.18 \pm 0.02$ $\mu m^2/ms$, and FA = 0.72 ± 0.04 were compared with those derived using DBSI where $\lambda_{\|} = 1.09 \pm 0.06$ $\mu m^2/ms$, $\lambda_{\perp} = 0.15 \pm 0.02$ $\mu m^2/ms$, FA = 0.84 ± 0.02 (n = 7, mean ± standard deviation). With the addition of 2% agar gel, DTI derived $\lambda_{\perp}$ or FA was significantly affected while DBSI derived parameters remained unchanged (Fig. 3 – 2 A). A comparable observation was seen in Monte-Carlo simulation data where DTI derived FA decreased while $\lambda_{\|}$, $\lambda_{\perp}$ increased with increasing vasogenic edema (i.e., extra-axonal/extracellular space, non-restricted isotropic diffusion component; Fig. 3 - 2 B) with relatively stable DBSI derived FA, $\lambda_{\|}$, and $\lambda_{\perp}$.

3.3.2 Effect of increased cellularity on DTI derived parameters

In the fixed trigeminal nerves (n = 7), DBSI estimated axonal fiber fraction to be 67 ± 3%, cellularity to be 14 ± 2%, and extra-axonal/extracellular space to be 20 ± 3% of the total signal intensity, consistent with our previously published results supported by immunohistochemistry [18]. Since cellularity is difficult to change experimentally, Monte-Carlo simulation was performed with various extents of extra-fiber cells (i.e., spheres, restricted isotropic diffusion component). Diffusion parameters derived by DTI were significantly affected with increasing cellularity, i.e., DTI derived $\lambda_{\|}$, and FA significantly decreased with increasing cellularity while DBSI derived parameters were largely unaffected (Fig. 3). DTI derived $\lambda_{\perp}$ was minimally affected in contrast to the more profound changes seen in $\lambda_{\|}$. No correlation was shown in FA, $\lambda_{\|}$, and $\lambda_{\perp}$ between DTI and DBSI.

3.3.3 Reducing the number of diffusion encoding direction for trigeminal nerves

There was no discernible difference between 25- vs. 99-direction diffusion encoding scheme in DBSI derived diffusion parameters on data generated using Monte-Carlo simulation (Fig. 3 – 2 B, 3 – 3 and 3 – 4). Similarly consistent findings were also seen in the experimental data using trigeminal nerves combined with varied amounts of 2% agar gel (Fig. 3 - 2 A). The accuracy of diffusion fractions from both 99- and 25-direction DBSI analysis of data from Monte-Carlo simulations ($n = 21$) were evaluated. DBSI derived non-restricted and restricted isotropic diffusion fractions using 99- and 25-direction diffusion schemes (Fig. 3 – 4 A and B) were not different from the simulated true values. DBSI derived restricted and non-restricted isotropic diffusion fractions using 25-direction compared to 99-direction were statistically not different by equivalence tests.

3.3.4 An *in vivo* example of EAE optic neuritis

Diffusion MRI using the 25-direction scheme was performed on optic nerves from one sham mouse and one with optic neuritis due to EAE. Both DBSI and DTI analyses exhibited decreased $\lambda_{\|}$ (DBSI $\lambda_{\|} = 1.38$ vs. $2.10\ \mu m^2/ms$; DTI $\lambda_{\|} = 0.72$ vs. $1.92\ \mu m^2/ms$ for EAE vs. sham) and increased $\lambda_{\perp}$ (DBSI $\lambda_{\perp} = 0.13$ vs. $0.11\ \mu m^2/ms$; DTI $\lambda_{\perp} = 0.20$ vs. $0.10\ \mu m^2/ms$ for

EAE vs. sham) in the EAE-affected optic nerve comparing with those of the sham. In addition to the conventional diffusivities, DBSI derived restricted isotropic diffusion fraction (i.e., the putative cellularity) = 0.25 vs. 0.03, non-restricted isotropic diffusion fraction (i.e., the putative vasogenic edema) = 0.22 vs. 0.02 significantly increased in the optic neuritis-affected nerve comparing with the sham nerve, reflecting the inflammation.

A close examination of the DBSI parameter maps of sham (Fig. 3 – 5 A, B, and C) and EAE-affected (Fig. 3 – 5 D, E, and F) mice suggested the presence of inflammatory cell infiltration evidenced by the increased restricted isotropic diffusion fraction, axonal injury supported by the decreased $\lambda_{\|}$, and demyelination indicated by the increased $\lambda_{\perp}$ in the EAE-affected optic nerve. Apparent heterogeneity of cell infiltration was also seen on the cross-section image of the optic nerve, consistent with a heterogeneous increase in DAPI-positive cell nuclei staining (Fig. 3 – 5 D and D'). Qualitatively, axonal injury (decreased $\lambda_{\|}$) and demyelination (increased $\lambda_{\perp}$) occurred within the regions where increased cellularity (increased restricted isotropic diffusion fraction) was present (Fig. 3 – 5 D, E, and F). However, the presence of increased cellularity does not necessarily correspond to axonal injury or demyelination. These *in vivo* DBSI findings were supported by immunohistochemical staining.

3.4 Discussion

This study investigated the effect of increased cellularity and vasogenic edema, commonly seen in CNS injuries, on the DTI derived diffusion parameters of white matter tracts. Specifically, increased cellularity as evidenced by increased isotropic, restricted diffusion, decreased the DTI derived FA and $\lambda_{\|}$ while having a limited impact on $\lambda_{\perp}$. Increased vasogenic edema, as evidenced by increased non-restricted isotropic diffusion, also decreased the DTI derived FA but increased $\lambda_\perp$ with the extent of impact on $\lambda_\parallel$ depending on the ADC value of edema relative to $\lambda_\parallel$ and $\lambda_\perp$ of axon. These confounding effects were resolved and quantified by the recently developed DBSI analysis [18], as demonstrated herein using data generated by both Monte-Carlo simulation and realistic tissue phantoms. Our prior study used 99-direction diffusion encoding [18]. A 25-direction diffusion encoding scheme [19] was assessed in this study to demonstrate its adequacy for performing DBSI analysis on optic nerves from the mouse at the onset of acute optic neuritis.

The partial volume effect of CSF, i.e., non-restricted (free) isotropic diffusion, on DTI indices has long been recognized, and limits DTI capability in regions abutting CSF, such as periventricular regions that are commonly affected by MS. The inclusion of the isotropic component of free diffusion improved fiber diffusion measurements [27, 28]. However, such modification is insufficient to deal with coexisting CNS inflammation (increased cellularity and vasogenic edema) or tissue loss that may be seen in diseased tissues [29]. To properly model the effect of CNS inflammation and tissue loss, allowing a more accurate evaluation of the diffusion properties of white matter fiber tracts, multiple extra-fiber diffusion components (both restricted and non-restricted isotropic diffusion components) must be identified and quantified. DBSI considers a spectrum of isotropic diffusion components of a wide range of ADC to account for the extra-fiber tissue and pathological components. The current results from fixed normal tissues and gel phantoms, and our previous *in vivo* mouse brain data [18] suggest that the DBSI approach allowed for an accurate estimation of white matter tract diffusion properties in the presence of increased cellularity and vasogenic edema.

The close agreement between the experimental measurements of fixed trigeminal nerve plus gel phantoms and the results from Monte-Carlo simulations using restricted and non-restricted isotropic diffusion components to mimic cells and vasogenic edema supported our approach of including a linear combination of isotropic diffusion spectra to account for the effect of CNS inflammation and tissue loss. One advantage of using DBSI is its capability to resolve crossing fibers while still quantitatively deriving fiber associated anisotropic diffusion tensors to assess the axon and myelin integrity [18]. Previously, a 99-direction diffusion encoding scheme was employed to acquire data for DBSI analysis that was able to resolve crossing fibers and quantifying extra-fiber cellularity and edema [18]. In the case where crossing fibers are not of concern such as when studying optic nerve, a reduced data acquisition scheme may be sufficient for DBSI analysis. In the present study, the 25-direction diffusion scheme was assessed and proved to be adequate and equivalent to the 99-direction scheme for DBSI analysis in coherent white matter tracts to quantify the extent of cellularity and edema. Thus, DBSI analysis may potentially be applied to existing diffusion weighted data acquired using 25- or other multiple-direction encoding schemes with multiple b-values may be suitable for DBSI analysis without reacquiring new data to examine the single coherent fiber tracts.

Similar to previous results on corpus callosum from cuprizone treated mice [18], *in vivo* DBSI derived restricted isotropic diffusion fraction map of optic nerve from the EAE mouse revealed a heterogeneous increase in amount of cellularity closely matching the pattern of DAPI-positive cell nuclei staining of the same nerve (Fig. 3 – 5 D and D’). This result is very encouraging because it demonstrates that DBSI could potentially provide a novel noninvasive index of inflammation in white matter to monitor in real time of cellular infiltration. In contrast, various MR techniques have been used to assess inflammation of optic neuritis, but rarely demonstrated the ability to image cellularity changes non-invasively. For example, gadolinium-enhanced T1W images reflect the leakage of blood-brain barrier [30-32] without information regarding the cellular infiltration. Iron-oxide particles have been used to allow *in vivo* visualization of macrophages, but this method is insensitive to non-phagocytic cells involved in inflammation [33]. An increased optic nerve area (swelling) has also been considered to reflect the severity of inflammation in acute optic neuritis [34, 35]. Unfortunately, this method is highly nonspecific, as a changed nerve cross-sectional size may reflect cell infiltration and/or edema and is further confounded by any tissue loss that may be present [34]. In the present study, axonal injury and myelin damage seen in the EAE-affected optic nerve co-localized with cell infiltration while the region of increased cellularity did not always correspond to visible nerve damage (Fig. 3 – 5 D - F). This is consistent with the pathogenesis of optic neuritis in EAE, i.e., nerve injury originates from the induced CNS inflammation but may not always occur with inflammation, and when it does occur axon injury may extend well outside the region of inflammation [36, 37].

3.6 Acknowledgements

The authors thank Robert Mikesell for his assistance with the immunization of mice to induce EAE. This study was supported in part by the grants from National Institute of Health R01-NS047592 (S.-K.S.), P01-NS059560 (A.H.C.), and National Multiple Sclerosis Society (NMSS) RG 4549A4/1 (S.-K.S).

3.7 References

1. Song, S.K., et al., *Dysmyelination revealed through MRI as increased radial (but unchanged axial) diffusion of water.* Neuroimage, 2002. **17**(3): p. 1429-36.
2. Kim, J.H., et al., *Detecting axon damage in spinal cord from a mouse model of multiple sclerosis.* Neurobiol Dis, 2006. **21**(3): p. 626-32.
3. Sun, S.W., et al., *Noninvasive detection of cuprizone induced axonal damage and demyelination in the mouse corpus callosum.* Magn Reson Med, 2006. **55**(2): p. 302-8.
4. DeBoy, C.A., et al., *High resolution diffusion tensor imaging of axonal damage in focal inflammatory and demyelinating lesions in rat spinal cord.* Brain, 2007. **130**(Pt 8): p. 2199-210.
5. Schmierer, K., et al., *Diffusion tensor imaging of post mortem multiple sclerosis brain.* Neuroimage, 2007. **35**(2): p. 467-77.
6. Werring, D.J., et al., *Diffusion tensor imaging of lesions and normal-appearing white matter in multiple sclerosis.* Neurology, 1999. **52**(8): p. 1626-32.
7. Assaf, Y., et al., *High b-value q-space analyzed diffusion-weighted MRI: application to multiple sclerosis.* Magn Reson Med, 2002. **47**(1): p. 115-26.
8. Pasternak, O., et al., *Free water elimination and mapping from diffusion MRI.* Magn Reson Med, 2009. **62**(3): p. 717-30.
9. Naismith, R.T., et al., *Increased diffusivity in acute multiple sclerosis lesions predicts risk of black hole.* Neurology, 2010. **74**(21): p. 1694-701.
10. Anderson, A.W., et al., *Effects of cell volume fraction changes on apparent diffusion in human cells.* Magn Reson Imaging, 2000. **18**(6): p. 689-95.

11. Lodygensky, G.A., et al., *In vivo MRI analysis of an inflammatory injury in the developing brain.* Brain Behav Immun, 2010. **24**(5): p. 759-67.

12. Wedeen, V.J., et al., *Mapping complex tissue architecture with diffusion spectrum magnetic resonance imaging.* Magn Reson Med, 2005. **54**(6): p. 1377-86.

13. Jensen, J.H., et al., *Diffusional kurtosis imaging: the quantification of non-gaussian water diffusion by means of magnetic resonance imaging.* Magn Reson Med, 2005. **53**(6): p. 1432-40.

14. Liu, C., et al., *Characterizing non-Gaussian diffusion by using generalized diffusion tensors.* Magn Reson Med, 2004. **51**(5): p. 924-37.

15. Assaf, Y. and P.J. Basser, *Composite hindered and restricted model of diffusion (CHARMED) MR imaging of the human brain.* Neuroimage, 2005. **27**(1): p. 48-58.

16. Scherrer, B. and S.K. Warfield, *Parametric representation of multiple white matter fascicles from cube and sphere diffusion MRI.* PLoS One, 2012. **7**(11): p. e48232.

17. Zhang, H., et al., *NODDI: practical in vivo neurite orientation dispersion and density imaging of the human brain.* Neuroimage, 2012. **61**(4): p. 1000-16.

18. Wang, Y., et al., *Quantification of increased cellularity during inflammatory demyelination.* Brain, 2011. **134**(Pt 12): p. 3590-601.

19. Batchelor, P.G., et al., *Anisotropic noise propagation in diffusion tensor MRI sampling schemes.* Magn Reson Med, 2003. **49**(6): p. 1143-51.

20. Kuo, L.W., et al., *Optimization of diffusion spectrum imaging and q-ball imaging on clinical MRI system.* Neuroimage, 2008. **41**(1): p. 7-18.

21. Stanisz, G.J., et al., *An analytical model of restricted diffusion in bovine optic nerve.* Magn Reson Med, 1997. **37**(1): p. 103-11.

22. Stolzenburg, J.U., A. Reichenbach, and M. Neumann, *Size and density of glial and neuronal cells within the cerebral neocortex of various insectivorian species.* Glia, 1989. **2**(2): p. 78-84.

23. Chiang, C.W., et al., *Acute visual function impairment in EAE is primarily caused by optic nerve inflammation as assessed by DBSI* Proc. Intl. Soc. Mag. Reson. Med. , 2011. **20, 3085**.

24. Sun, S.W., et al., *Evolving Wallerian degeneration after transient retinal ischemia in mice characterized by diffusion tensor imaging.* Neuroimage, 2008. **40**(1): p. 1-10.

25. Tu, T.W., et al., *Using absorption-mode images to improve in vivo DTI quality.* Proc. Intl. Soc. Mag. Reson. Med. , 2010. **18, 4001**.

26. Blewitt, E.S., T. Pogmore, and I.C. Talbot, *Double embedding in agar/paraffin wax as an aid to orientation of mucosal biopsies.* Journal of clinical pathology, 1982. **35**(3): p. 365.

27. Papadakis, N.G., et al., *Study of the effect of CSF suppression on white matter diffusion anisotropy mapping of healthy human brain.* Magn Reson Med, 2002. **48**(2): p. 394-8.

28. Alexander, D.C., et al., *Spatial transformations of diffusion tensor magnetic resonance images.* IEEE Trans Med Imaging, 2001. **20**(11): p. 1131-9.

29. Horsfield, M.A. and D.K. Jones, *Applications of diffusion-weighted and diffusion tensor MRI to white matter diseases - a review.* NMR Biomed, 2002. **15**(7-8): p. 570-7.

30. Guy, J., et al., *Gadolinium-DTPA-enhanced magnetic resonance imaging in optic neuropathies.* Ophthalmology, 1990. **97**(5): p. 592-9; discussion 599-600.

31. Hickman, S.J., et al., *Visual recovery following acute optic neuritis--a clinical, electrophysiological and magnetic resonance imaging study.* J Neurol, 2004. **251**(8): p. 996-1005.

32. Qi, X., et al., *Suppression of mitochondrial oxidative stress provides long-term neuroprotection in experimental optic neuritis.* Invest Ophthalmol Vis Sci, 2007. **48**(2): p. 681-91.

33. Vellinga, M.M., et al., *Pluriformity of inflammation in multiple sclerosis shown by ultra-small iron oxide particle enhancement.* Brain, 2008. **131**: p. 800-807.

34. Hickman, S.J., et al., *A serial MRI study following optic nerve mean area in acute optic neuritis.* Brain, 2004. **127**(Pt 11): p. 2498-505.

35. Boretius, S., et al., *MRI of optic neuritis in a rat model.* Neuroimage, 2008. **41**(2): p. 323-34.

36. Gold, R., C. Linington, and H. Lassmann, *Understanding pathogenesis and therapy of multiple sclerosis via animal models: 70 years of merits and culprits in experimental autoimmune encephalomyelitis research.* Brain, 2006. **129**(Pt 8): p. 1953-71.

37. Iglesias, A., et al., *T- and B-cell responses to myelin oligodendrocyte glycoprotein in experimental autoimmune encephalomyelitis and multiple sclerosis.* Glia, 2001. **36**(2): p. 220-34.

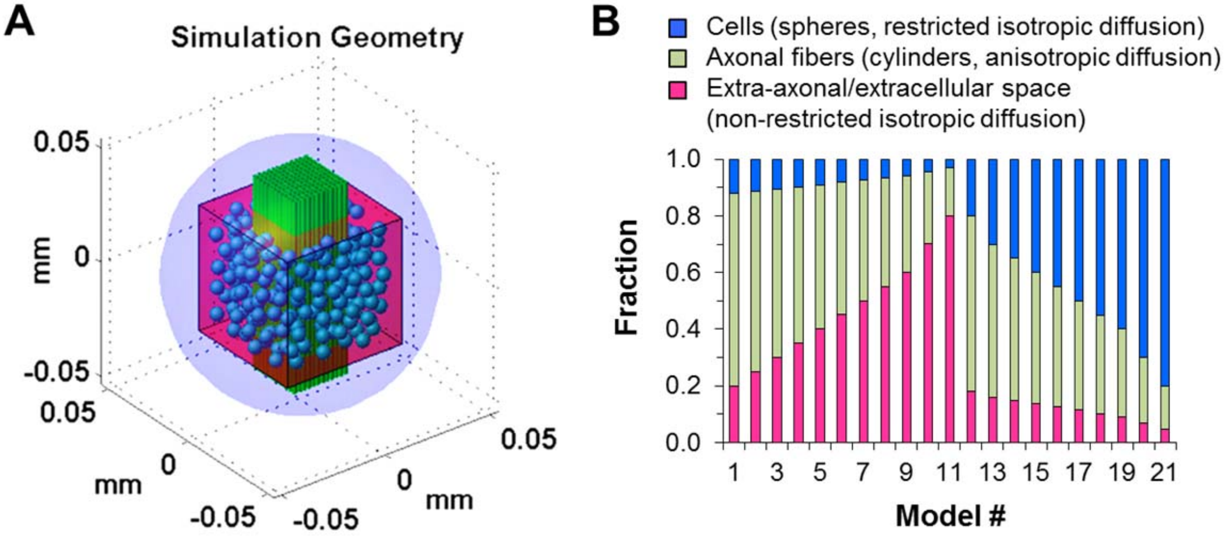

Figure 3–1 (A) A three-dimensional computer-synthesized trigeminal nerve model was constructed for Monte-Carlo simulations. The coherently oriented axonal fiber bundle was composed of tightly packed cylinders of 2-μm diameter (green cylinders), to be described by anisotropic water diffusion components. Cells were represented by spheres of 6-μm diameter (blue spheres) randomly placed surrounding the fiber bundle for simulating restricted isotropic water diffusion in cells. Extra-axonal/extracellular space was represented as non-restricted isotropic diffusion within an imaging voxel. Voxel of interest ($50 \times 50 \times 50\ \mu m^3$ pink cube) was placed in the center of the simulation space for the random walk of water molecules (light blue outer sphere of 90-μm diameter). (B) Baseline trigeminal nerve model (model # 1) consisted of intra- and extra-axonal water diffusion closely associated with axonal fibers (anisotropic diffusion; green bar), cells (restricted isotropic diffusion; blue bar) and extra-axonal/extracellular space (non-restricted isotropic diffusion; pink bar). Similar to the fixed normal trigeminal nerve phantoms with different amount of gel, by gradually increasing the size of imaging voxel, a set of baseline trigeminal nerve model with varying fractions of non-restricted isotropic diffusion (model # 2-11) was used to assess the impact of edema on DTI and DBSI measurements. By increasing the number of spheres, i.e., restricted isotropic diffusion components (model # 12-21), the impact of increased cellularity on DTI and DBSI was also assessed.

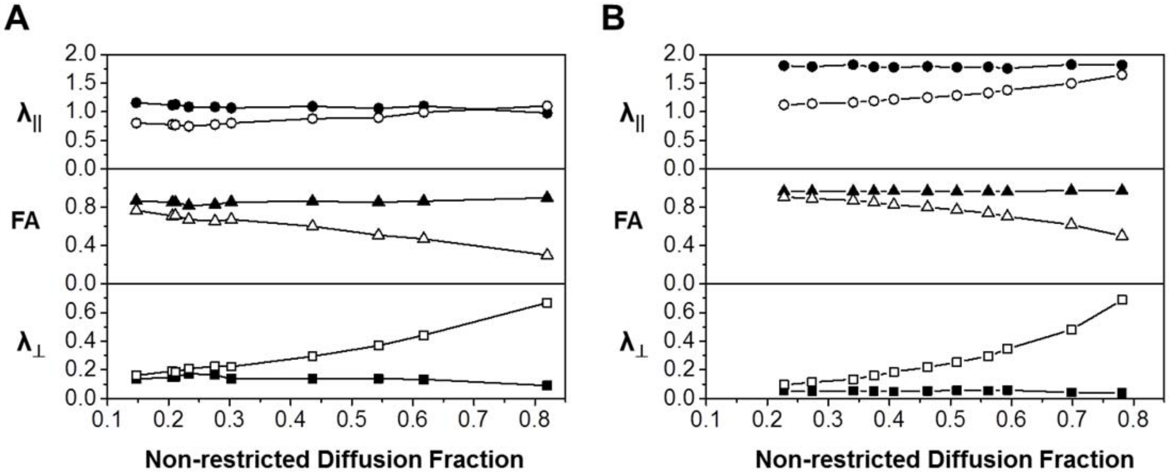

Figure 3–2 The impact of vasogenic edema (or tissue loss) on DTI (open symbols) and DBSI (filled symbols) measurements was mimicked experimentally by adding various amount of 2% agar gel to the fixed normal trigeminal nerve (A) or by increasing the extent, i.e., by enlarging the voxel size without changing the cell or axon bundle content, of non-restricted diffusion component in the Monte-Carlo simulation (B). Experimentally (A), increased gel content resulted in overestimating DTI derived $\lambda_{\|}$ and $\lambda_{\perp}$ (comparing with the nerve only phantom) while underestimated FA (open symbols). The DBSI derived diffusion parameters were not affected by varying the content of the gel (filled symbols). On the data generated using Monte-Carlo simulation (B), increasing non-restricted diffusion components also resulted in overestimating DTI derived $\lambda_{\|}$ and $\lambda_{\perp}$ while underestimated the FA (open symbols). The DBSI derived diffusion parameters (filled symbols) were not affected by increasing non-restricted diffusion component.

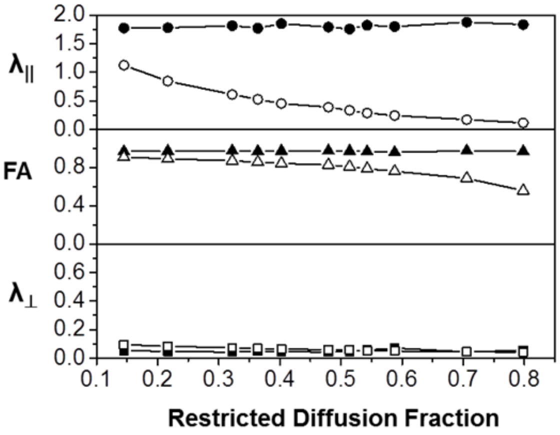

Figure 3–3 Due to the difficulty in making reliable experimental phantoms with varying cell contents, Monte-Carlo simulations with varying contents of the restricted diffusion components were performed to mimic the inflammation associated cellularity increase. Increased content of restricted diffusion component significantly underestimated the DTI derived $\lambda_{\|}$ and FA without an impact on $\lambda_{\perp}$. None of the DBSI derived diffusion parameters was affected by the increased restricted diffusion component.

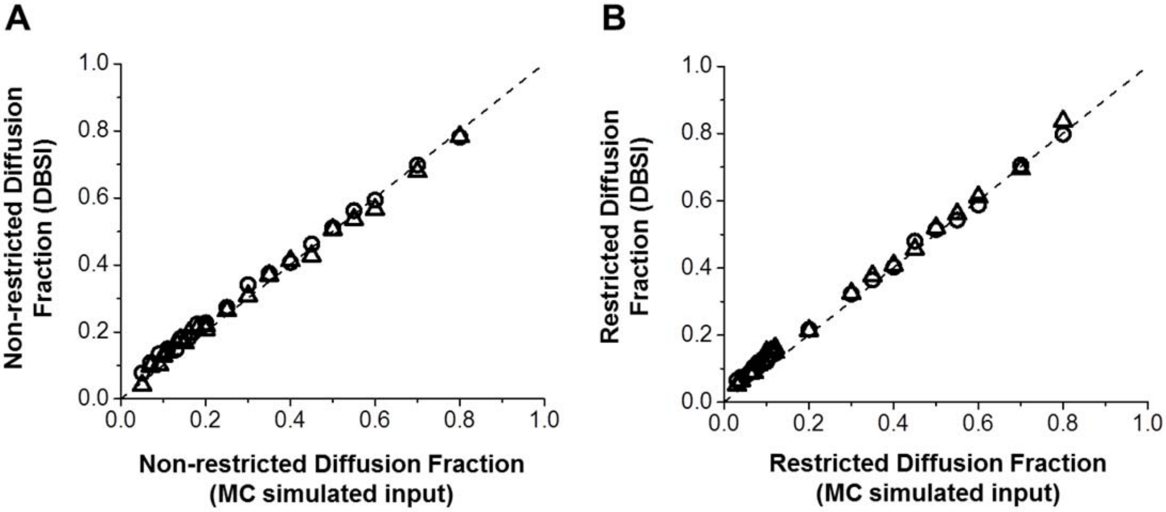

Figure 3–4 DBSI derived non-restricted (A) and restricted isotropic diffusion fraction (B) using 99- (circle) and 25-direction (triangle) diffusion encoding scheme was compared with the input values used for Monte-Carlo simulations. Data obtained from both diffusion encoding schemes fall on the line of identity (black dashed lines in A and B) suggesting that DBSI analysis can be accurately performed using 25-direction encoding scheme in situations where fiber crossing is not of concern.

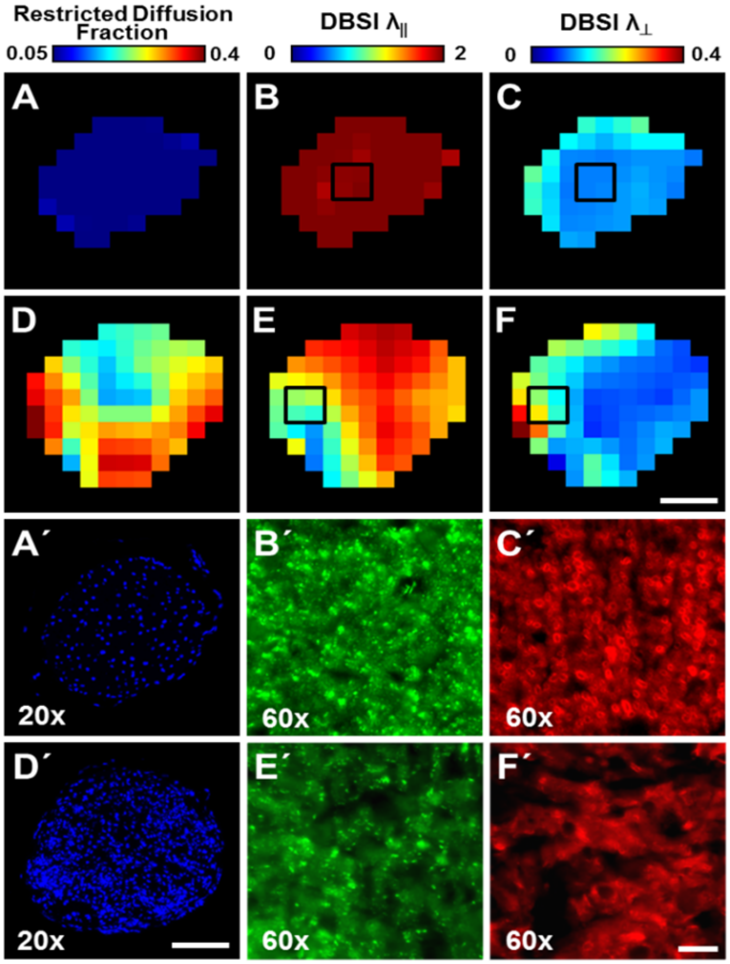

Figure 3–5 Representatives *in vivo* DBSI derived fraction of restricted isotropic diffusion (cellularity), $\lambda_{\parallel}$, and $\lambda_{\perp}$ maps of the optic nerves from the sham and EAE-affected mice were obtained using the 25-direction diffusion encoding scheme. DBSI maps of restricted isotropic diffusion fraction, $\lambda_{\parallel}$, and $\lambda_{\perp}$ of sham (A, B, C) and EAE (D, E, F) mouse optic nerves were compared to immunohistochemistry images of DAPI (blue), SMI-31 (green), MBP (red) from sham (A', B', C') and EAE (D', E', F') optic nerves, corresponding to the selected area from DBSI maps (B, C, E, F). Increased restricted diffusion fraction (0.25 vs. 0.03 for EAE vs. sham), decreased DBSI derived $\lambda_{\parallel}$ (1.38 vs. 2.10 μm^2/ms for EAE vs. sham), and slightly increased DBSI derived $\lambda_{\perp}$ (0.13 vs. 0.11 μm^2/ms for EAE vs. sham) was seen in the optic nerve with optic neuritis, correctly reflecting the optic nerve pathologies seen by immunohistochemistry. For example, the heterogeneously increased cellularity in the EAE optic nerve cross-section map detected by DBSI derived restricted isotropic diffusion fraction closely corresponded to the heterogeneity of DAPI-positive cell nuclei staining intensity. Similarly, correspondence between decreased $\lambda_{\parallel}$ and the decreased SMI-31 (representing loss of axons) and between increased $\lambda_{\perp}$ and the decreased MBP (representing demyelination) staining intensity was also seen. This strong correspondence between *in vivo* DBSI and postmortem immunohistochemistry findings supports that the 25-direction diffusion encoding scheme is adequate for assessing optic nerve pathologies in EAE mice. Scale bars represent 100 μm (F and D'), 10 μm (F').

Appendix 3–A

99-direction DBSI diffusion-encoding scheme (Wang et al., 2011)

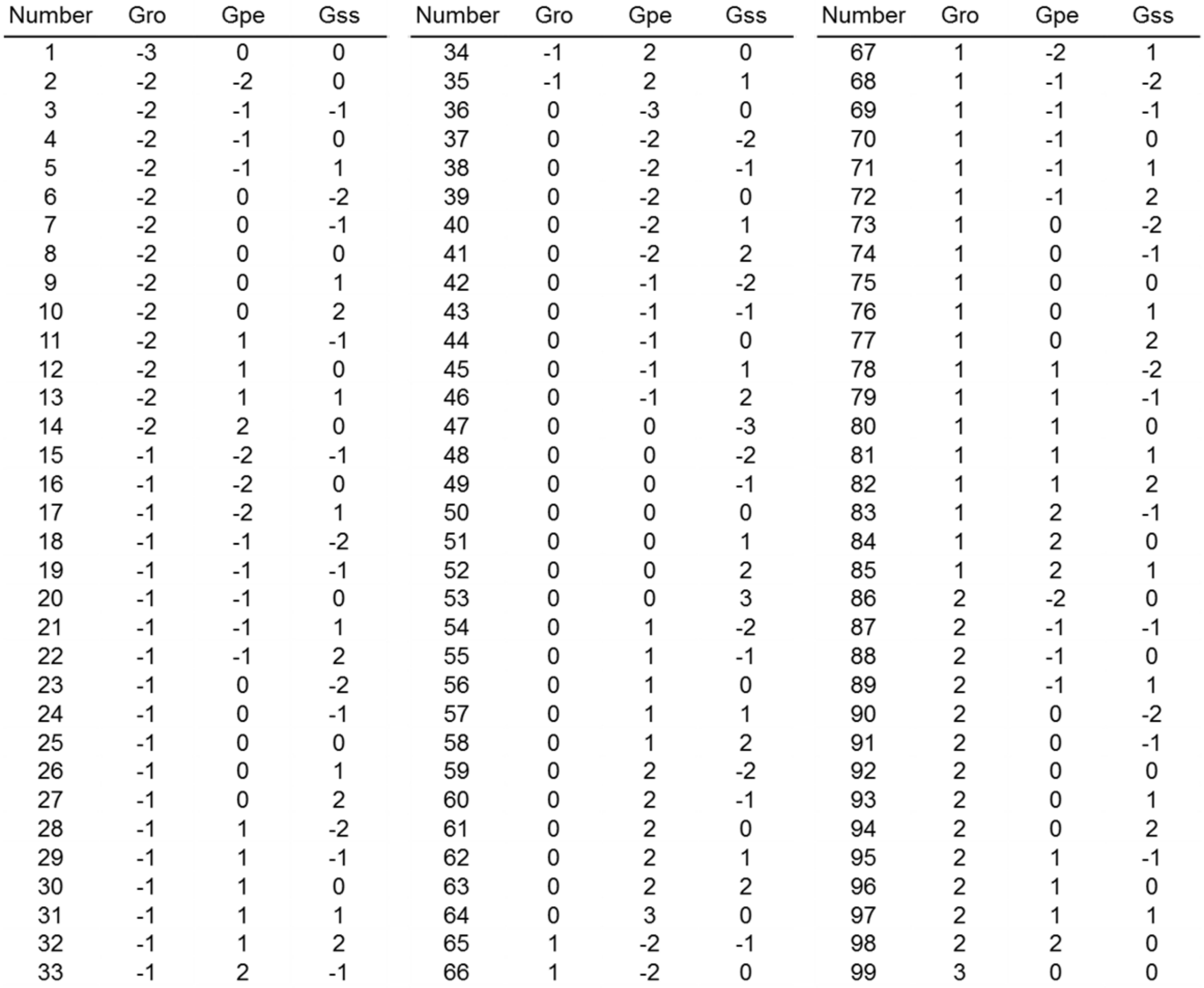

Number	Gro	Gpe	Gss	Number	Gro	Gpe	Gss	Number	Gro	Gpe	Gss
1	-3	0	0	34	-1	2	0	67	1	-2	1
2	-2	-2	0	35	-1	2	1	68	1	-1	-2
3	-2	-1	-1	36	0	-3	0	69	1	-1	-1
4	-2	-1	0	37	0	-2	-2	70	1	-1	0
5	-2	-1	1	38	0	-2	-1	71	1	-1	1
6	-2	0	-2	39	0	-2	0	72	1	-1	2
7	-2	0	-1	40	0	-2	1	73	1	0	-2
8	-2	0	0	41	0	-2	2	74	1	0	-1
9	-2	0	1	42	0	-1	-2	75	1	0	0
10	-2	0	2	43	0	-1	-1	76	1	0	1
11	-2	1	-1	44	0	-1	0	77	1	0	2
12	-2	1	0	45	0	-1	1	78	1	1	-2
13	-2	1	1	46	0	-1	2	79	1	1	-1
14	-2	2	0	47	0	0	-3	80	1	1	0
15	-1	-2	-1	48	0	0	-2	81	1	1	1
16	-1	-2	0	49	0	0	-1	82	1	1	2
17	-1	-2	1	50	0	0	0	83	1	2	-1
18	-1	-1	-2	51	0	0	1	84	1	2	0
19	-1	-1	-1	52	0	0	2	85	1	2	1
20	-1	-1	0	53	0	0	3	86	2	-2	0
21	-1	-1	1	54	0	1	-2	87	2	-1	-1
22	-1	-1	2	55	0	1	-1	88	2	-1	0
23	-1	0	-2	56	0	1	0	89	2	-1	1
24	-1	0	-1	57	0	1	1	90	2	0	-2
25	-1	0	0	58	0	1	2	91	2	0	-1
26	-1	0	1	59	0	2	-2	92	2	0	0
27	-1	0	2	60	0	2	-1	93	2	0	1
28	-1	1	-2	61	0	2	0	94	2	0	2
29	-1	1	-1	62	0	2	1	95	2	1	-1
30	-1	1	0	63	0	2	2	96	2	1	0
31	-1	1	1	64	0	3	0	97	2	1	1
32	-1	1	2	65	1	-2	-1	98	2	2	0
33	-1	2	-1	66	1	-2	0	99	3	0	0

Appendix 3–B

25-direction, icosahedral sampling scheme (Batchelor et al., 2003)

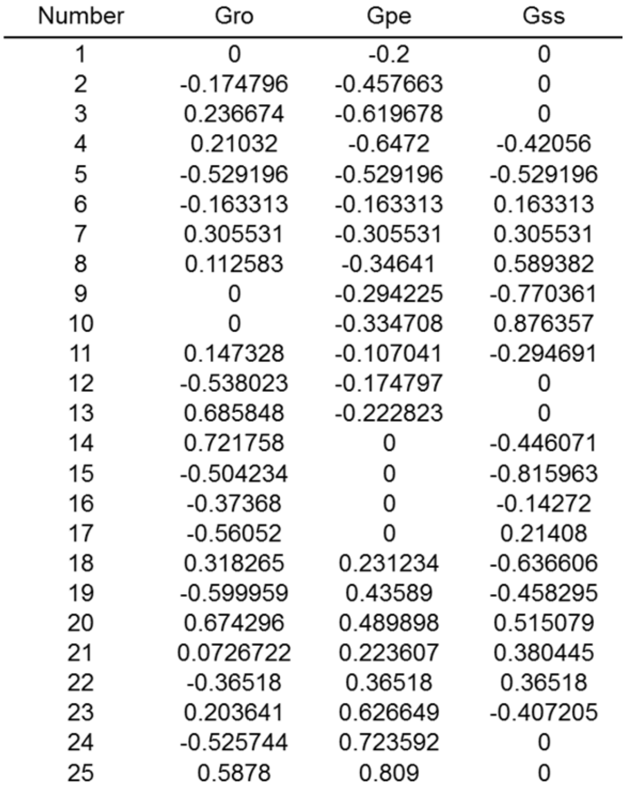

Number	Gro	Gpe	Gss
1	0	-0.2	0
2	-0.174796	-0.457663	0
3	0.236674	-0.619678	0
4	0.21032	-0.6472	-0.42056
5	-0.529196	-0.529196	-0.529196
6	-0.163313	-0.163313	0.163313
7	0.305531	-0.305531	0.305531
8	0.112583	-0.34641	0.589382
9	0	-0.294225	-0.770361
10	0	-0.334708	0.876357
11	0.147328	-0.107041	-0.294691
12	-0.538023	-0.174797	0
13	0.685848	-0.222823	0
14	0.721758	0	-0.446071
15	-0.504234	0	-0.815963
16	-0.37368	0	-0.14272
17	-0.56052	0	0.21408
18	0.318265	0.231234	-0.636606
19	-0.599959	0.43589	-0.458295
20	0.674296	0.489898	0.515079
21	0.0726722	0.223607	0.380445
22	-0.36518	0.36518	0.36518
23	0.203641	0.626649	-0.407205
24	-0.525744	0.723592	0
25	0.5878	0.809	0

Chapter 4

Diffusion basis spectrum imaging detects and differentiates coexisting inflammation, demyelination, and axonal injury in acute optic neuritis

This chapter represents the latest version of a manuscript that is targeted for submission to NeuroImage. (Chia-Wen Chiang, Yong Wang, Tsen-Hsuan Lin, Kathryn Trinkaus, Anne H. Cross, and Sheng-Kwei Song)

Abstract

Diffusion tensor imaging (DTI) measured directional diffusivities have been widely applied to investigate central nervous system (CNS) white matter pathologies. However, CNS white matter pathologies can be complex, and include combinations of demyelination, axon injury/loss, inflammation and edema. The largely isotropic diffusion components of inflammation, namely cellular inflammation and edema, and tissue loss may confound the interpretation of DTI derived biomarkers that focus only on the anisotropic components of white matter pathologies. Thus, a multiple-tensor based diffusion basis spectrum imaging (DBSI) has been proposed to resolve the confounding effect of inflammation. In the present study, a comparison between the newly developed DBSI and the conventional DTI was performed on the optic nerve of mice with optic neuritis due to experimental autoimmune encephalomyelitis (EAE). Notably, optic neuritis is a common early symptom of multiple sclerosis, for which EAE serves as a main model. Both DTI and DBSI correlated well with visual function measured by visual acuity in EAE-affected mice. However, DTI was unable to identify the underlying inflammation due to the associated increase in cellularity and vasogenic edema in acute optic neuritis. The current study demonstrated the

advantage of DBSI in specifically detecting and distinguishing inflammation, demyelination, and axonal injury in optic neuritis due to EAE.

4.1 Introduction

Optic neuritis (ON) is an early symptom in patients of multiple sclerosis (MS) [1, 2]. Accumulated axonal degeneration is now considered as the primary cause of permanent disability in MS [3]. In MS, inflammatory demyelination and axon loss within the optic nerve parallel that seen in the rest of central nervous system (CNS) white matter [3-5]. An imaging method that would non-invasively show optic nerve pathology and that would correlate with visual function due to ON could provide a window to better understand the underlying causes for disease progression in MS. EAE provides a model system to investigate the interrelationship between functional outcome, neuropathology, and imaging.

Previously, several clinical and neurophysiology methods have been used to noninvasively detect functional deficits and structural changes in the visual pathway due to ON. Decreased visual acuity (VA) indicates dysfunction of the visual pathway without specificity of location or underlying pathology (Regan et al., 1977). An increased latency and a reduced amplitude in visual evoked potential (VEP) is considered to reflect demyelination and axonal damage in the optic nerve respectively [6, 7]. Retinal nerve fiber layer thinning and macular volume reduction detected by optical coherence tomography (OCT) reflect axon and ganglion cell (neuron) loss correlating with VEP amplitude and vision tests after ON [8-11]. Recently, by adopting a novel retinal segmentation analysis, OCT has detected the retinal neuronal layer, i.e., ganglion cell layer plus inner plexiform layer and inner nuclear layer plus outer plexiform layer, where reduction in thickness has been associated with disease progression in MS [5, 12-14].

Magnetic resonance imaging (MRI) directly assesses optic nerve integrity and can localize and quantify pathological foci. For example, an increased optic nerve cross-sectional area (swelling) has been considered to reflect the severity of inflammation (cell infiltration and edema) associated with visual impairment in acute ON [15, 16]. Gadolinium (Gd)-enhanced T1-weighted (T1W) lesions in optic nerve, indicating blood-brain barrier dysfunction as a result of inflammation, correlated with visual recovery following acute ON [17, 18].

Decreased axial diffusivity ($\lambda_{\parallel}$, water diffusion parallel to the white matter fibers) detected by diffusion tensor imaging (DTI) correlated with slowed visual recovery [19]. An increased radial ($\lambda_{\perp}$, water diffusion perpendicular to the white matter fibers) and mean diffusivity (MD), and a decreased fractional anisotropy (FA) derived by DTI correlated with long-term visual recovery [20]. Despite the promising predictive results using DTI in acute and chronic ON in humans, DTI cannot reflect the underlying pathologies or cerebrospinal fluid (CSF) contamination, largely reflected as isotropic diffusion, of the voxel being examined. Thus, a new method termed diffusion basis spectrum imaging (DBSI) has been developed to detect and quantify increased cellularity and vasogenic edema associated with inflammation, while more accurately reflecting axonal injury and demyelination [21]. Moreover, DBSI can also detect CSF contamination and resolve crossing fibers within an imaging voxel [21].

Experimental autoimmune encephalomyelitis (EAE) is a widely used animal model of human MS [22]. C57BL/6 mice with EAE induced using myelin oligodendrocyte glycoprotein (MOG) exhibit neurological disability (visual impairment and hind limb paralysis) and white matter pathologies (i.e., inflammation, axonal injury, and demyelination) in the optic nerve and spinal cord similar to MS [23-28].

In the present work, DBSI [21] and conventional DTI [29] analyses were performed to assess optic nerve pathology in MOG-induced EAE-affected mice and sham mice at the onset of ON, defined by the first sign of decreased VA. Following imaging, mice were sacrificed and optic nerve tissues were examined by immunohistochemistry (IHC). The results demonstrated that inflammation, axonal injury and demyelination all correlated well with visual impairment at onset of ON. DBSI detected inflammatory cell infiltration and optic nerve pathology in EAE mice that was consistent with histology, supporting the potential use of DBSI to quantify cellularity, axonal injury and myelin damage in other systems of human disease.

4.2 Materials and Methods

4.2.1 Animals

All procedures involving animals were performed according to the animal protocols approved by the Washington University Animal Studies Committee and in compliance with University policies and procedures on research involving animals.

EAE was induced in 8-week-old female C57BL/6 mice (Jackson Laboratory, Bar Harbor, ME, USA) by subcutaneous immunization with 50 μg myelin oligodendrocyte glycoprotein peptide (MOG_{35-55}) emulsified in incomplete Freund's adjuvant (IFA) containing 50 μg Mycobacterium tuberculosis (MTB), as previously described [30]. Age-matched mice immunized with IFA lacking MOG_{35-55} and MTB served as controls. Pertussis toxin (300 ng; PTX, List Laboratories, Campbell, CA) was injected intravenously on days 0 and 2 post-immunization for EAE and PBS for sham mice. In this study, 10 EAE and 10 sham mice were employed to establish the temporal visual function profile without undergoing MRI. Another cohort of 16 EAE and 5 sham mice was employed to perform MRI measurements when mice with first sign of decreased VA. Optic nerve tissues from 7 EAE and 5 sham mice were perfusion fixed after MRI for histology. Mice were evaluated daily for clinical score using a published 0-5 clinical scoring system: 0, healthy; 1, limp tail; 2, hind limb weakness sufficient to impair righting; 3, one limb paralyzed; 4, two limbs paralyzed; 5, more than two limb paralyzed or the animal is moribund [31], and VA assessment by virtual optomotor system [32, 33].

Significantly decreased VA was seen in one or both eyes in all EAE-affected mice in this study. While all unilaterally affected optic nerves from EAE mice were included, only one optic nerve per animal was randomly selected from the bilaterally affected and the sham-treated animals for statistical analysis.

4.2.2 Optokinetic Tracking Responses

The visual function was assessed daily by optokinetic tracking response (OKR) using a commercially available apparatus and the associated software, OptoMotry (Cerebral Mechanics, Inc., Canada), as described [32, 33]. Briefly, mice were placed on a platform in a closed chamber with a projection of virtual cylinders of varying spatial frequency at 100% contrast. The spatial frequency of the rotating columns was noted at the point when the mouse responded to the rotating columns by moving its head. In this study, VA was defined as the highest spatial frequency, in cycles/degree (c/d), to which the mouse responded. Each mouse eye was independently assessed by changing the rotating direction of the cylinder, i.e., clockwise for left (L) and counterclockwise for right (R) eyes. The baseline VA of each mouse eye was assessed before EAE immunization. Two researchers measured the daily VA for each mouse eye in a blinded fashion.

4.2.3 Magnetic Resonance Imaging

When decreased VA of the mouse eye was confirmed, *in vivo* diffusion MRI experiments were performed on a 4.7-T Agilent DirectDrive™ small-animal MRI system (Agilent

Technologies, Santa Clara, CA) equipped with Magnex/Agilent HD imaging gradient coil (Magnex/Agilent, Oxford, UK) with pulse gradient strength up to 58 G/cm and a gradient rise time ≤ 295 μs. For this, mice underwent 1 % isoflurane/oxygen anesthesia and were placed in a custom-built head holder. Respiratory rate and rectal temperature, maintained at 37 °C, were monitored and controlled by a small animal physiological monitoring system (SAII Inc., NY). An actively-decoupled volume (transmit) /surface (receive) coil pair was used for MR excitation and signal reception, and all image slices were acquired based on previously reported procedures [34]. A final-targeted slice provided a transverse view of mouse brain with the two optic nerves. Diffusion weighted MRI was performed using a multi-echo spin-echo diffusion-weighted sequence [35] with a 25-direction icosahedral sampling scheme [36]. The MR acquisition parameters were: TR 1.5 sec, TE 37 ms, Δ 18 ms, δ 6 ms, field-of-view 22.5 mm × 22.5 mm, data matrix 192 × 192, slice thickness 0.8 mm, and 1 average. The b-values used were distributed from 0 to 2200 s/mm^2, and the total acquisition was 2 hours and 20 minutes.

4.4.4 MR Data Analysis

The acquired diffusion data were analyzed by DBSI to derive axial diffusivity ($\lambda_{\|}$), radial diffusivity ($\lambda_{\perp}$), fractional anisotropy (FA), fiber mean diffusivity (fiber MD), restricted isotropic diffusion fraction (reflecting cells) and non-restricted isotropic diffusion fraction (reflecting extra-axonal and extracellular space) as previously described [21]. Same data were also analyzed using the conventional DTI to calculate $\lambda_{\|}$, $\lambda_{\perp}$, FA and MD [37, 38]. Mouse optic nerve cross-sectional area was estimated by intensity segmentation of the diffusion-weighted image, with diffusion sensitizing gradient perpendicular to optic nerves. Regions of interest (ROI) for DBSI and DTI comparisons were selected using both diffusion-weighted images and FA maps to ensure consistency in ROI selection between animals.

4.2.5 Histological Analysis

Mice were perfusion fixed with 0.01 M phosphate-buffered saline (PBS) followed by 4% paraformaldehyde in 0.01 M PBS immediately after MR imaging. The brains were excised and placed in the fixative containing 4% paraformaldehyde in 0.01M PBS for 24 hours before transferred to 0.01 M PBS for storage at 4 °C until histological analysis. Fixed optic nerves were embedded in 2% agar gel [39] and paraffin followed by sectioning into 5-µm thick transverse slices. Sectioned tissues were deparaffinized, rehydrated, and blocked using a 1:1 mixture of 10% normal goat serum and 2% bovine serum albumin in PBS for 20 minutes at room temperature to prevent nonspecific binding of goat secondary antibody. Sections were incubated in monoclonal anti-phosphorylated neurofilament antibody (SMI-31; 1:1000, Covance, US) to stain non-injured axons, or in rabbit anti-myelin basic protein (MBP) antibody (1:1000, Sigma Inc., MO) to target myelin sheaths at 4 °C overnight. After several rinses, secondary goat anti-mouse IgG and goat anti-rabbit IgG conjugated Alexa 488 (1:800, Invitrogen) were applied respectively at room temperature for 1 hour to visualize the immunoreactivity. After washing, slides were covered using Vectashield Mounting Medium with 4′,6-diamidino-2-phenylindole (DAPI) (Vector Laboratory, Inc., Burlingame, CA) to stain cell nuclei. A Nikon Eclipse 80i fluorescence microscope was used to examined and photograph the IHC-stained optic nerves with the MetaMorph software (Universal Imaging Corporation, Sunnyvale, CA). Tissue sections stained with the same primary antibody were acquired using identical fluorescence light intensity and exposure time. Quantification of the SMI-31-stained intact axons and MBP-stained myelin sheaths (reflecting integrity of axon and myelin sheaths, respectively) was performed using two photographs of each staining at 60x magnification. DAPI-stained cell nuclei were counted using the entire optic nerve at 20x magnification. The IHC quantification protocols were adapted using ImageJ [40] and gray level watershed segmentation (http://bigwww.epfl.ch/sage/soft/watershed/) for assessment of optic nerve integrity.

4.2.6 Statistical Analysis

All data were expressed as mean ± standard deviation (SD). The Wilcoxon two-sample test was used to assess the difference for each measured parameter between 16 eyes from mice with ON and 5 sham eyes based on the median. A statistically significant difference was accepted at 95% confidence level. The Spearman rank correlation coefficients with significant test were calculated between VA and diffusion MRI measured parameters or IHC, and between IHC and diffusion MRI parameters. All statistical analyses were performed using SAS V9.3 (SAS Inc., Cary, NC).

4.3 Results

4.3.1 Visual Acuity

An initial experiment was performed on a cohort of 10 mice immunized to develop EAE and 10 sham-immunized mice to define the clinical course of ON due to EAE over time. The clinical onset (CS = 1) of individual EAE mice was generally observed between day 11 and 13 after immunization, peaking at approximately day 17 (CS = 2.8 ± 1.1). Sham-immunized mice exhibited no clinical signs (CS = 0). The onset of ON in EAE mice was defined as VA ≤ 0.25 c/d (a threshold when the VA is 3 × SD below the mean VA of the sham eyes). Based on this operational definition, ON onset occurred between day 9 and 13 after immunization (Fig. 1). Daily VA of sham eyes (n = 20) was unchanged longitudinally (0.38 ± 0.03 c/d) whereas the VA of EAE-affected eyes decreased, with continued worsening of visual function reaching nadir at day 20. A transient recovery of VA was seen between days 20 – 30, and 30 – 40, followed by progressive decline of visual function after day 40 (Fig. 1). Among 10 EAE-affected mice in this group, unilateral and bilateral ON was seen in 8 (80%) and 2 mice (20%), respectively.

After defining the onset of ON due to EAE in C5BL/6 mice in the first experiment without MRI (Fig 1), a follow-up experiment comparing EAE-affected and sham mice was performed to include MRI examinations at the onset of ON (days 9 – 13 after immunization). In this experiment, VA at the onset of ON was much lower than the operational threshold. Specifically, VA of the ON eyes from EAE-affected mice was 0.15 ± 0.11 c/d (n = 16), whereas the VA of the sham mice were 0.37 ± 0.03 c/d (n = 5), similar to VA of sham mice in Experiment 1 (Fig. 2).

Among the EAE mice with unilateral ON (n = 11; 69%) undergoing MRI in the second experiment, the contralateral eye exhibited significantly reduced VA (0.33 ± 0.03 c/d; n = 11) even though it did not meet the operational definition of ON in this study.

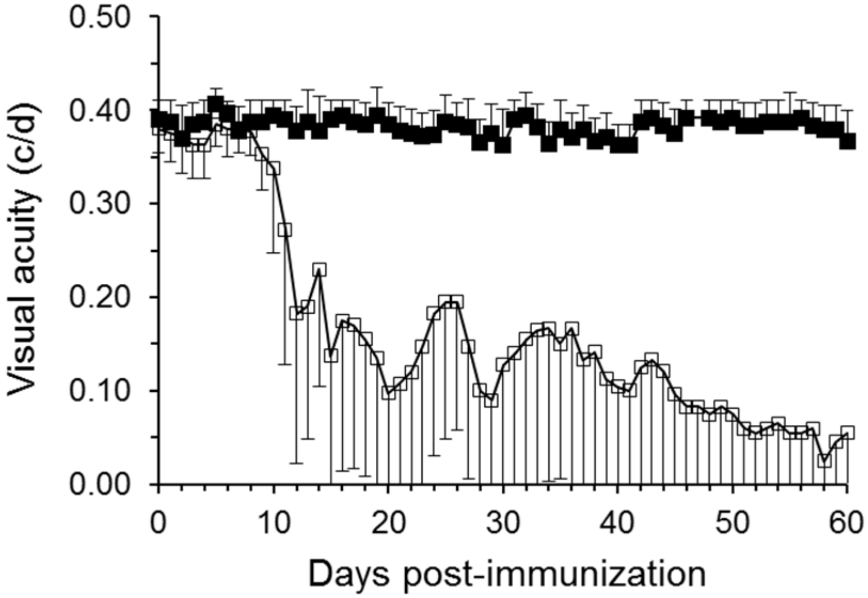

Figure 4 – 1 Time course of visual acuity (VA) for eyes from EAE (open symbols, n = 20) and sham (filled symbols, n = 20) mice. VA of sham eyes was unchanged throughout the time course whereas VA of EAE eyes decreased starting at approximately day 9 after immunization. A transient recover of VA was seen between days 20 – 30, and 30 – 40, followed by progressive degradation of visual function after day 40. Based on the group averaged VA of sham eyes (0.38 ± 0.03 c/d), a VA threshold was defined as the operational threshold to define the acute onset of ON when VA $\leq$ 0.25 c/d. The onset of ON typically occurred during day 9 to 13 after immunization.

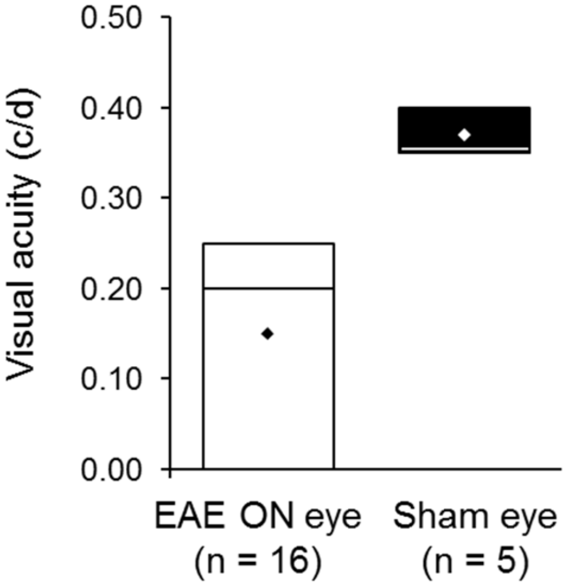

Figure 4 – 2 Group comparison of VA for sham and EAE eyes at the onset of ON exhibited a wide range of VA at the onset of the disease. The group averaged VA was: 0.15 ± 0.11 vs. 0.37 ± 0.03 c/d for EAE ON (n = 16) vs. sham eye (n = 5).

4.3.2 Optic nerve MRI

Representative *in vivo* diffusion-weighted images and corresponding DTI and DBSI derived parameter maps exhibited changes in optic nerves from EAE mice with ON compared with optic nerves of the sham group (Fig. 3). Results are summarized in Table 1. Optic nerve cross-sectional area was increased in EAE mice with ON ($65 \pm 15 \times 10^{-3}$ mm^2, n = 16, Fig. 3A) compared with sham optic nerves ($51 \pm 2 \times 10^{-3}$ mm^2, n = 5; $P < 0.002$, Table 1) at onset of ON. Optic nerve $\lambda_{\|}$ (1.51 ± 0.29 µm^2/ms, Fig. 3B) in EAE mice with ON was significantly decreased compared with sham mice (1.89 ± 0.09 µm^2/ms; $P < 0.002$, Table 1) using DTI. In contrast, DBSI derived optic nerve $\lambda_{\|}$ (1.93 ± 0.23 µm^2/ms, Fig. 3D) was not significantly decreased compared with the sham mice (2.10 ± 0.04 µm^2/ms; $P > 0.1$, Table 1). Optic nerve $\lambda_{\perp}$ of mice with ON was significantly increased whether derived by DTI (0.20 ± 0.04 µm^2/ms) or by DBSI (0.14 ± 0.03 µm^2/ms; Table 1) compared with that of the sham group (DTI: 0.11 ± 0.01 µm^2/ms, Fig. 3C; DBSI: 0.11 ± 0.01 µm^2/ms, Fig. 3E). Additionally, the DBSI derived restricted isotropic diffusion component increased in the optic nerves of mice with ON (0.07 ± 0.06 vs. 0.03 ± 0.01 for controls, Fig. 3F; $P < 0.02$, Table 1). Similarly, the DBSI derived non-restricted diffusion component in the optic nerves of EAE mice with ON (0.14 ± 0.04) also increased comparing with the controls (0.03 ± 0.01, Fig. 3G, $P < 0.002$, Table 1). The DTI derived MD in optic nerves of EAE mice with ON (0.64 ± 0.09 µm^2/ms) was lower than that of the sham optic nerves, but did not reach statistical significance (0.70 ± 0.03 µm^2/ms; $P > 0.09$, Table 1). All DTI and DBSI parameters correlated with VA (Table 2).

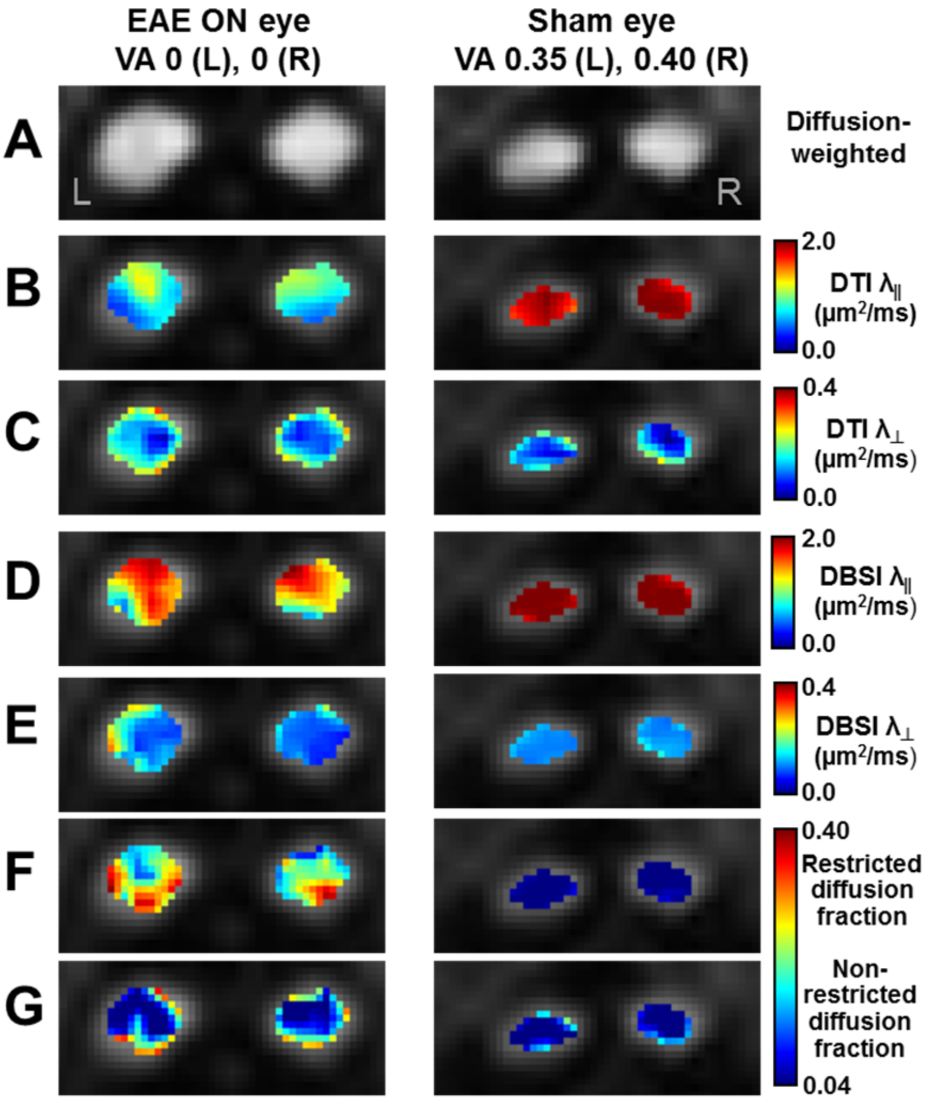

Figure 4 – 3 Representatives of *in vivo* diffusion weighted image (A) and the corresponding DTI (B, C) and DBSI (D-G) index maps of the optic nerve from EAE and sham mice. Increased cross-sectional area at the onset of ON may be a consequence of the inflammation (cell infiltration and vasogenic edema) of optic nerve (A). Decreased $\lambda_{\|}$ and increased $\lambda_{\perp}$ derived by DTI and DBSI was seen in the EAE eye of ON suggesting axonal and myelin damage (B – E). DTI derived $\lambda_{\|}$ was slightly lower than that derived by DBSI, likely resulting from the confounding effect of inflammation, i.e. cellularity and vasogenic edema. Heterogeneity of DTI derived $\lambda_{\|}$ was apparent (B), overall lower than that of DBSI (D), was largely in parallel with the intensity distribution of DBSI derived restricted diffusion fraction map (F). The significantly decreased DTI derived $\lambda_{\|}$ closely corresponded with the increased restricted diffusion fraction (putatively reflecting increased cellularity). DBSI derived $\lambda_{\|}$ was independent of cellularity changes (B, F). Both DTI and DBSI derived $\lambda_{\perp}$ increased (suggesting myelin damage; C and E) in optic nerves from EAE compared with sham mice. DBSI derived non-restricted diffusion fraction (G) did not change appreciably in this EAE mouse except at the periphery of the nerve (a potential contamination of cerebrospinal fluid surrounding the optic nerve). Note, the contamination of CSF was removed from all other parameters by DBSI.

Table 4 – 1 Summary of median (Q1, Q3) for MR derived parameters in EAE with ON and Sham eyes at the onset of ON

	DTI		DBSI	
Measure[2]	EAE ON (n = 16)	Sham (n = 5)	EAE ON (n = 16)	Sham (n = 5)
Optic nerve area	59.89 (54.76, 71.87) **	51.33 (51.33, 51.33)		
$\lambda_{\parallel}$	1.58 (1.41, 1.73) **	1.90 (1.84, 1.94)	1.91 (1.80, 2.10)	2.08 (2.08, 2.09)
$\lambda_{\perp}$	0.19 (0.17, 0.24) **	0.11 (0.11, 0.11)	0.14 (0.12, 0.15) *	0.11 (0.11, 0.12)
FA	0.84 (0.80, 0.89) **	0.94 (0.94, 0.94)	0.92 (0.91, 0.94) *	0.94 (0.94, 0.95)
MD or fiber MD	0.66 (0.62, 0.70)	0.69 (0.69, 0.70)	0.72 (0.70, 0.78)	0.77 (0.77, 0.77)
Restricted[3]			0.06 (0.05, 0.08) *	0.03 (0.02, 0.03)
Non-restricted[3]			0.13 (0.12, 0.16) **	0.03 (0.02, 0.04)
Restricted plus non-restricted			0.19 (0.15, 0.23) **	0.05 (0.05, 0.07)

[1] 25th % quartile (Q1), 75th % quartile (Q3);

[2] Optic nerve area in unit of mm^2; axial diffusivity ($\lambda_{\parallel}$), radial diffusivity ($\lambda_{\perp}$), mean diffusivity (MD) in unit of $\mu m^2/ms$;

[3] Restricted and non-restricted isotropic diffusion fraction;

*, $P < 0.02$; **, $P < 0.002$ from Wilcoxon two-sample tests;

Table 4 – 2 Summary of visual acuity correlations for MR derived parameters and immunohistochemistry of optic nerve in EAE with ON and sham eyes at onset of ON

Measure[1]	Visual acuity	
Optic nerve area	-0.69	$P = 0.0005$
DTI $\lambda_{\parallel}$	0.86	$P < 0.0001$
DTI $\lambda_{\perp}$	-0.75	$P < 0.0001$
DTI FA	0.88	$P < 0.0001$
DTI MD	0.62	$P = 0.003$
DBSI $\lambda_{\parallel}$	0.66	$P = 0.0012$
DBSI $\lambda_{\perp}$	-0.63	$P = 0.0022$
DBSI FA	0.71	$P = 0.0003$
DBSI fiber MD	0.61	$P = 0.0034$
Restricted[2]	-0.72	$P = 0.0003$
Non-restricted[2]	-0.75	$P < 0.0001$
Restricted plus non-restricted	-0.82	$P < 0.0001$
SMI-31 counts	0.76	$P = 0.0039$
MBP area	0.81	$P = 0.0013$
DAPI counts	-0.68	$P = 0.001$

[1] Optic nerve area in unit of mm^2; axial diffusivity ($\lambda_{\parallel}$), radial diffusivity ($\lambda_{\perp}$), mean diffusivity (MD) in unit of $\mu m^2/ms$; visual acuity in unit of c/d; SMI-31; fractional anisotropy (FA) in no unit; DAPI counts in unit of # per mm^2; MBP in unit of area %;

[2] Restricted and non-restricted isotropic diffusion fraction;

4.3.3 Immunohistochemistry of optic nerve

Post-MRI optic nerve sections exhibited a heterogeneous overall increase in DAPI-positive (blue color) nuclear staining in the optic nerve from a representative EAE mouse at the onset of ON compared with those of a representative sham mouse (Fig. 4A). Both SMI-31 and MBP staining were examined from the center of the optic nerve at 60× magnification, corresponding to the highlighted regions of the 20× magnified DAPI images (gray rectangle). A decrease in SMI-31-positive (green color) healthy axons and MBP-positive (red color) myelinated axons was also seen in the optic nerve from an $MOG_{35\text{-}55}$ -immunized mouse with ON compared with the sham optic nerve (Fig. 4B and C). A statistically significant increase in DAPI-positive counts was seen in optic nerve of EAE mice with ON ($6.6 \pm 4.1 \times 10^3$ per mm^2, n = 7) comparing with that of the sham ($3.5 \pm 0.7 \times 10^3$ per mm^2, n = 5, $P < 0.05$; Fig. 4D). Axon and myelin integrity assessed by SMI-31 (Fig. 4E), and MBP (Fig. 4F) was significantly decreased in the optic nerves of EAE mice with ON (SMI-31: $5.7 \pm 1.7 \times 10^5$ vs. $7.4 \pm 0.3 \times 10^5$ per mm^2, $P < 0.01$; MBP: 36 ± 4 vs. 45 ± 3 in area%, $P < 0.01$).

4.3.4 Correlating DTI and DBSI with immunohistochemistry

Both DTI (r = 0.86, $P = 0.0003$; Fig. 5A) and DBSI (r = 0.73, $P = 0.0071$; Fig. 5D) derived $\lambda_{\|}$ significantly correlated with SMI-31-positive axon counts in optic nerves from both EAE with ON (n = 7) and sham (n = 5). Similarly, both DTI (r = -0.83, $P = 0.0008$; Fig. 5B) and DBSI (r = -0.85, $P = 0.0005$; Fig. 5E) derived $\lambda_{\perp}$ negatively correlated with MBP-positive staining. The DTI derived MD decreased with increasing DAPI counts (r = -0.82, $P = 0.001$; Fig. 5C). DBSI derived restricted isotropic diffusion fraction (putative cellularity marker derived by DBSI) significantly correlated with DAPI counts (r = 0.81, $P = 0.0013$; Fig. 5F).

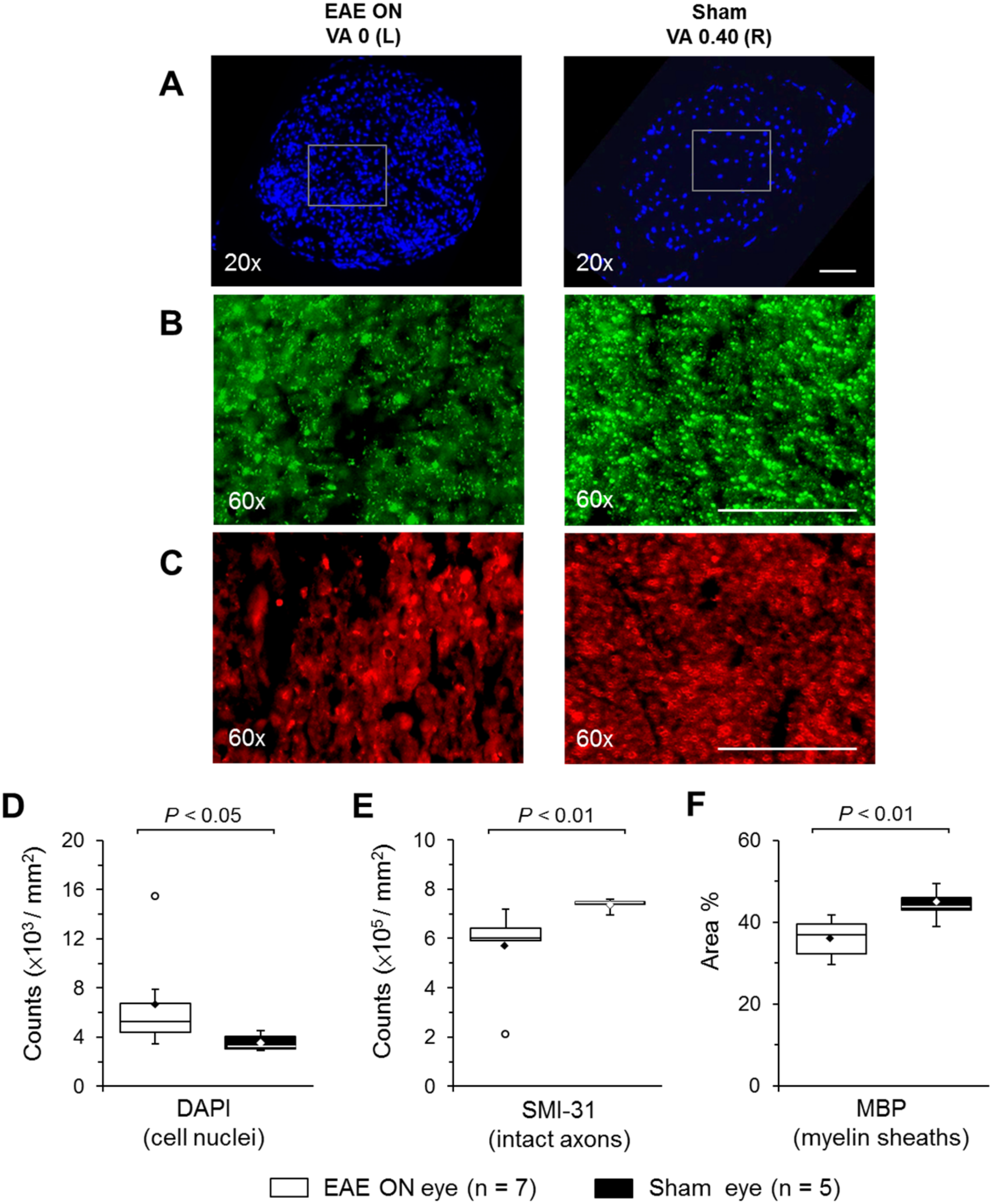
EAE ON
VA 0 (L)
Sham
VA 0.40 (R)
A
20x
20x
B
60x
60x
C
60x
60x
D
P < 0.05
Counts (×10³ / mm²)
20
16
12
8
4
0
DAPI
(cell nuclei)
E
P < 0.01
Counts (×10⁵ / mm²)
10
8
6
4
2
0
SMI-31
(intact axons)
F
P < 0.01
Area %
60
40
20
0
MBP
(myelin sheaths)
EAE ON eye (n = 7)
Sham eye (n = 5)

Figure 4 – 4 Representative immunohistochemistry staining of optic nerves from mice at onset of ON after MRI, same nerves as seen in Fig. 3. DAPI-positive staining (A) matched the restricted isotropic diffusion fraction in Fig. 3F of the optic nerve from the EAE mouse. Both SMI-31-positive staining (reflecting axonal integrity; B) and MBP-positive myelin sheaths (reflecting myelin integrity; C) were examined from the center of the optic nerve at 60× magnification, highlighted in A (gray rectangle), revealed discernible loss of staining intensity suggesting both axon and myelin damage. Quantification of staining results clearly shows inflammation (D), axonal injury (E), and demyelination (F) coexisted and were significant at the onset of ON. Scale bar = 50 μm.

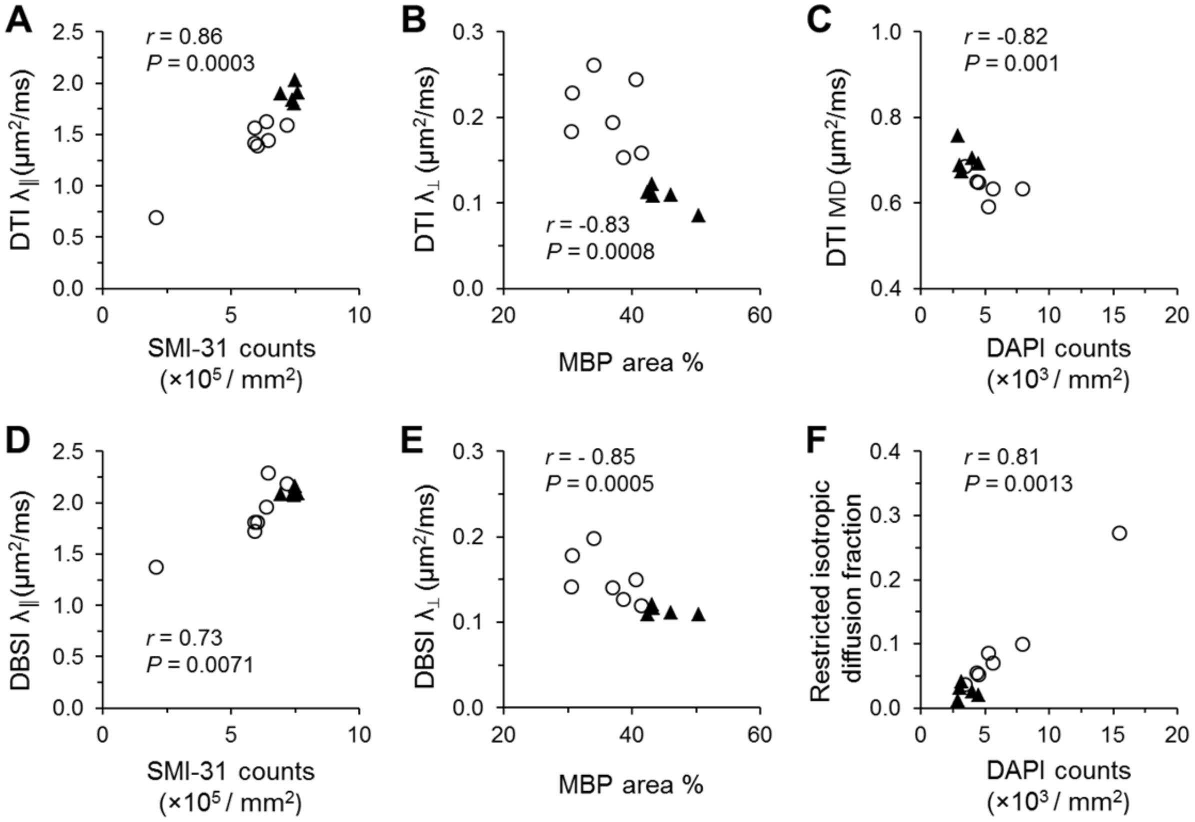

Figure 4 – 5 Correlations between DTI and DBSI derived $\lambda_\parallel$ with SMI-31 positive axon counts (A, D), DTI and DBSI derived $\lambda_\perp$ and MBP positive area (B, E), DTI derived MD and DAPI positive nuclei counts (C), and DBSI derived restricted diffusion fraction and DAPI positive nuclei counts in EAE (n = 7, open circle) and sham eye (n = 5, black triangle). Both DTI and DBSI derived $\lambda_\parallel$ and $\lambda_\perp$ significantly correlated with SMI-31 and MBP respectively (A and D, B and E). The decreased DTI derived MD strongly correlated with increased DAPI counts, clearly demonstrating the impact of inflammation on DTI derived diffusivity (C). The increase in restricted isotropic diffusion fraction also correlated with increased DAPI counts (F). Results suggested that both DTI and DBSI derived $\lambda_\parallel$ and $\lambda_\perp$ are sensitive to optic nerve pathologies at the onset of ON. However, inflammation associated cellularity confounded DTI derived diffusivity thus could lead to false positive conclusion due to underestimation of $\lambda_\parallel$ and MD.

4.4 Discussion

In this paper, we use a virtual optomotor system to longitudinally assess optic nerve function in ON due to MOG_{35-55} -induced EAE in C57BL/6 female mice. The method was sensitive to reduced visual acuity in mice, as confirmed by histopathology, and allowed detection of early clinical ON. ON was almost universal in EAE-affected mice, preceding other clinical signs of EAE by 2 or more days in most cases. We then demonstrated the use of a new imaging method, DBSI, to simultaneously detect inflammation, demyelination, and axonal injury in live mice with acute ON detect by the virtual optomotor system. We compared DBSI to conventional DTI in the assessment of acute ON in mice and correlated results using each technique with measures of axon integrity, myelin integrity and cellular infiltration determined by immunohistochemistry.

Results demonstrated that both DTI and DBSI derived $\lambda_{\|}$ (decreased, reflecting axonal injury) and $\lambda_{\perp}$ (increased, reflecting myelin damage) correlated with VA and with axon (SMI-31 vs. $\lambda_{\|}$) and myelin (MBP vs. $\lambda_{\perp}$) integrity assessed with IHC. Unlike DTI, DBSI can measure restricted (putatively reflecting cells) and non-restricted (putatively reflecting vasogenic edema) isotropic diffusion tensor fractions. These isotropic fractions were each significantly increased in the optic nerves of mice during acute ON. Consistent with the initial report (Wang et al., 2011), the increased fraction of restricted diffusion tensor component correlated well with increased cellularity assessed by DAPI staining. These data further supported the potential of DBSI as a tool to measure cellularity associated with inflammation. The effects of inflammation associated increase in cellularity and edema to confound DTI derived parameters was evident.

Many reports have demonstrated the effect of inflammation on MRI findings [15, 18, 20, 41, 42]. For example, the optic nerve cross-sectional area has been shown to detect optic nerve inflammation in ON patients [15, 43]. Our observation of a significant increase in optic nerve cross-sectional area in acute ON due to EAE (Fig. 3A and Table 1) was consistent with previous reports in ON patients. However, increased optic nerve cross-sectional area [15] is not specific to a particular pathology, and is likely the result of both increased cellularity and edema. Changes seen in optic nerve cross-sectional area may also be confounded by concurrent tissue loss due to axonal degeneration.

Prior studies have reported DTI derived diffusivity and anisotropy measures in optic nerves of ON-affected mice and humans that were not always as expected [20, 24, 44]. Despite the prevailing notion that axon loss is the main determinant of long-term disability, radial diffusivity, a putative marker of myelin loss, correlated best with visual recovery in human ON using DTI [20]. It is likely that the increased DTI-derived radial diffusivity seen in optic nerves of eyes with remote ON is due to a combination of demyelination and also increased isotropic diffusion due to axon loss.

The impact of isotropic components of inflammation, i.e., inflammatory cell infiltration and vasogenic edema, on DTI derived parameters was observed in the current study. Despite the same trend of changes in both DTI and DBSI derived $\lambda_{\|}$ and $\lambda_{\perp}$ in the optic nerve of EAE mice at ON onset, DTI derived $\lambda_{\|}$ was lower and $\lambda_{\perp}$ was higher than that derived by DBSI (Table 1). The underestimation of DTI derived $\lambda_{\|}$ in the optic nerve of EAE mice could be due to the contribution of restricted diffusion of the increased cellularity [21, 45]. The overestimation of DTI derived $\lambda_{\perp}$, in contrast, was likely the effect of increased vasogenic edema [46, 47]. This is consistent with our histological findings, and also with the DBSI results revealing the increased isotropic fractions of restricted diffusion (cellularity) and high diffusion (vasogenic edema) in the optic nerve of EAE mice at ON onset. These pathological findings have also been observed by others using conventional histology [25, 26].

In addition to the directional diffusivity, the effect of increased cellularity and edema was also seen in both DTI derived MD and FA (Table 1). The significantly decreased FA was a result of the synergistic effect of the increased cellularity [21] and vasogenic edema [46, 47] while the less significantly decreased MD was a result of the opposite effect of increased cellularity (decrease MD) and vasogenic edema (increased MD). In the current study, increased cellularity seemed to dominate the diffusion MRI parameters in the optic nerve of EAE mice at the ON onset, supported by the strong negative correlation between MD and DAPI positive nuclei counts ($r = -0.82$, $P = 0.001$; Fig. 5C), and strong positive correlation between DBSI derived restricted diffusion fraction and DAPI counts ($r = 0.81$, $P = 0.0013$; Fig. 5F).

Our findings from diffusion MRI and IHC were consistent with the presence of axonal injury early in MS/EAE. Inflammation, demyelination, and axonal injury were all observed in the optic nerves at the onset of ON. All MRI and IHC measured optic nerve pathology markers correlated with VA (Table 2) at the onset of ON, suggesting the injured optic nerve indeed contributed to the visual functional deficit. Our pilot results revealed no loss of RGC cells (determined using FluoroGold injected stereotactically into superior colliculi followed by RGC counts at day 10 - 12 post-immunization) in EAE mice at ON onset, 387 ± 11 ($n = 7$, EAE) vs. 395 ± 14 ($n = 5$, sham), and preliminary analysis revealed no changes in thickness of the retina (203 ± 7 for EAE, $n = 6$ vs. 200 ± 13 µm for sham, $n = 6$). Although not definitive, our pilot data suggested that there was no RGC loss or retinal thickness change (swelling or atrophy) at the onset of ON to account for the visual loss. Instead, the present study implicates a retrograde optic nerve degeneration leading to RGC loss and retinal atrophy as the disease progresses [25, 48].

This could be consistent with the gradual decline in vision observed in the longitudinal experiment after 35 days post-immunization.

In conclusion, both DTI and DBSI were able to reflect visual function measured by VA. However, the underlying pathological specificity was lost in DTI in the presence of inflammation due to the confounding effects of the associated increase in cellularity and vasogenic edema. In contrast, DBSI was able to discern and measure these inflammation-related pathologies. The current study clearly demonstrated the advantage of DBSI in specifically detecting and distinguishing inflammation, demyelination, and axonal injury in optic nerves of EAE mice at the onset of ON. Application of DBSI to human CNS imaging may expand the ability to detect and characterize inflammation.

4.5 Acknowledgements

The authors thank Bob Mikesell for his assistance with the immunization of mice to induce EAE. This study was supported in part by the grants from National Institute of Health R01-NS047592 (S.-K.S.), P01-NS059560 (A.H.C.), and National Multiple Sclerosis Society (NMSS) RG 4549A4/1 (S.-K.S).

4.6 References

1. Arnold, A.C., *Evolving management of optic neuritis and multiple sclerosis.* Am J Ophthalmol, 2005. **139**(6): p. 1101-8.
2. Frohman, E.M., et al., *The neuro-ophthalmology of multiple sclerosis.* Lancet Neurol, 2005. **4**(2): p. 111-21.
3. Trapp, B.D., R. Ransohoff, and R. Rudick, *Axonal pathology in multiple sclerosis: relationship to neurologic disability.* Curr Opin Neurol, 1999. **12**(3): p. 295-302.
4. Noseworthy, J.H., et al., *Medical progress: Multiple sclerosis.* New England Journal of Medicine, 2000. **343**(13): p. 938-952.
5. Saidha, S., et al., *Relationships Between Retinal Axonal and Neuronal Measures and Global Central Nervous System Pathology in Multiple Sclerosis.* Jama Neurology, 2013. **70**(1): p. 34-43.
6. Bodis-Wollner, I., et al., *Visual evoked potentials and the visuogram in multiple sclerosis.* Ann Neurol, 1979. **5**(1): p. 40-7.
7. Stöhr, M., J. Dichgans, and U.W. Buettner, *Evozierte Potentiale. 3rd ed.* 3rd ed1996, Berlin: Springer-Verlag.
8. Burkholder, B.M., et al., *Macular Volume Determined by Optical Coherence Tomography as a Measure of Neuronal Loss in Multiple Sclerosis.* Archives of Neurology, 2009. **66**(11): p. 1366-1372.
9. Costello, F., et al., *Quantifying axonal loss after optic neuritis with optical coherence tomography.* Ann Neurol, 2006. **59**(6): p. 963-9.
10. Trip, S.A., et al., *Retinal nerve fiber layer axonal loss and visual dysfunction in optic neuritis.* Ann Neurol, 2005. **58**(3): p. 383-91.

11. Fisher, J.B., et al., *Relation of visual function to retinal nerve fiber layer thickness in multiple sclerosis.* Ophthalmology, 2006. **113**(2): p. 324-32.

12. Saidha, S., et al., *Microcystic macular oedema, thickness of the inner nuclear layer of the retina, and disease characteristics in multiple sclerosis: a retrospective study.* Lancet Neurol, 2012. **11**(11): p. 963-72.

13. Saidha, S., et al., *Primary retinal pathology in multiple sclerosis as detected by optical coherence tomography.* Brain, 2011. **134**: p. 518-533.

14. Syc, S.B., et al., *Optical coherence tomography segmentation reveals ganglion cell layer pathology after optic neuritis.* Brain, 2012. **135**: p. 521-533.

15. Hickman, S.J., et al., *A serial MRI study following optic nerve mean area in acute optic neuritis.* Brain, 2004. **127**(Pt 11): p. 2498-505.

16. Hickman, S.J., et al., *Detection of optic nerve atrophy following a single episode of unilateral optic neuritis by MRI using a fat-saturated short-echo fast FLAIR sequence.* Neuroradiology, 2001. **43**(2): p. 123-128.

17. Hickman, S.J., et al., *Visual recovery following acute optic neuritis--a clinical, electrophysiological and magnetic resonance imaging study.* J Neurol, 2004. **251**(8): p. 996-1005.

18. Qi, X., et al., *Suppression of mitochondrial oxidative stress provides long-term neuroprotection in experimental optic neuritis.* Invest Ophthalmol Vis Sci, 2007. **48**(2): p. 681-91.

19. Naismith, R.T., et al., *Disability in optic neuritis correlates with diffusion tensor-derived directional diffusivities.* Neurology, 2009. **72**(7): p. 589-94.

20. Naismith, R.T., et al., *Radial diffusivity in remote optic neuritis discriminates visual outcomes.* Neurology, 2010. **74**(21): p. 1702-10.

21. Wang, Y., et al., *Quantification of increased cellularity during inflammatory demyelination.* Brain, 2011. **134**(Pt 12): p. 3590-601.

22. Gold, R., C. Linington, and H. Lassmann, *Understanding pathogenesis and therapy of multiple sclerosis via animal models: 70 years of merits and culprits in experimental autoimmune encephalomyelitis research.* Brain, 2006. **129**(Pt 8): p. 1953-71.

23. Kim, J.H., et al., *Detecting axon damage in spinal cord from a mouse model of multiple sclerosis.* Neurobiol Dis, 2006. **21**(3): p. 626-32.

24. Sun, S.W., et al., *Selective vulnerability of cerebral white matter in a murine model of multiple sclerosis detected using diffusion tensor imaging.* Neurobiol Dis, 2007. **28**(1): p. 30-8.

25. Quinn, T.A., M. Dutt, and K.S. Shindler, *Optic neuritis and retinal ganglion cell loss in a chronic murine model of multiple sclerosis.* Front Neurol, 2011. **2**: p. 50.

26. Matsunaga, Y., et al., *Visual functional and histopathological correlation in experimental autoimmune optic neuritis.* Invest Ophthalmol Vis Sci, 2012. **53**(11): p. 6964-71.

27. Wang, D., et al., *Astrocyte-associated axonal damage in pre-onset stages of experimental autoimmune encephalomyelitis.* Glia, 2005. **51**(3): p. 235-40.

28. Wu, Q., et al., *MR diffusion changes correlate with ultra-structurally defined axonal degeneration in murine optic nerve.* Neuroimage, 2007. **37**(4): p. 1138-47.

29. Basser, P.J. and C. Pierpaoli, *A simplified method to measure the diffusion tensor from seven MR images.* Magn Reson Med, 1998. **39**(6): p. 928-34.

30. Klein, R.S., et al., *IFN-inducible protein 10/CXC chemokine ligand 10-independent induction of experimental autoimmune encephalomyelitis.* J Immunol, 2004. **172**(1): p. 550-9.

31. Cross, A.H., et al., *Aminoguanidine, an inhibitor of inducible nitric oxide synthase, ameliorates experimental autoimmune encephalomyelitis in SJL mice.* J Clin Invest, 1994. **93**(6): p. 2684-90.

32. Prusky, G.T., et al., *Rapid quantification of adult and developing mouse spatial vision using a virtual optomotor system.* Invest Ophthalmol Vis Sci, 2004. **45**(12): p. 4611-6.

33. Douglas, R.M., et al., *Independent visual threshold measurements in the two eyes of freely moving rats and mice using a virtual-reality optokinetic system.* Vis Neurosci, 2005. **22**(5): p. 677-84.

34. Sun, S.W., et al., *Evolving Wallerian degeneration after transient retinal ischemia in mice characterized by diffusion tensor imaging.* Neuroimage, 2008. **40**(1): p. 1-10.

35. Tu, T.W., et al., *Using absorption-mode images to improve in vivo DTI quality.* Proc. Intl. Soc. Mag. Reson. Med. , 2010. **18, 4001**.

36. Batchelor, P.G., et al., *Anisotropic noise propagation in diffusion tensor MRI sampling schemes.* Magn Reson Med, 2003. **49**(6): p. 1143-51.

37. Song, S.K., et al., *Dysmyelination revealed through MRI as increased radial (but unchanged axial) diffusion of water.* Neuroimage, 2002. **17**(3): p. 1429-36.

38. Song, S.K., et al., *Diffusion tensor imaging detects and differentiates axon and myelin degeneration in mouse optic nerve after retinal ischemia.* Neuroimage, 2003. **20**(3): p. 1714-22.

39. Blewitt, E.S., T. Pogmore, and I.C. Talbot, *Double embedding in agar/paraffin wax as an aid to orientation of mucosal biopsies.* Journal of clinical pathology, 1982. **35**(3): p. 365.

40. Schneider, C.A., W.S. Rasband, and K.W. Eliceiri, *NIH Image to ImageJ: 25 years of image analysis.* Nat Methods, 2012. **9**(7): p. 671-5.

41. Hobom, M., et al., *Mechanisms and time course of neuronal degeneration in experimental autoimmune encephalomyelitis.* Brain Pathol, 2004. **14**(2): p. 148-57.

42. Vellinga, M.M., et al., *Pluriformity of inflammation in multiple sclerosis shown by ultra-small iron oxide particle enhancement.* Brain, 2008. **131**: p. 800-807.

43. Boretius, S., et al., *MRI of optic neuritis in a rat model.* Neuroimage, 2008. **41**(2): p. 323-34.

44. Trip, S.A., et al., *Optic nerve diffusion tensor imaging in optic neuritis.* Neuroimage, 2006. **30**(2): p. 498-505.

45. Chiang, C.W., et al., *Quantifying white matter tract diffusion parameters in the presence of increased extra-fiber cellularity and vasogenic edema.* Neuroimage, under review.

46. Werring, D.J., et al., *Diffusion tensor imaging of lesions and normal-appearing white matter in multiple sclerosis.* Neurology, 1999. **52**(8): p. 1626-32.

47. Tievsky, A.L., T. Ptak, and J. Farkas, *Investigation of apparent diffusion coefficient and diffusion tensor anisotrophy in acute and chronic multiple sclerosis lesions.* AJNR Am J Neuroradiol, 1999. **20**(8): p. 1491-9.

48. Shindler, K.S., et al., *Inflammatory demyelination induces axonal injury and retinal ganglion cell apoptosis in experimental optic neuritis.* Experimental Eye Research, 2008. **87**(3): p. 208-213.

Chapter 5

Conclusions

5.1 Conclusions

Visual dysfunction in multiple sclerosis (MS), commonly the first clinical symptom, is caused by optic neuritis (ON), an inflammation of optic nerve [1, 2]. Thus, functional deficits and structural changes in the visual pathway of ON have been extensively examined [3]. Although various MR techniques have been used to assess inflammation (inflammatory cell infiltration and vasogenic edema) of ON, they rarely demonstrated the ability to image cellularity changes non-invasively [4-7]. This current work has attempted to establish a more accurate measure to assess disease pathologies than the conventional MRI approaches in the hopes of better understanding the disease progression and predicting the various courses of MS.

Neurodegeneration in ON was generally thought to be caused by an inflammatory process of optic nerve, resulting in demyelination and axonal damage, and eventually neuronal loss [8, 9]. Accumulated axonal damage was considered as the major correlate of permanent disability [10]. Therefore, a non-invasive, specific biomarker for inflammation or cellularity may provide a window to reflect disease progression in MS. Our recently developed diffusion basis spectrum imaging (DBSI) approach has shown the capability to assess inflammation, cellularity, axonal injury and demyelination in CNS white matter [11]. Experimental autoimmune encephalomyelitis (EAE), an animal model of MS [3], mimics several MS-like stages and characteristics and thus provides a model to investigate the ON-associated neuropathology in MS.

To demonstrate that our approach accurately reflects inflammation or cellularity, the histological validation is necessary. Therefore, correct and reliable histological staining and quantification protocols are important. As described in Chapter 2, we optimized a set of high quality immunohistochemical staining methods. At the same time, systematic and objective quantification protocols were developed, which are successful in evaluating intact and injured axons, myelin sheaths, and cell nuclei. The histological results by the newly developed protocols are highly reliable.

The impact of CSF partial volume, edema, and inflammation on DTI has been long-recognized; while DBSI enables resolution of these pathologies using a multi-tensor model with multi b-values. In addition, by taking advantage of the coherence of white matter tracts, DBSI allows us to use a reduced diffusion-encoding scheme as applied herein on optic nerve. In Chapter 3, we employed a tissue phantom with 2% agar gel to mimic the condition of vasogenic edema to compare DBSI [11] and conventional DTI [12] measurements. The results showed DBSI provides reliable fiber diffusivity under conditions where DTI fails. A Monte-Carlo simulation considering the impact of edema agrees with the experimental results. The impact of cellularity on DTI and DBSI was further evaluated using simulation as well. Moreover, a 25-direction encoding scheme [13] was successfully applied to generate high quality images of the mouse optic nerve without compromising the accuracy of DBSI analysis.

Finally, Chapter 4 first described the visual acuity (VA) time course of sham and EAE-affected mice where the first sign of decreased VA was detected in EAE and the VA threshold with onset of ON was operationally defined. Second, both DBSI [11] and DTI [12] were performed to assess optic nerve pathologies from EAE and sham mice at onset of ON using the 25-direction diffusion-encoding scheme [13], followed by immunohistochemistry using the developed protocols from Chapter 2. Our results demonstrate that inflammation correlated well with visual impairment in acute EAE ON without retinal atrophy. DBSI successfully detected inflammatory cell infiltration and optic nerve white matter pathology in EAE that was consistent with histology, supporting the capability of DBSI to quantify increased cellularity, axonal injury and myelin damage in the optic nerve of EAE mice.

Overall, the work supports the contention that DBSI provides non-invasive, specific biomarkers of inflammation, cellularity, axonal damage and demyelination in a mouse model of MS by DBSI-derived restricted and non-restricted isotropic diffusion fractions, and axial and radial diffusivity. DBSI can therefore accurately reflect the disease progression.

5.2 References

1. Beck, R.W., et al., *High- and low-risk profiles for the development of multiple sclerosis within 10 years after optic neuritis: experience of the optic neuritis treatment trial.* Arch Ophthalmol, 2003. **121**(7): p. 944-9.

2. Arnold, A.C., *Evolving management of optic neuritis and multiple sclerosis.* Am J Ophthalmol, 2005. **139**(6): p. 1101-8.

3. Gold, R., C. Linington, and H. Lassmann, *Understanding pathogenesis and therapy of multiple sclerosis via animal models: 70 years of merits and culprits in experimental autoimmune encephalomyelitis research.* Brain, 2006. **129**(Pt 8): p. 1953-71.

4. Hickman, S.J., et al., *A serial MRI study following optic nerve mean area in acute optic neuritis.* Brain, 2004. **127**(Pt 11): p. 2498-505.

5. Guy, J., *MRI in experimental inflammatory and mitochondrial optic neuropathies.* NMR Biomed, 2008. **21**(9): p. 968-77.

6. Vellinga, M.M., et al., *Pluriformity of inflammation in multiple sclerosis shown by ultra-small iron oxide particle enhancement.* Brain, 2008. **131**: p. 800-807.

7. Boretius, S., et al., *MRI of optic neuritis in a rat model.* Neuroimage, 2008. **41**(2): p. 323-34.

8. Green, A.J., et al., *Ocular pathology in multiple sclerosis: retinal atrophy and inflammation irrespective of disease duration.* Brain, 2010. **133**(Pt 6): p. 1591-601.

9. Shindler, K.S., et al., *Inflammatory demyelination induces axonal injury and retinal ganglion cell apoptosis in experimental optic neuritis.* Experimental Eye Research, 2008. **87**(3): p. 208-213.

10. Trapp, B.D., R. Ransohoff, and R. Rudick, *Axonal pathology in multiple sclerosis: relationship to neurologic disability.* Curr Opin Neurol, 1999. **12**(3): p. 295-302.

11. Wang, Y., et al., *Quantification of increased cellularity during inflammatory demyelination.* Brain, 2011. **134**(Pt 12): p. 3590-601.

12. Basser, P.J. and C. Pierpaoli, *A simplified method to measure the diffusion tensor from seven MR images.* Magn Reson Med, 1998. **39**(6): p. 928-34.

13. Batchelor, P.G., et al., *Anisotropic noise propagation in diffusion tensor MRI sampling schemes.* Magn Reson Med, 2003. **49**(6): p. 1143-51.

Appendix

(Reprints from the annual Proceedings of the International Society of Magnetic Resonance in Medicine and a published paper)

Infarct volume determined by acute ADC correlates neurological outcome in stroke mice

C-W. Chiang[1], T-H. Wu[2], J. H. Kim[2], and S-K. Song[2]

[1]Chemistry, Washington University, St. Louis, MO, United States, [2]Radiology, Washington University, St. Louis, MO, United States

Introduction

Rodent models have been employed to study human stroke, the third leading cause of death and disability in western countries. In vivo magnetic resonance (MR) imaging including advanced diffusion technology has been employed to examine infracted tissues after stroke[1]. The decreased apparent diffusion coefficient (ADC) has been demonstrated as a sensitive and reliable biomarker of cerebral ischemia[2-3]. In addition, there have been efforts to correlate MR findings with neurological behavior outcomes. Various behavior assessments have been employed including neurological scoring system[4], rotor rod[5], and methamphetamine-induced rotation test[5]. However, an accurate behavior test avoiding subjective ratings, significant training effect, or injection of medicine is still needed. Footprint analysis is a simple and sensitive measurement for gait analysis and has been applied to objectively evaluate the step cycle of mice[6,7]. In this study, the gait analysis of middle cerebral artery occlusion (MCAO) mice was performed using a treadmill to examine the effect of lesion severity on neurological function. Acute DTI derived ADC delineated ischemic lesion clearly enabling quantification of the lesion volume and lesion ADC. The ADC defined lesion volume correlated well with injury severity, and neurological motor function.

Methods

Eighteen male, 8 – 12 weeks old, C57BL/6 mice weighing between 20 – 28 g underwent different degrees of stroke injuries (n = 6 for each group) by electrocoagulation of middle cerebral artery at the right side of the mouse brain. The injury severity was regulated by controlling energy of electrocoagulation at 0 (craniotomy), 1.4 (mild), and 1.8 mJ (moderate). *In vivo* DTI was immediately performed on a 4.7 T magnet utilizing a standard spin-echo diffusion-weighted sequence. All images were obtained with acquisition parameters of TR 1.7 sec, TE 50 ms, Δ 25 ms, δ 8 ms, NEX 4, slice thickness 0.5 mm, field-of-view 3.0 cm × 3.0 cm, data matrix 256 × 256 (zero filled to 512 × 512), (Gx,Gy,Gz) = (1,1,0), (1,0,1), (0,1,1), (-1,1,0), (0,-1,1), and (1,0,-1), and b = 0 and 0.768 ms/μm^2. The locomotor function (left foot base) of the mice was assessed using the treadmill with gait analysis software TreadScan^{TM} 2.0 (Clever Sys. Inc., VA, USA). The evaluation was performed at a speed of 15 cm/s without pre-training. The statistical analysis, two sample student *t* test and Person-product linear correlation, was performed with Origin 7.5 SR2 v7.5817 (Origin Lab Co., MA, USA).

Results and Discussion

In acute stage, i.e., at 3 hours after stroke injury, the tensor derived ADC maps clearly revealed the infracted cortex as the hypointense region on ADC maps in stroke mice. The region of interest (ROI) analysis based on the ADC contrast between the infarct and the non-injured cortex was used to quantify the total lesion volume (Fig. 1a). As the energy deposition elevated to increase the injury severity, the infarct volume increased significantly (Fig. 1b). Although there was a statistically significant difference between the stroke mice and the control, the ADC value of the lesion area among the stroke groups were not statistically significantly different (Fig. 1c). The result suggests that the lesion volume determined using the ADC correlated well with the injury severity intended by modulating the deposited coagulation energy.

The left and right foot base, the distance between mid-points of strides of the pairs of feet, was assessed using mouse treadmill as neurological functional measure. Prior to any experimental procedure, there was no foot base difference among all mice as expected. Since we did the surgery on the right side of the mouse brain and the infarct covers the motor and sensory cortex, we expected a neurological deficit to the left side. Indeed, animal with ischemia showed shortened left foot base compared to naïve and craniotomy group. A linear correlation between the volume of acute infarction and left foot base at day 3 is observed (Fig. 2). There was no observable foot base change for right lateral limbs (data not shown).

Conclusion

As previously reported[1-5], *in vivo* diffusion examination of brain tissue sensitively revealed ischemic lesion. Our results indicated that the total ADC determined volume of infarction reflected stroke injury severity better than ADC itself. The acutely quantified infarct volume correlated with the locomotor function deficit assessed using gait analysis of the mouse treadmill.

References

[1] Busch, E. *et al.* Stroke 1998. [2] Yenari, M.A. *et al.* Brain research 1996. [3] Sotak, C. H. NMR Biomed. 2002. [4] Farrm T. D. *et al.* J. Neuroendocrinol. 2008. [5] Yanagisawa D. *et al. J.* Cereb Blood Flow Metab. 2008. [6] Leblond, H. *et al.* J. Neuroscience 2003. [7] Wooley, C. M. *et al.* Muscle Nerve 2005.

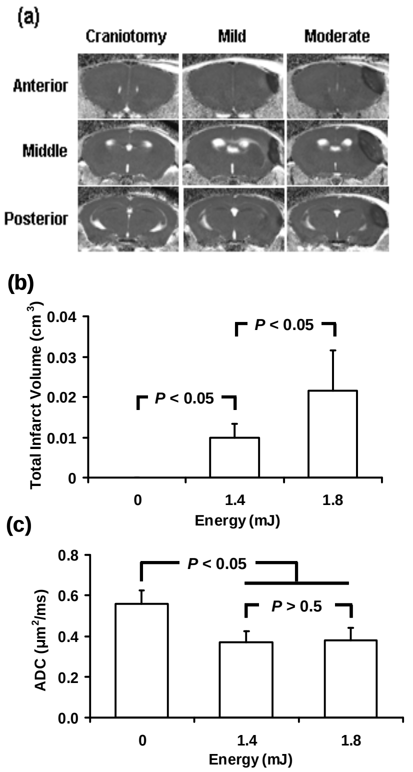

Fig.1 (a) *In vivo* acute DTI derived ADC maps of craniotomy, mild and moderate stroke mice are shown at three different positions: anterior, middle, and posterior of mouse brain. The total infarct volume (b) and its ADC value (c) were quantified. The infarct volume increases rapidly with increase of injury severity while ADC shows no difference between the two injury groups.

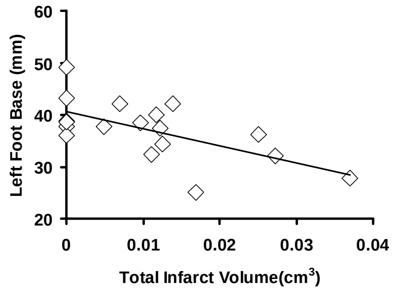

Fig.2 The correlation between total infract volume in acute stage and the locomotor function (left foot base) at 3 days after stroke. The left foot base linearly decreases ($r = -0.64$, $P < 0.05$) with the increase of infarct volume (or severity).

Decreased ADC precedes cellular swelling in N-Methyl-D-Aspartate (NMDA) treated mouse retina

C-W. Chiang[1], J. Chen[2], and S-K. Song[3]
[1]Chemistry, Washington University in St. Louis, Saint Louis, MO, United States, [2]Medicine, Washington University in St. Louis, Saint Louis, MO, United States,
[3]Radiology, Washington University in St. Louis, Saint Louis, MO, United States

Introduction

Acute excitotoxicity causes cytotoxic edema that precedes neuron cell necrosis and apoptosis in neurological diseases[1]. Apparent diffusion coefficient (ADC) decreases early reflecting cytotoxic edema in various brain injuries[2]. Our recent study demonstrated that high-resolution diffusion MRI detected three retinal layers of distinct ADC[3]. In this study, we examined the feasibility of detecting N-methyl-D-aspartate (NMDA) induced retinal excitotoxic injury in mice using *in vivo* diffusion MRI.

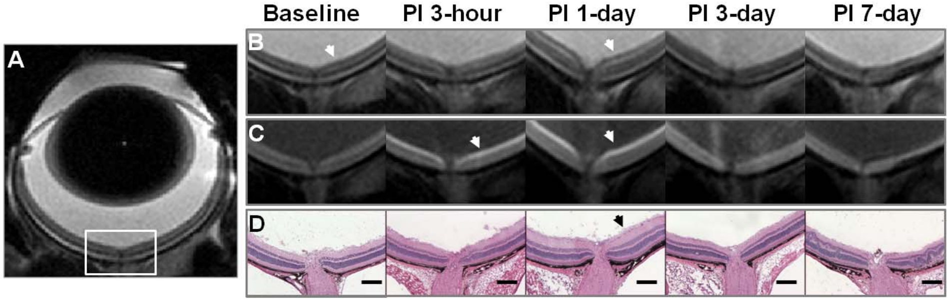

Fig. 1 (A) A representative of non diffusion-weighted image of a normal mouse eye. The highlighted box shows central retina close to the optic nerve head. **(B)** T_2-weighted MR images of mouse retina at baseline and PI 3-hour, 1-, 3-, 7-day. **(C)** Diffusion weighted MR images of the same mouse eyes. **(D)** H&E staining of retina from the same mouse. Scale bar, 200 µm. PI – post injection.

Materials and Methods

Animal Model: Eight-week old male C57BL/6 mice (~25 g) received 0.5 µl of 5 mM NMDA/saline through intravitreal injection. *In vivo* diffusion MRI was performed at 3-hour (n=6), 1- (n=5), 3- (n=3), and 7-day (n=4) post injection (PI). Baseline measurements were performed on age-matched C57BL/6 male mice without NMDA treatment (n=4). *In vivo MRI:* Diffusion weighted imaging (DWI) was performed on 11.74 T utilizing a standard spin-echo diffusion-weighted sequence. Three pairs of diffusion weighted images with orthogonal diffusion weighting directions and opposite gradient polarity and a non-diffusion weighted image were acquired for each mouse eye[3]. MRI acquisition parameters were: TR 2 sec, TE 34 ms, Δ 15 ms, δ 5 ms, b = 0 and 955 s/mm^2, slice thickness 400 µm, FOV 12 × 12 mm^2, in-plain resolution 47 × 47 µm^2 (23 × 23 µm^2 zero filled), and number of average 1. Mice were euthanized at the conclusion of MRI. Eyes were enucleated and snap frozen for histology. *Data Analysis:* Calculation of ADC map and identification of region of interest were performed as previously reported[3]. Starting from the vitreous, the three MR-detected retinal layers were assigned to NFL/GCL/IPL (dark) – INL/OPL (bright) – ONL/IS/OS† (dark). At PI 1-day, there were three, two extra layers resulting from NMDA toxicity, MR-detected layers in the middle and were tentatively assigned as INL/OPL. *Histology:* Eight-µm thick tissue sections bisecting the optic nerve were collected for hematoxylin and eosin (H&E) staining to examine the changes of retinal layers. *Statistics:* One-way ANOVA was performed to test ADC difference between NMDA-treated groups and baseline.

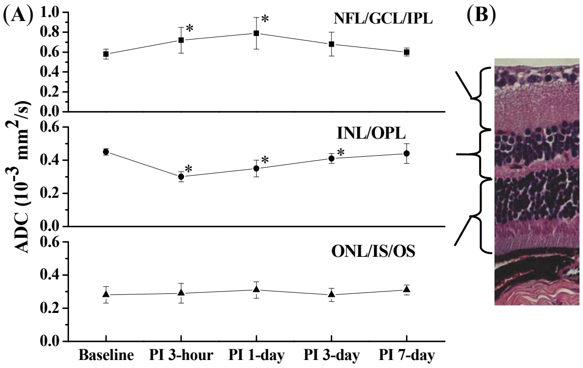

Fig. 2 (A) Diffusion weighted MRI determined ADC in NFL/GCL/IPL, INL/OPL, and ONL/IS/OS of mouse retina at baseline and PI 3-hour, 1-, 3-, and 7-day. (**B**) H&E stained mouse retina shows corresponding retinal cell layers. *, $p < 0.05$ compared to baseline.

Results

Figure 1 shows MR images and the matched H&E staining of mouse retina with or without NMDA treatment. A hyper-intense inner retinal layer between NFL and OPL was seen in DWI as early as at PI 3-hour. At PI 1-day, retinal swelling was evidenced by the increased number of MR-detected middle layers and the increased retinal thickness in H&E staining. At PI 3-day and 7-day, both the inner retinal hyperintensity and retinal swelling subsided, possibly as a result of tissue loss. Figure 2 shows DWI determined ADC in respective MR-detected retinal layers. A transient decrease of ADC in INL/OPL that peaked at PI 3-hour (~30%) was observed. In contrast, ADC in ONL/IS/OS exhibited no change at all times. Additionally, ADC in NFL/GCL/IPL increased at PI 3-hour and 1-day.

Discussion and Conclusion

Intravitreal injection of NMDA caused a transient decrease of ADC in INL/OPL at PI 3-hour, the earliest measurement in our hands, suggesting the excitotoxicity induced edema in these retinal layers[4]. ADC in ONL/IS/OS was not affected by NMDA treatment, reflecting the resistance of pre-synaptic photoreceptors to NMDA excitotoxicity[5]. The transient increase of ADC in NFL/GCL/IPL at PI 3-hour and PI 1-day could be attributed to the acute necrosis of ganglion cells which are sensitive to excitotoxicity[6]. Overall, current results support that decreased ADC as a biomarker of cytotoxic edema providing an early measure of retinal excitotoxicity injury before retinal swelling.

†, Abbreviations of retinal layers: NFL – nerve fiber layer; GCL – ganglion cell layer; IPL – inner plexiform layer; INL – inner nuclear layer; OPL – outer plexiform layer; ONL – outer nuclear layer; IS – inner segment; OS – outer segment.

References

[1] Bonfoco, E. *et al.* PNAS 1995. [2] Moritani, T. *et al.* AJNR 2005. [3] Chen, J. and Wang, Q. *et al.* MRM 2008. [4] Sevick, R. *et al.* Radiology 1992. [5] Lam, T. *et al.* IOVS 1999. [6] Fre´de´ric, L. *et al.* J Neurosci 2009.

Acute visual function impairment in EAE is primarily caused by optic nerve inflammation as assessed by DBSI

Chia-Wen Chiang[1], Yong Wang[2], Tsen-Hsuen Lin[3], Anne Cross[2,4], and Sheng-Kwei Song[2]

[1]*Chemistry, Washington University, St. Louis, MO, United States,* [2]*Radiology, Washington University, St. Louis, MO, United States,* [3]*Physics, Washington University, St. Louis, MO, United States,* [4]*Neurology, Washington University in St. Louis, Saint Louis, MO, United States*

Introduction

Experimental autoimmune encephalomyelitis (EAE) is the main animal model of human multiple sclerosis. Optic neuritis is a commonly seen pathology in EAE mice, and involves inflammation, demyelination, and axonal damage. A prior histological study showed that inflammation precedes retinal ganglion cell death in EAE.[1] Diffusion tensor imaging (DTI) has previously detected axon and myelin injury as decreased axial and increased radial diffusivity, respectively, in chronic EAE optic nerve[2]. In this study, a novel diffusion basis spectrum imaging (DBSI)[3] was performed to evaluate inflamed EAE-affected optic nerves during acute EAE.

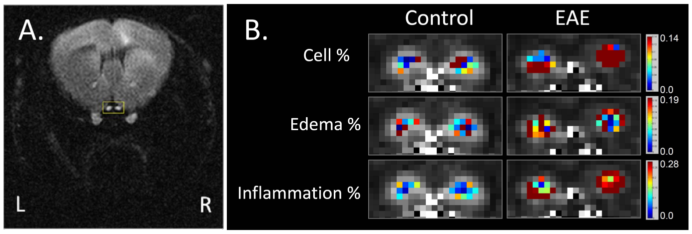

Fig. 1 A representative *in vivo* transverse view diffusion-weighted image of a control mouse brain with optic nerves highlighted (A). Representative DBSI maps of control and EAE optic nerve demonstrating the extent of optic nerve inflammation are presented with color-coded intensity (B).

Materials and Methods

Animal Model: EAE was induced in female, 8 – 10 week old C57BL/6 mice (~20g) by active immunization with MOG$_{35-55}$ peptide/CFA emulsion (n=15). *In vivo* diffusion MRI was immediately performed at the first detection of impaired vision in mice, typically between 9 – 14 days after immunization. Age-matched control mice (n=5) underwent the same procedure without MOG$_{35-55}$ immunization. *In vivo* MRI: DBSI was performed on a 4.7 T magnet utilizing a multi-echo spin-echo diffusion-weighted sequence by multi-directions and multi-*b*-values. All images were obtained with acquisition parameters of TR 1.5 sec, TE 37 ms, Δ 18 ms, δ 6 ms, max. *b*-value 2,200 s/mm^2, slice thickness 0.8 mm, field-of-view 22.5 mm × 22.5 mm, in-plain resolution 117 μm × 117 μm (59 μm × 59 μm zero filled). Functional measurement: Visual acuity (VA) of the individual mouse eye was assessed using Virtual Optomotor System (OptoMotry, Cerebral Mechanics Inc., Canada). Independent left-eye and right-eye vision was measured corresponding to clockwise and counter-clockwise grating movement with adjustable spatial frequency[4]. Baseline VA measurement was assessed to confirm intact vision before EAE immunization. Daily VA measurement was performed to determine EAE optic neuritis onset. Normal mice VA = 0.38 ± 0.03 c /d (mean ± SD). Poor mouse vision was defined as VA≤ 0.25 c/d.

Results

Figure 1(A) shows diffusion-weighted image of control mouse brain with left and right optic nerve (see highlighted box). Figure 1(B) shows representative DBSI maps of cell %, edema %, and inflammation % (equal to cell % + edema %) on control and acute EAE mice with decreased VA. Cell inflammation, edema, and inflammation were clearly seen in acute EAE compared to control mice. Quantified DBSI index and DTI-derived axial and radial diffusivity were shown in Figure 2 and 3. Figure 2 shows all three DBSI index linearly correlates with VA. A strong negative correlation of edema with VA [$R^2 = 0.64$; Figure 2(b)] and inflammation with VA [$R^2 = 0.80$; Figure 2(c)] was seen in acute EAE mice. Figure 3(a) shows that DTI- and DBSI-derived axial diffusivity in EAE mice were each significantly decreased compared with control mice. In contrast, Figure 3(b) shows that DTI- and DBSI-derived radial diffusivity in EAE each significantly increased compared with control mice.

Discussion and Conclusion

Our results indicate that *in vivo* DBSI-derived inflammation% significantly correlated with VA during acute EAE, supporting a predominant role of inflammation at the onset of optic neuritis. The decreased axial diffusivity measured by both DTI and DBSI suggested accompanying axonal injury during acute EAE. Immunohistochemistry is being performed on nerves fixed after MRI to evaluate cell infiltration, axonal injury, and myelin integrity to compare and correlate with our *in vivo* MRI findings.

References

[1] Shindler, K. C. *et al.* Experimental Eye Research 2008. [2] Sun, SW *et a*l. NeuroImage. 2005. [3] Wang, Y *et al.* Brain 2011, in press. [4] Douglas, R.M. *et al*. Visual Neuroscience 2005.

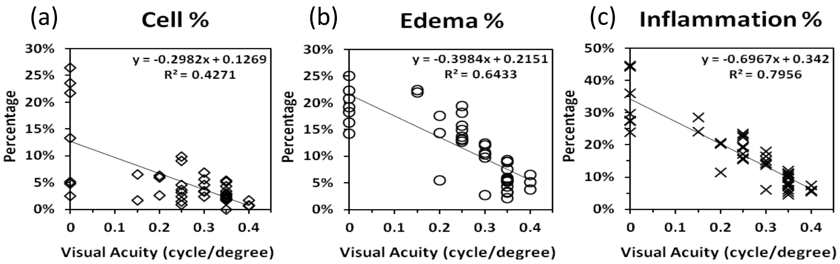

Fig. 2 Correlations between optic nerve DBSI indices and visual acuity (VA) of control (n=5) and acute EAE mice with various degrees of VA impairments (n=15). (a) Cell %, (b) edema %, and (c) inflammation % all negatively linearly correlated with mouse VA. DBSI-based inflammation in optic nerves correlated strongly ($R^2 = 0.80$) with mouse VA, suggesting inflammation is a predominant factor leading to visual function impairment in acute EAE.

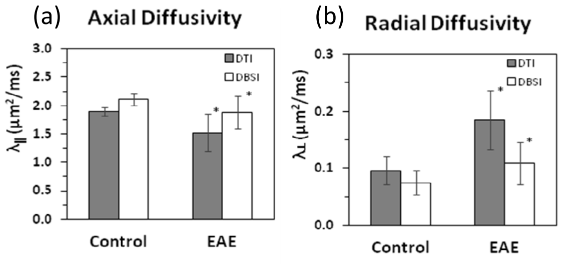

Fig. 3 (a) DTI- and DBSI- derived axial diffusivities in acute EAE decreased by 20% and 13% from the control level. (b) DTI- and DBSI- derived radial diffusivities in acute EAE increased by 80% and 38% from the control level. *, $p < 0.05$ compared to control.

Reduced Diffusion Encoding for Accurately Estimating Axonal Injury, Demyelination, and Inflammation in Mouse Optic Nerve

Chia-Wen Chiang[1], Yong Wang[2], Anne H. Cross[3,4], and Sheng-Kwei Song[2,4]
[1]*Chemistry, Washington University, Saint Louis, MO, United States,* [2]*Radiology, Washington University School of Medicine, Saint Louis, MO, United States,* [3]*Neurology, Washington University School of Medicine, Saint Louis, MO, United States,* [4]*The Hope Center for Neurological Disorders, Washington University School of Medicine, Saint Louis, MO, United States*

Introduction

Diffusion tensor imaging (DTI) has been successfully used to detect axon/myelin dysfunction in white matter injury [1]. However, the Gaussian diffusion assumption hampered its application to quantify non-Gaussian characters. Many new diffusion MRI techniques, such as generalized DTI (gDTI) [2], diffusion spectrum imaging (DSI) [3], diffusion kurtosis imaging (DKI)[4], composite hindered and restricted model of diffusion (CHARMED) [5], have been proposed to model the non-Gaussian diffusion in the past decade. We have recently developed a new diffusion MRI method, diffusion basis spectrum imaging (DBSI), to resolve crossing fibers and quantify confounding effects of inflammation [6]. A 99-direction diffusion-encoding scheme was employed for acquiring DBSI data providing sufficient information to accurately detect and quantify multiple diffusion components including crossing fibers, axonal injury, demyelination, and inflammation in both ex vivo phantom and an in vivo animal model [6]. However, the initial DBSI protocol with 99-direction diffusion weighting scheme leads to a lengthy scanning time. To image small coherent white matter tract such as mouse optic nerve, high spatial resolution and high SNR are required, significantly hampering in vivo DBSI applications. Taking the advantage of the simple structure of optic nerve without crossing fibers, we removed the redundancy in the original 99-direction DBSI diffusion weighting scheme in this study. We demonstrated that a simplified 29-direction DBSI diffusion weighting scheme was adequate to generate DBSI results from mouse optic nerves that were comparable to those obtained using the full 99-direction diffusion-encoding scheme.

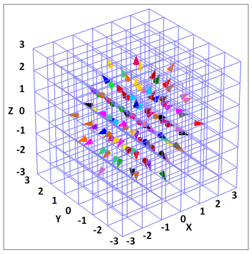

Figure 1 Original 99-direction scheme. Each diffusion-encoding vector starts from the origin of the Cartesian grid system and ends at a non-origin grid point (colored arrows).

Method *99-direction DBSI scheme:* Standard 99 DBSI diffusion-encoding directions can be visualized on a 3D Cartesian grid system (blue boxes in Figure 1). Each diffusion-encoding vector starts from the origin of the Cartesian grid system and ends at a non-origin grid point (colored arrows) including (1) 93 diffusion-encoding vectors located inside the sphere of radius = 3 and (2) 6 diffusion-encoding vectors located at the crossing points between the Cartesian axes and the sphere which constitutes the 99-direction DBSI diffusion-encoding scheme. DBSI diffusion-encoding scheme is the same as the grid scheme used in DSI [3]. However, DBSI only uses the inner part of the DSI grid scheme. The maximal diffusion weighting factor (b-value) of DBSI scheme was 3200 s/mm^2 for ex vivo studies.

Simplified 29-direction DBSI scheme: The simplified 29-direction diffusion weighting scheme (blue arrows with red circles at the tip in Figure 2) was selected and derived from the original 99-direction scheme (blue arrows in Figure 1) by removing symmetric or redundant diffusion-encoding directions while maintaining the diffusion space well sampled and the b-value fully distributed from the range of 0 to 3200 s/mm^2 for ex vivo studies.

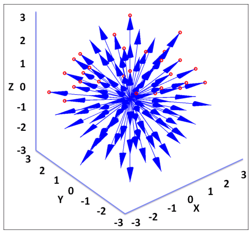

Figure 2 New 29-direction scheme (blue arrows with red marks) is simplified from the 99-direction scheme (blue arrows).

DBSI scan of fixed optic nerves of experimental autoimmune encephalomyelitis (EAE)-affected mice: Five fixed, female EAE-affected C57BL/6 mouse brains with individual paired optic nerves, four mice at acute stage and one at chronic stage with severe pathologies, were examined with both 99- and 29-direction DBSI at the same experimental setup on a 4.7 Tesla scanner using multiple-echo spin-echo sequence [7] with the following parameters: TR 1.2 s, TE 38 ms, Δ 15 ms, δ 5 ms, field-of-view 20 mm × 20 mm, data matrix 256 × 256 (before zero-filled), slice thickness 1 mm, 1 average, and maximal b-value 3200 s/mm^2. Total acquisition time for 99- and 29-direction DBSI was 8 h 25 min and 2 h 30 min respectively. Voxel-based analysis was performed on non-zero filled 99- and 29-direction DBSI data, 50 voxels from 10 optic nerves were used for comparison.

$$S_k = \sum_{i=1}^{N_{Aniso}} S_i e^{-\left|\vec{b}_k\right| \cdot \lambda_\perp} e^{-\left|\vec{b}_k\right| \cdot (\lambda_\parallel - \lambda_\perp) \cos^2\theta_i} + \sum_{j=1}^{N_{iso}} S_j e^{-\left|\vec{b}_k\right| \cdot d_j} \quad [1]$$

DBSI analysis: Eq. [1] was solved by fitting the 99 (or 29) diffusion weighted signals using a linear combination of diffusion basis sets consisting of cylindrically symmetric diffusion tensors [3] with the freedom to vary $\lambda_\parallel$ and $\lambda_\perp$ to estimate the number of anisotropic diffusion tensor components (N_{aniso}) and the associated principal directions. After N_{Aniso} was computed, the number of isotropic component (N_{iso}) was further determined using nonnegative least-squares (NNLS) analysis. The global nonlinear optimization was conducted employing direct pattern search to solve Eq. [1]. S_k is the kth measured diffusion weighted signals (k = 1, 2, 3, …). S_i and S_j are fractions of anisotropic diffusion components and isotropic diffusion component respectively.

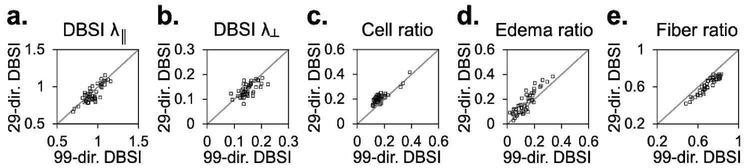

Figure 3 29- and 99-direction DBSI indices distributed close to the line of identity, indicating minor offsets using 29-direction scheme.

Results and Discussion

Scatter plots (Fig. 3 a-e) qualitatively revealed that most data points distributed near the line of identity with small offsets. Bland-Altman analysis (Table 1) quantitatively suggested that 29- and 99-direction DBSI indices were comparable with acceptable standard deviations of the difference and small biases. For the animal tissues demonstrated in this study, the scanning time was reduced by 2/3rds using the simplified 29-direction DBSI compared to the original 99-direction scheme. The same spatial resolution and DBSI computation accuracy was maintained for mouse optic nerves ex vivo. Currently, by employing single-shot diffusion-weighted EPI, 99-direction DBSI with 2 x 2 x 2 mm^3 resolution can be acquired within 15 min on a 3.0 Tesla Trio TIM (Siemens, Erlangen, Germany) human scanner. If the same 2 x 2 x 2 mm^3 resolution is maintained, the simplified 29-direction scheme will shorten the scanning time to 5 minutes.

DBSI Indices		DBSI $\lambda_\parallel$	DBSI $\lambda_\perp$	Cell ratio	Edema ratio	Fiber ratio
Mean (±S.D.)	29-dir.	0.91 (±0.11)	0.14 (±0.03)	0.21 (±0.05)	0.17 (±0.09)	0.62 (±0.09)
	99-dir.	0.94 (±0.10)	0.15 (±0.03)	0.16 (±0.05)	0.13 (±0.07)	0.70 (±0.09)
29-dir. vs. 99-dir.	Bias[1]	-0.04	-0.01	0.04	0.04	-0.08
	Precision[2]	0.06	0.02	0.03	0.04	0.03

[1] Bias = average difference of Bland-Altman plot of 29- minus 99-direction DBSI against mean;
[2] Precision = 1 S.D. of difference; directional diffusivity in μm^2/ms.

Table 1 Quantitative Bland-Altman analysis of the simplified 29- and original 99-direction DBSI, indicating good agreement between the two schemes.

References [1] Song, SK. *et al. Neuroimage* 2002; 17:1429 . [2] Chunlei L. *et al. MRM* 2004; 51:924–937; [3] Wedeen, VJ. *et al. Neuroimage* 2008; 41: 1267-77; [4] Fieremans, E. *et al. Neuroimage* 2011; 58:177-188; [5] Assaf,Y. *et al. Neuroimage* 2005; 27: 48-58; [6] Wang,Y. *et al. Brain* 2011, 134:3590; [7] Tu TW. *et al. Proc. Intl. Soc. Magn. Reson. Med.* 18 (2010), 4001.

Cell Swelling Contributes to Thickening of Low-Dose N-methyl-D-Aspartate–Induced Retinal Edema

Junjie Chen,[1,4] *Chia-Wen Chiang,*[2,4] *Huiying Zhang,*[1] *and Sheng-Kwei Song*[3]

Purpose. The contribution of cell swelling versus vascular leakage in retinal edema remains largely undefined. The objective of this study was to use in vivo magnetic resonance imaging (MRI) to assess retinal cell swelling in the edematous mouse retina.

Methods. Inner retinal edema was induced by intravitreal injection of 2.5 nmol N-methyl-D-aspartate (NMDA). To assess retinal cell swelling, diffusion MRI was performed at baseline, 3-hours, 1 day, 3 days, and 7 days ($n \geq 5$ at each time point) after NMDA injection. To detect retinal vascular leakage, gadolinium diethylenetriamine pentaacetic acid (Gd-DTPA) enhanced MRI was performed at baseline, 3 hours and 1 day ($n = 5$ for each group) after NMDA injection. Upon the completion of MRI, mouse eyes were enucleated, cryosectioned, and stained for assessing retinal layer thickness and cell death.

Results. Inner retinal cell swelling was hyperintense on diffusion-weighted images at 3 hours and 1 day after NMDA injection. The thickened inner retina was also seen in anatomic MRI and histology. Quantitatively, inner retinal apparent diffusion coefficient (ADC) decreased approximately 20% at 3 hours and 1 day after NMDA injection ($P < 0.05$ compared with baseline), suggesting cell swelling. Systematic injection of paramagnetic Gd-DTPA did not alter vitreous longitudinal relaxation time (T1) at baseline or at 3 hours after NMDA injection. In contrast, vitreous T1 in mice decreased 16 ± 6% ($P < 0.05$), reflecting retinal vascular leakage at 1 day after NMDA injection.

Conclusions. Noninvasive diffusion MRI was performed to detect retinal cell swelling in vivo. Our results demonstrated that retinal cell swelling could directly lead to retinal thickening independent of vascular leakage. (*Invest Ophthalmol Vis Sci.* 2012;53:2777–2785) DOI:10.1167/iovs.11-8827

Retinal edema impairs vision in millions. It is diagnosed as abnormal thickening of the retina that is commonly observed in ischemic and inflammatory diseases.[1–4] Retina edema can be classified as cytotoxic or vasogenic, which respectively reflects cell swelling induced by volumetric increase of *intracellular* water and vascular leakage induced volumetric increase of *extracellular* water.[5] It is commonly accepted that vascular leakage is the primary pathway of retinal edema. However, in ischemic/excitotoxic diseases cell swelling may develop early or coexist with vascular leakage.[6,7] It has also been suggested that the swelling and death of Müller cells contributes to the development of cystoid macular edema.[4] Thus, cell swelling and vascular leakage may have different contributions to retinal edema in individual patients.

Noninvasive methods for direct assessment of retinal cell swelling are lacking. Unlike vascular leakage induced edema that can be indirectly detected using fluorescein angiography,[2,8] retinal cell swelling can be implicated only in certain patients who develop retinal thickening without vascular leakage.[9] Given the different mechanisms underlying cytotoxic and vasogenic edema, the capability to differentially assess retinal cell swelling and vascular leakage is therefore critical to advance the current disease diagnosis and therapy.

In addition to its detectability, the contribution of cell swelling to edematous retinal thickening remains an open question. Knowledge acquired from cerebral diseases suggested that cell swelling may not lead to increased tissue volume if the blood–tissue barrier, which limits extravasation of blood-pool water, is intact.[10] Instead, cell swelling can develop through redistribution of extracellular water, accompanying the ion (primarily Na^+) flux, into the intracellular compartment.[10] Since the neural retina comprises a blood–retina barrier, if the same mechanism applies, cell swelling may not lead to retinal thickening before the onset of retinal vascular leakage.

We hypothesize that retinal cell swelling directly causes retinal thickening. The retina is a thin layer of tissue (200–300 µm thick) located adjacent to vitreous (99% of water content).[11] It continuously experiences a transretinal fluid flux driven by intraocular pressure gradient from the vitreous to the choroid.[5] This unrestricted extracellular fluid supply suggests retinal cell swelling may develop without changing the extracellular water volume. A mouse model of N-methyl-D-aspartate (NMDA) excitotoxicity was used to test our hypothesis. Excessive binding of intravitreally injected NMDA to NMDA receptors causes overexcitation of neuronal cells followed by energy failure. The resulting cell swelling and edematous retinal thickening occur within several hours.[12] Due to the absence of NMDA receptors on photoreceptor cells in the outer retina, NMDA excitotoxicity primarily damages the inner retina that extends from the nerve fiber layer to the outer plexiform layer.

In this study, diffusion MRI–derived water apparent diffusion coefficient (ADC) was measured to evaluate NMDA excitotoxicity–induced cell swelling in the inner and outer

---

From the [1]Department of Medicine, the [2]Department of Chemistry, and the [3]Department of Radiology and Hope Center for Neurological Disorders, Washington University, St. Louis, Missouri.

[4]These authors contributed equally to the work presented here and should therefore be regarded as equivalent authors.

Supported in part by National Institutes of Health Grants R21 EY018914 (JC) and NIH P01 NS059560 (SKS), Washington University Diabetes Research and Training Center Pilot and Feasibility Grant 5 P60 DK20579 (JC), and Missouri Life Science Research Board Pilot Grant 091076 (JC).

Submitted for publication October 19, 2011; revised February 24, 2012; accepted March 15, 2012.

Disclosure: **J. Chen**, None; **C.-W. Chiang**, None; **H. Zhang**, None; **S.-K. Song**, None

Corresponding author: Sheng-Kwei "Victor" Song, Biomedical MR Laboratory, Campus Box 8227, Washington University School of Medicine, Room 2313, 4525 Scott Ave., St. Louis, MO 63110; ssong@wustl.edu.

retina. Diffusion MRI is a primary clinical imaging method for assessing neural tissue injury.[13] Despite the retinal edema-induced concomitant T1 and T2 changes during the diffusion-weighted MRI measurement, the derivation of ADC takes the ratio of image intensities with and without diffusion weighting, which essentially performed the automatic normalization of T1 and T2 effects eliminating the commonly seen "T2 shine through" effect in diffusion-weighted images.[13] The measured ADC is by nature independent of T1 relaxation, T2 relaxation, or the magnetic field strength.[14,15] It has long been recognized that neuronal cell swelling leads to an ADC decrease.[16,17] When cell swelling and vasogenic edema coexist, such as that observed in ischemia/reperfusion injury,[18,19] the relative contribution of each component at different stages of the disease confounds the interpretation of the longitudinal evolution of ADC.

Gadolinium diethylenetriamine pentaacetic acid (Gd-DTPA) enhanced MRI with T1 mapping was used in this study to evaluate retinal vascular leakage before, at 3 hours, and 1 day after NMDA treatment. Gadolinium is a paramagnetic ion that reduces ^{1}H T1 of surrounding water molecules. The chelated Gd-DTPA has limited permeability through intact blood–brain barrier or blood–retina barrier. In CNS diseases such as multiple sclerosis (MS), the Gd-DTPA from the blood pool into perivascular tissue through the damaged blood–brain barrier in active lesions results in signal enhancement on T1-weighted images.[20–22] The sensitivity of this technique to MS lesions is improved by administering a higher dose of Gd-DTPA and delayed image acquisition[23,24]; for example, it reached a 95% detection rate for MS lesions when MR images were acquired at 20 minutes after a triple dose (0.3 mmol/kg) of Gd-DTPA.[24] In retinal diseases such as diabetic retinopathy[25] and macular edema,[26] the leakage of Gd-DTPA into avascular posterior vitreous caused local enhancement of the T1-weighted signal. The Gd-DTPA–enhanced MRI-detected retinal vascular leakage was confirmed by histology[27] or electron microscopy.[28] Our recent work showed that retinal vascular leakage in *rd1* mice resulted in a progressive increase of vitreous signal within the first 30 minutes after injection of 1.0 mmol/kg Gd-DTPA.[29] Unfortunately, the exact sensitivity of this MRI technique to retinal vascular leakage, as compared with standard fluorescein angiography and histological methods, has not been defined yet. Based on the previous work of our group and others, we used a high dose of Gd-DTPA (1.0 mmol/kg, 10-folds the standard dose) and delayed image acquisition (between 30 and 45 minutes after Gd-DTPA injection) to optimize MRI sensitivity against retinal vascular leakage.

METHODS

NMDA Animal Model

All animal experiments were performed according to protocols approved by the Animal Studies Committee at Washington University and were in adherence to the ARVO Statement for the Use of Animals in Ophthalmic and Vision Research.

A total of 71 3- to 4-month-old male C57BL/6 mice were used. Normal mice ($n = 5$) were used to determine the baseline parameters. Other mice were intravitreally injected with 0.5 µL of 5 mM (equivalent to 2.5 nmol) NMDA or sham-injected with 0.5 µL of saline. Diffusion MRI was performed at 3 hours ($n = 8$ for NMDA group vs. 5 for sham group), 1 day ($n = 8$ vs. 7), 3 days ($n = 8$ vs. 5) or 7 days ($n = 5$ vs. 5) after intravitreal injection. A separate group of mice was used to assess the development of NMDA excitotoxicity–induced retinal vascular leakage. The differences in vitreous longitudinal relaxation time (T1) after Gd-DTPA injection in normal mice ($n = 5$), and in mice at 3 hours ($n = 5$), and 1 day ($n = 5$) after NMDA injection were examined.

Intravitreal Injection Protocol

Intravitreal injection was performed according to reported procedures with some modifications.[30] Mice were anesthetized by inhalation of 1.5–3% isoflurane mixed with oxygen. A drop of topical antibiotics was applied to the left eye. A 34-gauge sharp needle was inserted into the posterior vitreous (1.5 mm depth) at approximately 1 mm posterior to the limbus. The other end of the needle was connected to a microinjection pump (World Precision Instruments, Sarasota, FL). A total of 0.5 µL 5 mM (equivalent to 2.5 nmol) NMDA or saline was injected into the vitreous within 15 seconds. The needle was kept in the vitreous for 1 extra minute and then was slowly pulled out. Finally, a drop of antibiotic gel was applied to the left eye.

The injection volume was selected to avoid distortion of the globe that was frequently observed after injection of >1 µL fluid. The 0.5 µL fluid occupied approximately 10% of mouse vitreous volume (4.3 ± 0.6 µL, $n = 6$) as determined by MRI (voxel size $= 100 \times 100 \times 100$ µm^3 or 1 nL; Kaplan HJ, et al. *IOVS* 2010;43:ARVO E-Abstract 4414).

MRI

MRI was performed on a commercial MRI system scanner (Varian 11.74T UNITY-INOVA spectrometer/scanner; Varian Associates, Palo Alto, CA) using our previously reported procedure. Mice were anesthetized by intraperitoneal injection of ketamine (87 mg/kg) and xylazine (13 mg/kg) followed by constant subcutaneous infusion of ketamine (54 mg/kg/h)/xylazine (4 mg/kg/h). Animal body temperature was maintained at 37°C and its respiration was monitored using a small animal heating and monitoring system (SA Instruments, Stony Brook, NY). An active-decoupled saddle volume coil was used for radiofrequency (RF) transmission. An actively decoupled surface coil (diameter = 1 cm) was placed on top of the left eye for receiving the MR signal. All images were acquired on a nasal–temporal slice that bisects the eye through the optic nerve head.

Diffusion MRI was used to assess NMDA excitotoxicity–induced retinal cell injury. Three orthogonal diffusion gradients were applied in directions parallel to and in- and out-of-plane perpendicular to the axis of the optic nerve. In each direction, a pair of diffusion-weighted images was acquired with positive and negative diffusion gradients to minimize the background magnetic field gradient effect on the diffusion measurement. Acquisition parameters were: slice thickness 400 µm; field-of-view 12×12 mm^2; data matrix 256×256 (zero filled to 512×512); in-plane resolution 47×47 µm^2; number of averages 1; repetition time (TR) 2.0 s; echo time (TE) 34 ms; diffusion gradient on time (δ) 5 ms; duration time between two diffusion gradients (Δ) 15 ms; b-values 0 and 954 s/mm^2; acquisition time 1 hour.

Gd-DTPA–enhanced MRI was used to assess the development of retinal vascular leakage in NMDA-injected mice. Two sets of T1-weighted images of mouse eye were acquired before and 30 minutes after a bolus injection of Gd-DTPA (1 mmol/kg) through an intraperitoneal catheter. Acquisition parameters were: slice thickness 400 µm; field-of-view 6×6 mm^2; data matrix 32×64 (the resolution was higher in the direction parallel to the optic nerve, zero filled to 64×64); in-plane resolution 188×94 µm^2; TR (number of averages) 0.3 s (8), 0.8 s (4), 2.0 s (2), 6.0 s (1), 16.0 s (1); TE 16 ms; acquisition time 17 minutes.

All animals underwent a single diffusion or Gd-DTPA–enhanced MRI measurement. Upon the conclusion of MRI, mice were euthanized and eyes were enucleated for histology.

MR Data Analysis

Diffusion-weighted and T1-weighted MR images were processed using previously described methods to determine ADC and T1 maps of the mouse eye.[31]

NMDA-induced cell injury in the inner and outer retina was assessed using ADC. Segmentation of the inner and outer retina was performed following a previously described procedure with minor

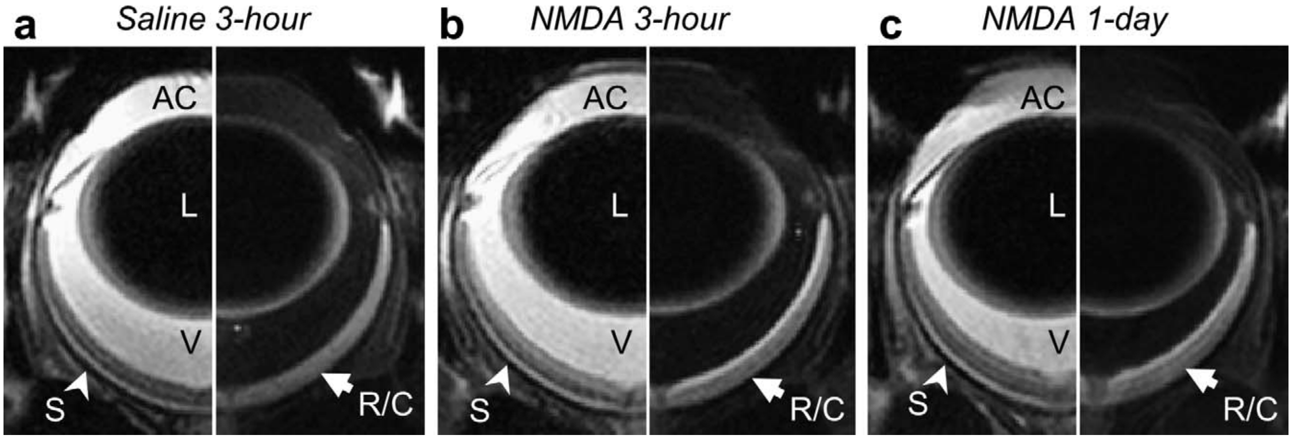

FIGURE 1. Representative nondiffusion-weighted (*left*) and diffusion-weighted (*right*) MR images of mouse eyes at 3 hours after saline injection (**a**), or at 3 hours (**b**) and 1 day (**c**) after NMDA injection. On nondiffusion-weighted images, the anterior chamber (AC), lens (L), vitreous (V), and sclera (S) are clearly identified. Retina/choroid layers (R/C) were bright on diffusion weighting and exhibited multiple signal intensity layers on nondiffusion-weighted images. At 3 hours and 1 day after intravitreal injection of NMDA, a hyperintense inner retina layer appeared in diffusion-weighted images, reflecting decreased diffusivity. On nondiffusion images of the same mouse eyes, more MR-detected layers in retina are visually discernible.

adjustments (see Figs. 3a and 3b in the following text).[31] First, the retina and choroid layers were identified by the hyperintense signal on diffusion-weighted images. The retina and choroid were determined as the region with signal > mean ± 3SD of vitreous and sclera signal. Second, the choroid was manually segmented on nondiffusion-weighted images as the outermost hyperintense layer of the retina/choroid layers. The remaining tissue was considered as the MRI-detected retina. Finally, the outermost hypointense retinal layer on nondiffusion-weighted images was manually segmented and assigned as the outer retina that comprises photoreceptor cell nuclei, inner and outer segments. All other MRI-detected retinal layers were assigned to the inner retina that extends from the nerve fiber layer to the outer plexiform layer. Due to the absence of MR signal contrast at the peripheral retina, we used our previously reported protocol to define the region-of-interest (ROI) analyzing retinal ADC.[31] Specifically, two central retinal segments, located between 250 and 750 μm away from the optic nerve head, were used to determine the mean retinal ADC. The MRI-determined inner and outer retinal thickness was estimated as the mean thickness in the two segments.

To quantify vitreous T1 on the calculated T1-map, the ROI covering the entire vitreous space was defined. The mean T1 in this ROI was used for interanimal data comparison.

Histology

Eyes were enucleated, flash-frozen, and sectioned (8 μm thick). Tissue sections were stained with hematoxylin and eosin (H&E) for analysis of the retinal thickness and cell loss, and stained with terminal deoxynucleotidyl transferase dUTP nick-end labeling (TUNEL) for analysis of cell apoptosis. Only those sections cut through the optic nerve head and perpendicular to the retina were selected for data analysis. The thickness of the inner and outer retina on H&E–stained slices was measured in the central retina region corresponding to that used for ADC analysis. Because sporadic tissue loss had occurred during the TUNEL staining preparation, the exactly identical ROI for

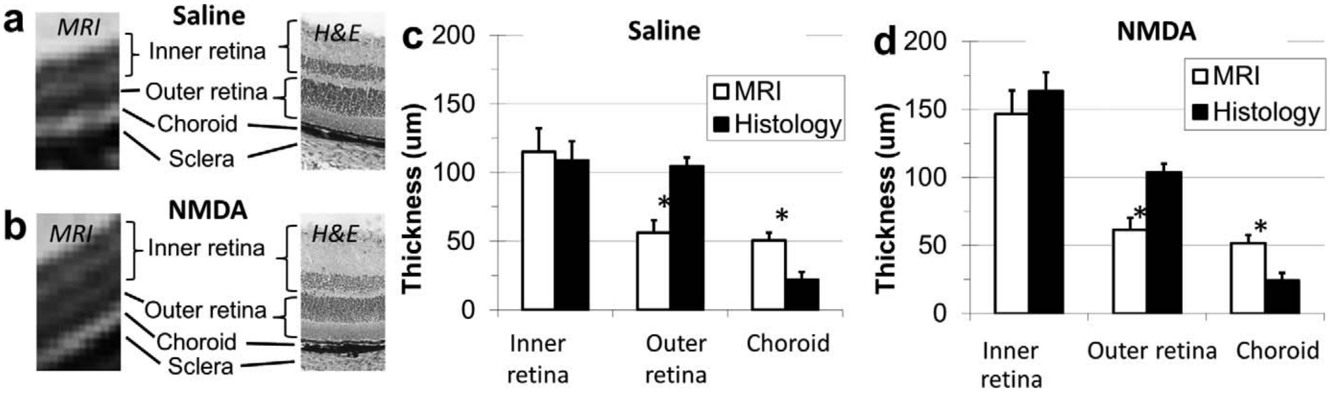

FIGURE 2. Assignment of MR-detected retinal cell layers based on the MRI and histology-measured layer thickness. The R/C layers on nondiffusion-weighted images (*left*) and the corresponding regions on H&E–stained retinal sections (*right*) in mice at 1 day after saline (**a**) and NMDA (**b**) injection are shown. The bright layer adjacent to the sclera was assigned to the choroid. The dark retinal layer adjacent to the choroid was assigned to the outer retina. The remaining retinal layers, four in mice at 3 hours and 1 day after NMDA injection and two in all other mice, were assigned to the inner retina. MRI and histology-quantified thickness of retinal layers and the choroid after saline (**c**) or NMDA (**d**) injection is shown. Each data point represents the average of mice at 3 hours and 1 day after injection. Compared with histology, MRI detected similar inner retinal thickness, underestimated the outer retinal thickness, and overestimated the choroid thickness in all mice. *$P < 0.05$ compared with histology-determined layer thickness. Data were presented as mean ± SD. NFL, nerve fiber layer; GCL, ganglion cell layer; IPL, inner plexiform layer; INL, inner nuclear layer; OPL, outer plexiform layer; ONL, outer nuclear layer of photoreceptor cells; IS/OS, inner and outer segments of photoreceptor cells; RPE, retinal pigment epithelium.

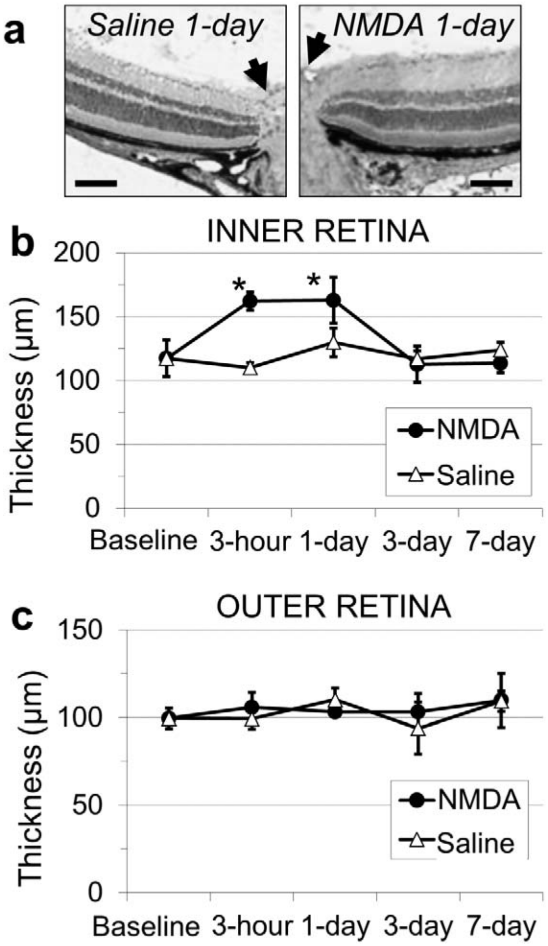

Figure 3. Histology-determined inner and outer retina thickness of normal and NMDA-injured mice. H&E–stained retinal sections of mice at 1 day after saline or NMDA injection (**a**) show substantially increased retina thickness in NMDA-treated mice. *Arrows* indicate the optic nerve head. Scale bar: 100 µm. Quantitative measurements showed increased inner retinal thickness at 3 hours and 1 day after NMDA injection (**b**). The outer retinal thickness remained unchanged in all mice (**c**). $^*P < 0.05$ compared with saline-injected mice at the same time point and normal mice at baseline. Data were presented as mean ± SD.

ADC and thickness measurement by MRI could not be obtained without encountering tissue voids by histology. Thus, four 200-µm-wide central retinal segments from two adjacent frozen-tissue sections, a subregion representing the largest area allowing a consistent localization among tissues within the MRI analysis region, were used for counting necrotic or apoptotic cells.

Statistics

All statistical analyses were performed using commercial software (SAS software; SAS Institute, Cary, NC). Quantitative data are expressed as mean ± SD. For comparisons between two experimental groups, the significance of the difference between the means was calculated.

Two-way ANOVA was used to test the difference of: (1) the inner or outer retinal ADC for NMDA- versus saline-injected mice at different time points; (2) the inner or outer retinal thickness for NMDA- versus saline-injected mice at different time points; and (3) the number of necrotic or apoptotic cells among different retinal nuclear layers at different time points. One-way ANOVA was used to test the difference of Gd-DTPA–induced T1 shortening among normal mice, NMDA-injected mice at 3 hours, and NMDA-injected mice at 1 day. When overall significance of $P < 0.05$ was attained by ANOVA, comparisons between the means were performed using the Freeman–Tukey test. Paired Student's *t*-test was used to test the difference of vitreous T1 before and after Gd-DTPA treatment. A statistically significant difference was defined by $P < 0.05$.

RESULTS

MRI Detected Abnormal Inner Retinal Signal at 3 Hours and 1 Day after NMDA Injection

Figure 1 shows representative diffusion- and nondiffusion-weighted MR images of mouse eyes. In nondiffusion-weighted images, three MR signal intensity defined layers were seen in the retina of normal mice (Figs. 1a, 2a). Both lens and sclera appeared dark. In contrast, the anterior chamber and vitreous were bright. In diffusion-weighted images (b-value = 954 s/mm^2), the vitreous and anterior chambers were nearly invisible because of fast water diffusion in these compartments. The retina/choroid layers appeared bright because of restricted water diffusion in these tissues.

At 3 hours and 1 day after NMDA injection, diffusion-weighted images detected abnormal hyperintense signal in the inner retina, suggestive of reduced water diffusivity. Nondiffusion-weighted images showed two more MR-detected retinal layers in NMDA-treated mice than that in saline-injected mice, indicating retinal thickening (Figs. 1b, 1c, 2b).

Inner Retinal Thickness Transiently Increased at 3 Hours and 1 Day after NMDA Injection

Figures 2a and 2b show the assignment of MRI-detected retinal/choroid layers using MRI and histology-measured retinal thickness. Based on our previous reports,[29,31,32] the outmost MR-detected retina/choroid layer, that is, the bright layer adjacent to sclera, was assigned as the choroid. The layer adjacent to the choroid was assigned as outer retinal photoreceptor cells comprising the outer nuclear layer and the inner and outer segments. The remaining MRI-detected layers were assigned as the inner retina. The assigned inner retina was confirmed by the comparable MRI and histology-determined inner retinal thickness in both saline- and NMDA-treated mice (Figs. 2c, 2d). The thickness of the MRI-detected outer retina was underestimated due to the partial volume-effect–induced overestimation of the thickness of MRI-detected choroid.[31]

Histological analysis showed NMDA injection acutely caused an approximately 50% increase of inner retinal thickness, reaching 170 ± 17 µm at 3 hours and 163 ± 16 µm at 1 day ($P < 0.05$ compared with saline-injected mice). From 3 days after NMDA injection, the inner retinal thickness recovered to its normal value of 115 ± 15 µm (Figs. 3a, 3b). The outer retinal thickness remained unchanged at all time points after NMDA injection (Fig. 3c).

Inner Retinal ADC Transiently Decreased at 3 Hours and 1 Day after NMDA Injection

Figure 4 shows diffusion MRI quantified inner and outer retinal ADC. The inner retinal ADC was 0.51 ± 0.07 µm^2/ms at baseline. After NMDA injection, the inner retinal ADC decreased by approximately 20%, reducing to 0.40 ± 0.02 µm^2/ms at 3 hours and 0.39 ± 0.05 µm^2/ms at 1 day. From 3 days after NMDA injection, the inner retinal ADC recovered to baseline values. In contrast, the outer retinal ADC remained unchanged after NMDA injection. In saline-injected mice, both

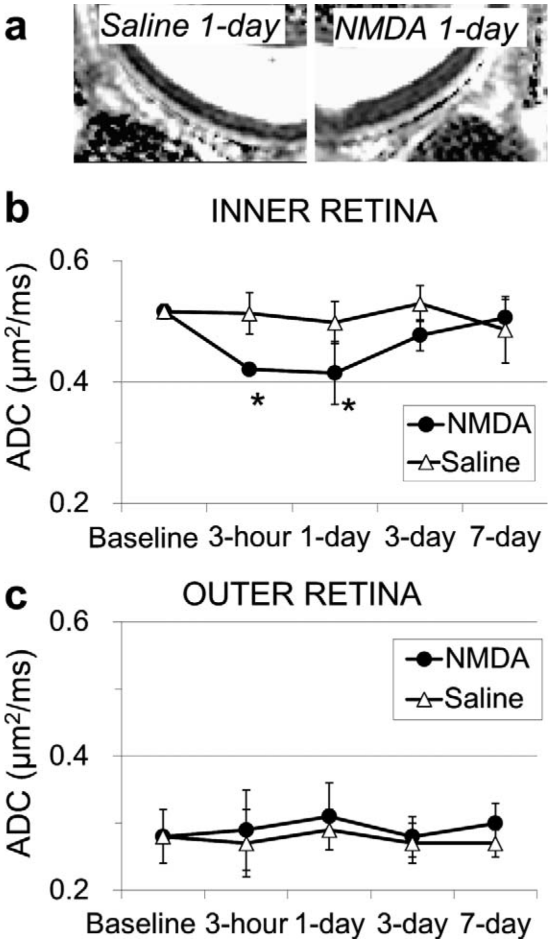

Figure 4. Diffusion MRI determined inner and outer retinal ADC of normal and NMDA-injured mice. Representative ADC maps of mouse retina at 1 day after saline or NMDA injection were shown (**a**). The inner retinal ADC transiently reduced in mice at 3 hours and 1 day after NMDA injection (**b**); the outer retinal ADC remained unchanged after NMDA injection (**c**). $^{*}P < 0.05$ compared with saline-injected mice. Data were presented as mean ± SD.

inner and outer retinal ADC remained unchanged at all time points.

Retinal Vascular Leakage Was Observed at 1 Day, but Not at 3 Hours, after NMDA Injection

Retinal vascular leakage was evaluated by Gd-DTPA–enhanced MRI (Fig. 5). Gd-DTPA treatment did not cause significant changes of the vitreous T1 in normal mice ($-0 \pm 4\%$) or mice at 3 hours after NMDA injection ($-4 \pm 3\%$). However, in mice at 1 day after NMDA injection, Gd-DTPA treatment changed the vitreous T1 by $-16 \pm 6\%$ ($P < 0.05$ compared with before Gd-DTPA treatment) due to leakage of Gd-DTPA into the avascular vitreous.[25]

NMDA Excitotoxicity Causes Inner Retinal Cell Necrosis and Swelling

Excitotoxicity-induced inner retinal cell swelling was reflected by the ensuing retinal cell necrosis on H&E–stained slides (Fig. 6a). The number of necrotic cells peaked at 3 hours and 1 day after NMDA injection, then rapidly decreased close to zero from 3 to 7 days (Fig. 6b). No necrotic cell was observed in the outer retina of NMDA-treated mice or in the entire retina of normal and saline-injected mice.

Retinal cell apoptosis was assessed by TUNEL staining. As early as 3 hours after NMDA injection, TUNEL-positive apoptotic cells were observed in the inner retina (Fig. 6c). The number of apoptotic cells peaked at 1 day and decreased close to zero at 3 and 7 days (Fig. 6d). Sporadic apoptotic cells were detected in the outer retinal photoreceptor cells of NMDA-treated mice, which agreed with previous reports.[33,34] No apoptotic cells were detected in the retina of normal and saline-injected mice.

Discussion

Our results demonstrated the capability of in vivo diffusion MRI to noninvasively assess retinal cell swelling in the NMDA mouse model. The cytotoxic retinal edema induced by intravitreal injection of NMDA resulted in transient inner retinal thickening and ADC decrease. Inner retinal thickening with ADC decrease was observed at 3 hours after NMDA injection, prior to retinal vascular leakage. This decreased ADC was not masked by the potential presence of vasogenic edema resulting from the onset of vascular leakage at 1 day after NMDA injection. Thus, our finding suggests that retinal cell swelling, unlike its cerebral counterpart, can directly cause retinal thickening independent of retinal vascular leakage.

The NMDA mouse model was selected in this study to take advantage of NMDA excitotoxicity-induced layer-specific injury in the inner retina.[12] Specifically, intravitreal injection of NMDA acutely causes the overexcitation of inner retinal neuronal cells due to its excessive binding to NMDA receptors. Müller cell swelling may also occur due to intracellular overloading of K^+ and glutamate that are released by overexcited neuronal cells.[35] However, outer retinal photoreceptor cells that do not express NMDA receptors, as well as retinal vasculature that comprises nonexcitable cells, are not directly affected by NMDA.[36] Thus, the NMDA mouse model is ideal to evaluate contribution of cell swelling to edematous retinal thickening.

The present study is the first in vivo investigation of layer-specific retinal cell swelling using diffusion MRI. The image resolution used (47 × 47 μm) is among the highest resolution reported in the literature.[29,31,37] Although five pixels across the 200-μm-thick retina could not resolve individual retinal anatomic layers (Figs. 2a, 2b), our results showed that it is sufficient to differentially detect inner retinal cell swelling from the outer retina in vivo. Using the same imaging parameters (e.g., TR and TE) as those used in our previous report,[31] the observed inner and outer retinal ADC in normal mice were consistent between the two studies.[31] In NMDA-injured mice, an approximately 20% decrease of inner retinal ADC was detected at 3 hours and 1 day after NMDA injection, reflecting the acute development of cell swelling in the inner retina. In agreement with MRI findings, histology analysis showed that the inner retinal cell necrosis, which typically developed after cell swelling,[38] also peaked at 3 hours and 1 day after NMDA injection. In the outer retina, however, no substantial change in MRI-determined ADC or histology-delineated cell viability was observed after NMDA injection. Thus, our results demonstrated that diffusion MRI may be used to detect layer-specific retinal injury in vivo.

Retinal vascular leakage was assessed by Gd-DTPA–enhanced MRI. Gadolinium ion, Gd^{3+}, is paramagnetic, which reduces the T1 of surrounding water. After intraperitoneal injection, Gd-DTPA is absorbed into the blood pool and delivered to the retina through circulation. Under normal conditions, Gd-DTPA does not penetrate the intact blood–

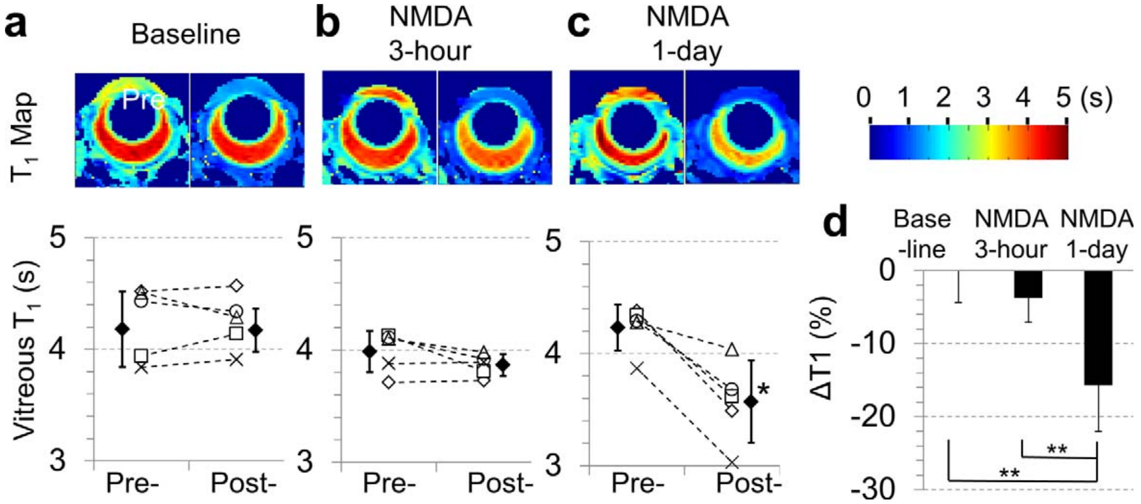

Figure 5. Gd-DTPA–enhanced MRI detected vitreous T1 in mouse eyes at baseline (**a**), 3 hours (**b**) or 1 day (**c**) after NMDA injection. *Top images*: representative T1 maps of each mouse eye acquired before (*left*) and at 30 minutes after (*right*) intraperitoneal injection of Gd-DTPA. *Bottom graphs*: quantified vitreous T1 before and after Gd-DTPA treatment. Each pair of *open symbols*, linked by a dashed line, represents the vitreous T1 of the eye measured pre- and postintravenous injection of Gd-DTPA from each individual mouse. The *filled symbols* represent the averaged vitreous T1 of all five mice. Statistical analysis showed the leaked Gd-DTPA resulting in a substantial decrease of vitreous T1 ($\Delta T1 = -16 \pm 6\%$) in mice at 1 day after NMDA injection (**d**). In all mice, the T1 of anterior chamber was reduced after Gd-DTPA treatment due to its fluid supply from the blood pool that contains Gd-DTPA. AC, anterior chamber; V, vitreous; Pre-, before Gd-DTPA treatment; Post-, 30 minutes after Gd-DTPA treatment. *$P < 0.05$ compared with vitreous T1 of the same mice before Gd-DTPA treatment. **$P < 0.01$ compared with ΔT1 of other groups. Data were presented as mean ± SD.

retinal barrier into the avascular vitreous. After blood–retinal barrier breakdown, the leakage of Gd-DTPA from the retinal vessels into the vitreous, as well as the diffusion of leaked Gd-DTPA from the choroid vascular bed to the vitreous, results in shortening of the vitreous T1 that can be quantified by MRI.[25,29,39,40]

Our results showed that retinal thickening developed before retinal vascular leakage in NMDA-injured mice. Decreased inner retinal ADC was observed at both 3 hours and 1 day after NMDA injection, reflecting inner retinal cell swelling. At 3 hours after NMDA injection, the vitreous T1 was not changed after systematic Gd-DTPA injection, reflecting the integrity of blood–retina barrier. Thus, the substantial thickening of the inner retina suggests a dominant contribution of cell swelling at this early time point. This is distinct from that observed in brain injury, where a volumetric increase of

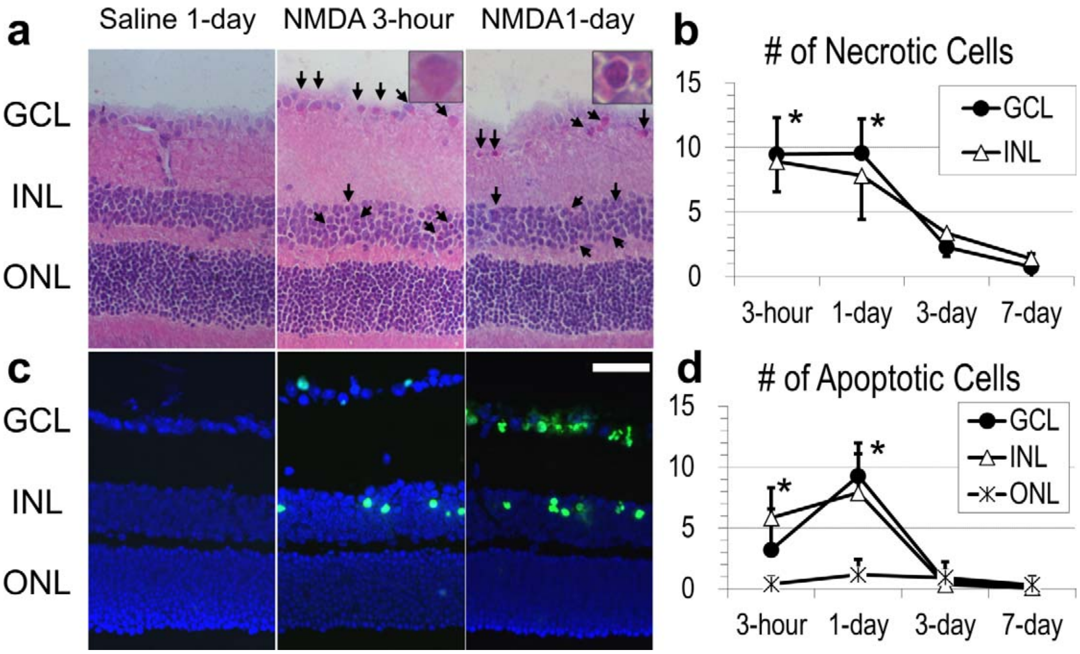

Figure 6. Histology analysis of NMDA excitotoxicity induced cell necrosis and apoptosis in different retinal cell layers. H&E staining shows necrotic cells (*arrows*) that stained with eosinophilic, pink cytoplasm and pyknotic (shrunken), purple nuclei in GCL (e.g., *middle insert*) and INL (e.g., *right insert*) (**a**). TUNEL staining shows apoptotic cells in green color (**b**). Quantitative analysis showed the number of necrotic (**c**) and apoptotic (**d**) cells in GCL and INL peaked at 3 hours and 1 days. Sporadic apoptotic cells, but no necrotic cells, were observed in the ONL. *$P <$ 0.05 compared with 3 and 7 days after NMDA injection. Data were presented as mean ± SD.

cerebral tissue is primarily caused by vascular leakage instead of cell swelling.[10] In mice at 1 day after NMDA injection, however, Gd-DTPA treatment caused a 16 ± 6% decrease of the vitreous T1, indicating the presence of retinal vascular leakage. The coexisting vascular leakage and cell swelling at this time point may jointly contribute to the inner retinal thickening.

The different effect of cell swelling on retinal and cerebral tissue volume might be attributed to the different external fluid supply to these tissues. Excitotoxicity-induced neuron cell swelling is developed by intracellular sequestration of water with Na^+ influx.[10] In the brain, the blood pool is the only source of external fluid supply. The fluid movement from the blood pool to extracellular space is tightly controlled by the blood–brain barrier, consisting of tight junctions around capillaries, largely impermeable to ions and fluids.[41] If the blood–brain barrier is intact, cerebral cell swelling will develop by redistributing extracellular water into intracellular space without increasing the brain volume.[10] In contrast, the retina experiences sustained transretinal fluid flux, driven by hydrostatic pressure gradient, from the vitreous to the choroid.[5] When the blood–retinal barrier is intact, the extracellular water is likely replenished by the transretinal fluid flux and/or diffusion, resulting in an overall increase of the retinal fluid volume (i.e., retinal thickening). This mechanism of cell swelling–induced retinal thickening is consistent with previous findings of acutely developed retinal thickening, retina cell swelling, and extracellular space shrinkage in whole-mount guinea pig retina preparation exposed to 1 mM L-glutamate.[42] The unchanged retinal thickness before L-glutamate exposure, the reduced extracellular space after L-glutamate exposure, together with the absence of blood hydrostatic pressure to drive vascular leakage suggested vasogenic edema did not contribute to the acute thickening of whole-mount retina. Thus, it is plausible that the observed cell swelling is the primary cause of L-glutamate excitotoxicity-induced retinal thickening.

The increased inner retinal thickness at 3 hours and 1 day after NMDA injection is in agreement with previous reports that excitotoxicity leads to acute thickening and chronic thinning of the inner retina.[12,43] The acute retinal thickening was, at least partly, caused by the swelling of injured cells.[42,44] The progressive death/loss of injured cells[12,26,27] caused inner retinal thickness thinning has been observed at 7 days after NMDA injection.[33,45–47] NMDA-decreased retinal thickness was shown to be dose dependent in rats.[33] Despite the NMDA dose effect on mouse retinal thickness has not been investigated in previous studies,[30,34,43,48–51] it has been shown that at least 30 nmol NMDA is needed in mice to cause significant death of retinal ganglion cells by 7 days after NMDA injection.[50] Accordingly, the low dose of NMDA (2.5 nmol) used in this study probably did not substantially damage retinal cells to cause significant retinal thinning at 7 days after NMDA injection.

In this study, the NMDA dose was selected to induce retinal cell swelling while minimizing the extent of cell death, which could potentially cause an ADC increase, complicating data interpretation.[52] The 0.5 μL injection volume was selected to avoid the risk of elevated intraocular pressure–induced retinal mechanical injury. Our results showed that retinal ADC was not altered after injection of 0.5 μL of saline (Fig. 4).

The current study has several limitations. First, excitotoxicity-induced cell swelling is not a major cause of retinal edema in patients. The development of cell swelling in retinal edema commonly occurred in ischemic and inflammatory diseases.[6,53] Since diffusion MRI–derived ADC is a marker of cell swelling despite its origin, selection of the NMDA mouse model does not undermine the potential of diffusion MRI to detect cell swelling in other retinal diseases. Second, this study did not directly evaluate glial cell swelling that has been documented in previous studies.[35,42] Third, Gd-DTPA–enhanced MRI was performed on control and NMDA-injured mice at 3 hours and 1 day after exposure. Since our results showed retinal vascular leakage occurred at 1 day after NMDA injection, the selected study groups sufficiently support that retinal cell swelling is the dominant contributor of retinal thickening at 3 hours after NMDA injection. However, it is unclear whether vascular leakage will continue at later time points (e.g., at 3 and 7 days) when cell swelling and apoptosis reduce and ADC returns to its normal value. Further investigation is needed in the future for a better understanding of the progression of retinal edema. Finally, quantitative ADC measurement requires four images, that is, three diffusion-weighted images oriented orthogonal to each other and one nondiffusion-weighted image. For a fast screening of disease-induced cell swelling, a diffusion-weighted image along a single direction, a 75% saving in acquisition time, may be acquired to reflect the effect without quantifying ADC (Fig. 1).

In summary, we used diffusion MRI–derived ADC to detect retinal cell swelling in the edematous retina using the NMDA mouse model. Our results revealed that retinal cell swelling can directly contribute to retinal thickening, a mechanism different from that observed in cerebral diseases. Compared with existing methods to detect retinal vascular leakage and retinal thickening, diffusion MRI assessment of cell swelling provides critical and complementary information for investigating the pathomechanism of retinal edema.

Acknowledgments

The authors thank Gregory M. Lanza, Samuel A. Wickline, and Bruce A. Berkowitz for their valuable comments on study design, and Tseng-Hsuan Lin, Jiayang Deng, and Noriko Yanaba for their help with histology.

References

1. Bringmann A, Reichenbach A, Wiedemann P. Pathomechanisms of cystoid macular edema. *Ophthalmic Res*. 2004;36:241–249.
2. Browning DJ. Diabetic macular edema. In: Browning DJ, ed. *Diabetic Retinopathy: Evidence-Based Management*. New York: Springer-Verlag; 2010:141–202.
3. Scholl S, Kirchhof J, Augustin AJ. Pathophysiology of macular edema. *Ophthalmologica*. 2010;224(suppl 1):8–15.
4. Yanoff M, Fine BS, Brucker AJ, Eagle RC Jr. Pathology of human cystoid macular edema. *Surv Ophthalmol*. 1984;28(suppl):505–511.
5. Marmor MF. Mechanisms of fluid accumulation in retinal edema. *Doc Ophthalmol*. 1999;97:239–249.
6. Bringmann A, Uckermann O, Pannicke T, Iandiev I, Reichenbach A, Wiedemann P. Neuronal versus glial cell swelling in the ischaemic retina. *Acta Ophthalmol Scand*. 2005;83:528–538.
7. Pannicke T, Uckermann O, Iandiev I, Wiedemann P, Reichenbach A, Bringmann A. Ocular inflammation alters swelling and membrane characteristics of rat Müller glial cells. *J Neuroimmunol*. 2005;161:145–154.
8. Ciulla TA, Amador AG, Zinman B. Diabetic retinopathy and diabetic macular edema: pathophysiology, screening, and novel therapies. *Diabetes Care*. 2003;26:2653–2664.
9. Lobo CL, Bernardes RC, Cunha-Vaz JG. Alterations of the blood-retinal barrier and retinal thickness in preclinical retinopathy in subjects with type 2 diabetes. *Arch Ophthalmol*. 2000;118:1364–1369.

10. Liang D, Bhatta S, Gerzanich V, Simard JM. Cytotoxic edema: mechanisms of pathological cell swelling. *Neurosurg Focus*. 2007;22:E2.
11. Alm A, Ehinger B. Retina. In: Kaufman P, Alm A, eds. *Adler's Physiology of the Eye*. St. Louis, MO: Mosby; 2002:319–438.
12. Sun Q, Ooi VE, Chan SO. N-Methyl-D-aspartate-induced excitotoxicity in adult rat retina is antagonized by single systemic injection of MK-801. *Exp Brain Res*. 2001;138:37–45.
13. Schaefer PW, Grant PE, Gonzalez RG. Diffusion-weighted MR imaging of the brain. *Radiology*. 2000;217:331–345.
14. Basser PJ, Jones DK. Diffusion-tensor MRI: theory, experimental design and data analysis—a technical review. *NMR Biomed*. 2002;15:456–467.
15. Hagmann P, Jonasson L, Maeder P, Thiran JP, Wedeen VJ, Meuli R. Understanding diffusion MR imaging techniques: from scalar diffusion-weighted imaging to diffusion tensor imaging and beyond. *Radiographics*. 2006;26(suppl 1):S205–S223.
16. Loubinoux I, Volk A, Borredon J, et al. Spreading of vasogenic edema and cytotoxic edema assessed by quantitative diffusion and T2 magnetic resonance imaging. *Stroke*. 1997;28:417–426.
17. Sevick RJ, Kanda F, Mintorovitch J, et al. Cytotoxic brain edema: assessment with diffusion-weighted MR imaging. *Radiology*. 1992;185:687–690.
18. Schaefer PW, Buonanno FS, Gonzalez RG, Schwamm LH. Diffusion-weighted imaging discriminates between cytotoxic and vasogenic edema in a patient with eclampsia. *Stroke*. 1997;28:1082–1085.
19. Pierpaoli C, Alger JR, Righini A, et al. High temporal resolution diffusion MRI of global cerebral ischemia and reperfusion. *J Cereb Blood Flow Metab*. 1996;16:892–905.
20. Runge VM, Clanton JA, Lukehart CM, Partain CL, James AE Jr. Paramagnetic agents for contrast-enhanced NMR imaging: a review. *AJR Am J Roentgenol*. 1983;141:1209–1215.
21. Larsson HB, Courivaud F, Rostrup E, Hansen AE. Measurement of brain perfusion, blood volume, and blood-brain barrier permeability, using dynamic contrast-enhanced T(1)-weighted MRI at 3 tesla. *Magn Reson Med*. 2009;62:1270–1281.
22. Larsson HB, Stubgaard M, Frederiksen JL, Jensen M, Henriksen O, Paulson OB. Quantitation of blood-brain barrier defect by magnetic resonance imaging and gadolinium-DTPA in patients with multiple sclerosis and brain tumors. *Magn Reson Med*. 1990;16:117–131.
23. Silver NC, Good CD, Barker GJ, et al. Sensitivity of contrast enhanced MRI in multiple sclerosis. Effects of gadolinium dose, magnetization transfer contrast and delayed imaging. *Brain*. 1997;120:1149–1161.
24. Wolansky LJ, Finden SG, Chang R, et al. Gadoteridol in multiple sclerosis patients. A comparison of single and triple dose with immediate vs. delayed imaging. *Clin Imaging*. 1998;22:385–392.
25. Berkowitz BA, Roberts R, Luan H, Peysakhov J, Mao X, Thomas KA. Dynamic contrast-enhanced MRI measurements of passive permeability through blood retinal barrier in diabetic rats. *Invest Ophthalmol Vis Sci*. 2004;45:2391–2398.
26. Trick GL, Liggett J, Levy J, et al. Dynamic contrast enhanced MRI in patients with diabetic macular edema: initial results. *Exp Eye Res*. 2005;81:97–102.
27. Sato Y, Berkowitz BA, Wilson CA, de Juan E Jr. Blood-retinal barrier breakdown caused by diode vs argon laser endophotocoagulation. *Arch Ophthalmol*. 1992;110:277–281.
28. Vinores SA, Derevjanik NL, Mahlow J, Berkowitz BA, Wilson CA. Electron microscopic evidence for the mechanism of blood-retinal barrier breakdown in diabetic rabbits: comparison with magnetic resonance imaging. *Pathol Res Pract*. 1998;194:497–505.
29. Wang Q, Song SK, Zhang H, et al. Photoreceptor degeneration changes magnetic resonance imaging features in a mouse model of retinitis pigmentosa. *Magn Reson Med*. 2011;65:1793–1798.
30. Awai M, Koga T, Inomata Y, et al. NMDA-induced retinal injury is mediated by an endoplasmic reticulum stress-related protein, CHOP/GADD153. *J Neurochem*. 2006;96:43–52.
31. Chen J, Wang Q, Zhang H, et al. In vivo quantification of T1, T2, and apparent diffusion coefficient in the mouse retina at 11.74T. *Magn Reson Med*. 2008;59:731–738.
32. Chen J, Wang Q, Chen S, Wickline SA, Song SK. In vivo diffusion tensor MRI of the mouse retina: a noninvasive visualization of tissue organization. *NMR Biomed*. 2011;24:447–451.
33. Lam TT, Abler AS, Kwong JM, Tso MO. N-Methyl-D-aspartate (NMDA)–induced apoptosis in rat retina. *Invest Ophthalmol Vis Sci*. 1999;40:2391–2397.
34. Lebrun-Julien F, Duplan L, Pernet V, et al. Excitotoxic death of retinal neurons in vivo occurs via a non-cell-autonomous mechanism. *J Neurosci*. 2009;29:5536–5545.
35. Izumi Y, Kirby CO, Benz AM, Olney JW, Zorumski CF. Müller cell swelling, glutamate uptake, and excitotoxic neurodegeneration in the isolated rat retina. *Glia*. 1999;25:379–389.
36. Osborne NN, Casson RJ, Wood JP, Chidlow G, Graham M, Melena J. Retinal ischemia: mechanisms of damage and potential therapeutic strategies. *Prog Retin Eye Res*. 2004;23:91–147.
37. Cheng H, Nair G, Walker TA, et al. Structural and functional MRI reveals multiple retinal layers. *Proc Natl Acad Sci USA*. 2006;103:17525–17530.
38. Cobb JP, Hotchkiss RS, Karl IE, Buchman TG. Mechanisms of cell injury and death. *Br J Anaesth*. 1996;77:3–10.
39. Berkowitz BA, Sato Y, Wilson CA, de Juan E. Blood-retinal barrier breakdown investigated by real-time magnetic resonance imaging after gadolinium-diethylenetriaminepentaacetic acid injection. *Invest Ophthalmol Vis Sci*. 1991;32:2854–2860.
40. Berkowitz BA, Tofts PS, Sen HA, Ando N, de Juan E Jr. Accurate and precise measurement of blood-retinal barrier breakdown using dynamic Gd-DTPA MRI. *Invest Ophthalmol Vis Sci*. 1992;33:3500–3506.
41. Rubin LL, Staddon JM. The cell biology of the blood-brain barrier. *Annu Rev Neurosci*. 1999;22:11–28.
42. Uckermann O, Vargova L, Ulbricht E, et al. Glutamate-evoked alterations of glial and neuronal cell morphology in the guinea pig retina. *J Neurosci*. 2004;24:10149–10158.
43. Ito Y, Shimazawa M, Inokuchi Y, et al. Degenerative alterations in the visual pathway after NMDA-induced retinal damage in mice. *Brain Res*. 2008;1212:89–101.
44. Hama Y, Katsuki H, Suminaka C, Kume T, Akaike A. Chloride-dependent acute excitotoxicity in adult rat retinal ganglion cells. *Neuropharmacology*. 2008;55:677–686.
45. Honjo M, Tanihara H, Kido N, Inatani M, Okazaki K, Honda Y. Expression of ciliary neurotrophic factor activated by retinal Müller cells in eyes with NMDA- and kainic acid-induced neuronal death. *Invest Ophthalmol Vis Sci*. 2000;41:552–560.
46. Luan H, Roberts R, Sniegowski M, Goebel DJ, Berkowitz BA. Retinal thickness and subnormal retinal oxygenation response in experimental diabetic retinopathy. *Invest Ophthalmol Vis Sci*. 2006;47:320–328.
47. Morizane C, Adachi K, Furutani I, et al. N(omega)-nitro-L-arginine methyl ester protects retinal neurons against N-methyl-D-aspartate-induced neurotoxicity in vivo. *Eur J Pharmacol*. 1997;328:45–49.
48. Karl MO, Hayes S, Nelson BR, Tan K, Buckingham B, Reh TA. Stimulation of neural regeneration in the mouse retina. *Proc Natl Acad Sci USA*. 2008;105:19508–19513.

49. Li Y, Schlamp CL, Poulsen GL, Jackson MW, Griep AE, Nickells RW. p53 regulates apoptotic retinal ganglion cell death induced by N-methyl-D-aspartate. *Mol Vis*. 2002;8:341–350.
50. Nakazawa T, Takahashi H, Nishijima K, et al. Pitavastatin prevents NMDA-induced retinal ganglion cell death by suppressing leukocyte recruitment. *J Neurochem*. 2007;100:1018–1031.
51. Shimazawa M, Inokuchi Y, Ito Y, et al. Involvement of ER stress in retinal cell death. *Mol Vis*. 2007;13:578–587.
52. Morse DL, Galons JP, Payne CM, et al. MRI-measured water mobility increases in response to chemotherapy via multiple cell-death mechanisms. *NMR Biomed*. 2007;20:602–614.
53. Bringmann A, Pannicke T, Grosche J, et al. Müller cells in the healthy and diseased retina. *Prog Retin Eye Res*. 2006;25:397–424.